Suppression of acoustic streaming in liquids of inhomogeneous density and compressibility

Dženan Hajdarović

MASTER'S THESIS IN
BIOMEDICAL ENGINEERING

DEPARTMENT OF BIOMEDICAL ENGINEERING
LUND UNIVERSITY, LTH

Supervisor: Per Augustsson
Examiner: Christian Antfolk

November 22, 2016

"Nature composes some of her loveliest poems for the microscope and the telescope."

– THEODORE ROSZAK

DEDICATION

This one is for all those countless hours filled with a roller-coaster of emotions, which wouldn't be possible to endure without you. Thanks for being there. Pushing me. Encouraging me every step on the way.

To my dearest mother Naila, being my biggest supporter and friend in life.

To my beloved soulmate Ramajana, keeping both my heart and mind at ease.

To my family, for which I'm truly blessed to have.
"Hvala vam svima dragi moji, ništa bez vas."

To my friends, filling my spare time with laughter and joy. Lastly, a special "SMD" greeting goes out to Axel, Björn, Erik, James and Johan.

Love,
D.H

★

ABSTRACT

This thesis provides strong evidence that acoustic streaming is suppressed when using liquids of inhomogeneous density and compressibility in acoustophoresis. Manipulation of extremely small particles in acoustophoresis is something that usually is impaired by acoustic streaming.

The project was divided into three aims. Firstly, a particle tracking software (GDPT) was evaluated using 3 μm polystyrene beads letting them sediment inside of a microchannel. Then, the flow of 1 μm and 4.8 μm polystyrene beads was studied separately, influenced by an acoustic field. The obtained trajectories and velocities of these beads were then solved analytically with existing theory describing acoustophoretic particle motion. Lastly and most importantly, the acoustic streaming of 1 μm polystyrene beads was examined when laminating the particle-solution with a density gradient medium called iodixanol, following acoustic actuation.

The evaluation of the GDPT-software and the particle trajectories and velocities were deemed as valid since they corresponded to theoretical expectations. Regarding the main goal of the project, it was found that when using inhomogeneous medium, the acoustic streaming would decrease by a factor of 57, in comparison to when homogeneous medium is used. The acoustic streaming is thus mainly influenced by the acoustic radiation force, giving a lateral motion of the polystyrene beads.

Ultimately, these results indicate that it will be possible to manipulate and deal with particles as small as bacteria and viruses in acoustophoresis, giving a potential tool, globally speaking, in the fight against aggressive infections in today's healthcare.

Keywords — *inhomogeneous medium, density gradients, acoustic streaming, iso-acoustic focusing, acoustophoresis, microchannel, microfluidics, general defocusing particle tracking, astigmatic particle tracking, polystyrene beads*

ACKNOWLEDGEMENTS

First of all, a sincere thanks to my supervisor Per Augustsson for giving me a helping hand throughout this project. His insights and knowledge have lead me towards great accomplishments.

Thank you Rune Barnkob for giving me access to the GDPT-software and also for explaining how it should be used during my initial testings.

Thanks to Ola Jakobsson and Anna Fornell for generously letting me use their working station for the experiments from time to time.

I am also very grateful for all the friendly, funny and interesting discussions with the other master students in the "exjobbar-rummet".

Lastly, a big thanks to all the remaining staff of the faculty of biomedical engineering in LTH who, in many ways have helped me find my way around the department in the beginning of the project and for always meeting me with a smile and kind words.

TABLE OF CONTENTS

LIST OF ABBREVIATIONS

LOC   *L*ab *O*n a *C*hip

IAF   *I*so *A*coustic *F*ocusing

μTAS   *M*icro *T*otal *A*nalysis *S*ystems

MEMS   *M*icro*E*lectro*M*echanical *S*ystems

Bio-MEMS   *Bio*logical *M*icro*E*lectro*M*echanical *S*ystems

Re   *Re*ynolds number

GDPT   *G*eneral *D*efocusing *P*article *T*racking

PS   *P*oly*S*tyrene

DNA   *D*eoxyribo*N*ucleic *A*cid

RNA   *R*ibo*N*ucleic *A*cid

PCR   *P*olymerase *C*hain *R*eaction

ARF   *A*coustic *R*adiation *F*orce

PRF   *P*rimary *R*adiation *F*orce

SRF   *S*econdary *R*adiation *F*orce

AD   *A*nalog-to-*D*igital

PZT	*P*iezolectric *T*ransducer
NS	*N*avier *S*tokes
DEP	*D*iElectro*P*horesis
MACS	*M*agnetic *A*ctivated *C*ell *S*orting
POC	*P*oint *O*f *C*are

LIST OF FIGURES

LIST OF TABLES

CHAPTER 1

INTRODUCTION

Knowledge is a resource that has a specific driving factor, namely curiosity. Only in the last few decades, a lot of new fascinating discoveries have turned our society around and thus, also the way we live in. Curiosity leads to new questions asked, new problems obtained and new ideas resulting in rewarding solutions. This is the never ending loop of scientific success. The remarkable diversity of science can be seen in all of the multidisciplinary fields that are continuously thriving. Microfluidics is such a scientific field, one in the crowd, constantly being studied further and better understood, thanks to the curiosity of researchers. This is the science of miniaturizing systems used for biological analyses and consists of countless numbers of diverse methods, all having their own smart solutions, which will be elaborated more in detail in this thesis. It combines the physics when downscaling to the sub-micro scale with fluid behaviour.

Acoustophoresis is a special method in many ways, having its roots in the physics of microfluidics and actually being developed at the department where this master thesis also took place in, the department of biomedical engineering in Lund university. By using ultrasound waves and applying these to the microchannel which has features that are smaller than a few tenths of a millimetre, it was made possible to manipulate small suspended particles inside the microchannel, thus enabling focusing [20], separation [14], trapping [21], washing of the fluids [22] etc. As already mentioned, the way of science is comprised of looking at things at different angles and asking the right questions. A drawback considering acoustophoresis is its strong size dependency, related to the radius of the particles used. It is the most significant and domi-

nant separation property of particles which complicates separations based on the underlying intrinsic acoustic properties, the density of the particles and their compressibility.

New discussions have led to considering finding a way to decrease this size dependency, thus improving acoustophoresis. The goal is to create a size-insensitive version that would theoretically only depend on the intrinsic acoustic properties of the particles. This is exactly what is accomplished with the groundbreaking method called Iso-acoustic fosusing (IAF), also pioneered and presented by scientists at the department of Biomedical Engineering [19]. IAF has the potential to expand into a game-changer in Lab-on-a-chip-systems, touching unknown grounds by creating completely new separation terms. In IAF, both particles and the medium itself have been observed to behave qualitatively differently than compared to traditional acoustophoresis. This particular feature, combined with a closer study of acoustic streaming using the IAF-method has never been done before, which this thesis will take a closer look into. Acoustic streaming is a phenomenon that takes the form of vortices inside of microchannels, thereby causing problems regarding the separation and focusing and it is the dominating fluid motion when using particles with a radius smaller than around 1 μm. Ultimately, in the near future, IAF could enable working with even smaller particles when employing acoustic manipulation methods, such as bacteria and viruses.

CHAPTER 2

BACKGROUND

This chapter will initially put forward all the essential theory needed in order to understand the underlying physics and some of the many methods being utilized in the field of microfluidics with deeper explanations regarding acoustic manipulation methods. The theoretical background will be rounded off by explaining how the general defocusing particle tracking (GDPT) works.

2.1 Microfluidics − The nano-scale realm

Microfluidics is a field in science that explains how small things can have a big impact on the world around us. It contains the knowledge of controlling, mixing, separating, purifying, manipulating and analysing extremely small, or rather, ungraspable sample volumes that lie in the nano-range and even beyond that $(10^{-9}$ - 10^{-18} litres) [1, 8]. The small volumes are being analysed in different devices or channels/chips that are the same size as that of a single hair in the sub millimetre range. Medical diagnostics and the healthcare sector employ many of the methods that come straight from the field of microfluidics.

2.1.1 The physical advantage

Modern society has reached an impressive technological level. The somewhat universal condition making this possible has been to always try to save time and money. Time and money are indeed being saves using these microchannels, but why has there been a big urge to study microfluidics in detail the last

decades, what more advantages could this science of nature's small components possibly give us? The most important answer lies in the universal laws of physics. When we go down the scale, into the nano-scale realm, new and fascinating properties are revealed that differ from the ones we experience in our macro dimensions. In this region, the behaviour of fluids is simply changed from what we normally are used to.

Perhaps the easiest way to describe the change in fluid behaviour is with the help of the elegantly formulated dimensionless equation called the Reynolds number, see Eq. (2.1).

$$Re = \frac{inertial\,forces}{viscous\,forces} = \frac{\rho uL}{\mu} \tag{2.1}$$

where ρ is the fluid's density, u is the average speed of the fluid's flow, μ describes the fluid's dynamic viscosity and L is the characteristic length of the geometry where the fluid flows. This characteristic length does not correspond to the length of a pipe but rather the smallest dimension, for instance the distance from the centre of a fluid to the surrounding wall.

By using the Reynolds equation, one can predict how the fluid will behave depending on the four input parameters [3]. There are two forces that can dominate and thereby determine a fluid's characteristics, either the inertial or the viscous forces as seen in Eq. (2.1). In our everyday life, whether we stir around our coffee, fill up our car with petrol or take on a huge wave in the ocean, we will always encounter fluids where the inertial forces dominate, a behaviour which is called turbulent flow. After looking at the Reynolds equation, this corresponds to high values, approximately over 2000. In this state, the fluid is constantly changing its direction and also the speed of the flow in all positions, which more or less can be described as disordered and randomized mixing, see Fig. (2.1b).
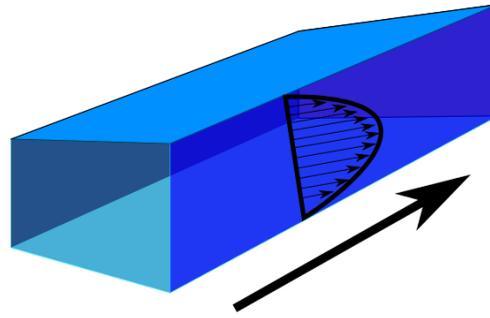
a) Laminar flow
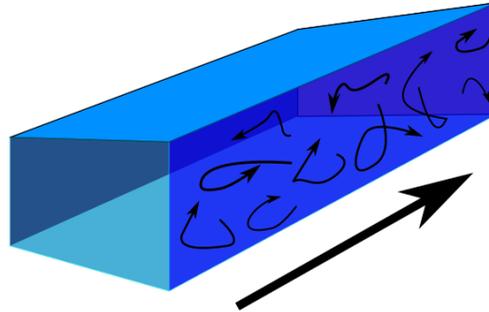
b) Turbulent flow

Figure 2.1: **Flows inside a microchannel. (a) Low Re-numbers correspond to slow and predicted flow lines, called laminar flow. (b) High Re-numbers correspond to unpredicted and high velocities of the fluid, called turbulent flow.**

The other fluid behaviour, which is more relevant to this work is called the laminar flow, where the viscous forces take over and dominate, see Fig. (2.1a). This aspect is exactly what we obtain when downscaling to the nano-range which corresponds to lower Re-values (Re < 2000). For simplicity, viscous fluids can be referred to or seen as thick liquids, for instance ketchup or honey. In the macro region, a "thick" fluid is non-turbulent, having a high viscosity and thus a low Re-number. As seen in Eq. (2.1), when going down in scale and decreasing the dimensions, we receive a lower value of the Re-number. The same result goes for fluids with low viscocity. The dynamic viscosity explains how good or bad a fluid is at resisting deformation after being affected by shear or tensile stress [3]. This explains why you sometimes have a difficult time squeezing out ketchup or honey from a tube, but water, which has lower viscosity than ketchup, always flows smoothly.

Table 2.1: **Fluid properties of honey and water, μ - viscosity, ρ - density, L - characteristic length, u - velocity.**

Fluids	μ [Pa s]	ρ [kg/m^3]	L [m]	u [m/s]
Honey	10	1420	0.1	0.1
Water	0.001	1000	0.1	0.1

Let us take honey as a concrete example with its high viscosity of 10 Pa s compared to water which only has 0.001 Pa s [23]. Let's further assume that we pour the honey and water in two different jars with the same dimension L = 0.1 m after which the fluids are being stirred around with approximately the same velocities, see Table 2.1. Using the values for the honey and adding them in Eq. (2.1) gives us a Re-number of 1.42, which indicates that we have laminar flow present. At the same time, the properties of water would result in an extremely huge Re-number, due to the low viscosity, and thus a turbulent flow is obtained. If you instead were to suck up the water using a thin straw, this would result in laminar flow since the characteristic dimension L would be decreased, same goes for decreasing the velocity u. This thought experiment showcases the practical advantage of Eq. (2.1).

During laminar flow, Fig. (2.1a), a fluid travels in a straight and undisturbed fashion with no lateral mixing. Laminar liquids will flow next to each other in distinct streamlines. One of the biggest advantages with the laminar flow is that it is straightforward to explain mathematically, as explained, using Eq. (2.1). Through the physical laws of microfluidics, we are given a chance to understand how our own body works at the cellular level. This insight by mimicking in microchannels of how, for instance, the blood flows through our bodies gives us a chance to take on common diseases in a whole new and improved way.

The promising prospects still do not end here. The knowledge obtained from microfluidics has set its roots far deeper and even to this date, new research findings are constantly being developed into complex and novel methods. It has given us the opportunity to study small objects using different forces and external fields, such as capillary forces, pressure gradients, acoustic-, electric- and magnetic fields [2, 3].

Other examples conclude simplifying chemistry procedures, learning how to mix solutions easier in the sub-millimetre range, control fluids using microvalves and micropumps, particle trapping, heat control for PCR analysis,

incubating and manipulating particles using small droplets, study biomolecules such as DNA, RNA and proteins using microarrays, testing and delivery of drugs, devices used in point-of-care diagnostics and the list goes on [3–5, 7–12].

As can be seen by the great diversity of examples, microfluidics is an inter-disciplinary field that interweaves many different technologies, giving rise to meaningful discoveries. The future of microfluidics is looking bright, considering that it still is a relatively young field of science. Some of the physical theory behind the mentioned methods will be explained more in detail, in the forthcoming sections.

2.1.2 Parabolic flow profile - Simplifying the Navier Stokes equations

As explained, the Re-number can determine if a fluid will have laminar or turbulent flow which is a characteristic knowledge of great importance. Furthermore, the so called Navier-Stokes equations have the ability to describe in detail, exactly how the motion of viscous fluids looks and behaves like and what velocities that can be expected at different points and areas of the fluid [3,13]. This can give a better prediction of how viscous fluids will flow in microchannels of different geometries, for instance describing the difference when using a rectangular contra a cylindrical channel, thus giving a better understanding which is needed in the fabrication of microfluidic devices utilizing flows of viscous fluids.

The complete Navier-Stokes equations are derived from Newtons second law, describing the relation between the force applied to an object as its mass multiplied with its acceleration ($F = m \cdot a$). The NS-equations can thus be seen as a special case of the conservation of momentum while only concentrating on viscous fluids [3, 13]. In their entirety, the NS-equations take account for viscous fluids, that external forces may be applied and that the viscosity of the fluid is temperature dependent. Luckily, in the field of microfluidics, much of these considerations can be neglected. Since we most often use so called Newtonian fluids (shear stresses linearly proportional to the velocity gradients) that are both isotropic (uniform mechanical properties in all directions) and incompressible (constant density), the complex NS-equations can be simplified to [3]:

$$-\frac{\partial p}{\partial x} + \eta \left(\frac{\partial^2 u_x}{\partial y^2} + \frac{\partial^2 u_x}{\partial z^2} \right) = 0 \qquad (2.2)$$

$$\frac{\partial p}{\partial y} = \frac{\partial p}{\partial z} = 0 \qquad (2.3)$$

where p is the applied pressure, η is the dynamic viscosity of the fluid and x, y, z correspond to the microchannels length, width and height respectively.

Eq. (2.2) and (2.3) explain the nature behind the so called parabolic flow profile which is seen in laminar flow, as illustrated in Fig. (2.1a). Only the pressure gradient along the flow direction is considered in this equation (x-direction) with a constant viscosity, thus neglecting any temperature alteration. The velocity u_x has a maximum value at the centre of the channel, when fully developed laminar flow is achieved. At the microchannels solid boundaries, e.g top and bottom, the velocity will instead go down to zero. This is explained by the so called "no slip condition" which is an essential approximation that more or less assumes that the outermost parts of the viscous fluid stick to the walls. Different shapes of the geometry in which the viscous fluid flows through, lead to different analytical expressions of the magnitude of velocity u_x. In this project, the used microchannel had a rectangular shape. The theory used for describing acoustophoretic particle movement and velocities considers a rectangular shape with such confining boundaries.

2.1.3 Mass transfer - Advection versus Diffusion

There is yet another important phenomenon in microfluidics that the NS-equations do not explain, namely diffusion. The intuitive way to think of how a fluid transports and mixes itself is by considering how the bulk of the fluid is carrying the entire liquid around, a process which is referred to as advection. On the other hand, as originally explained by Albert Einsten back in 1905 [35], individual particles are constantly moving in a random fashion which he denoted as Brownian motion, after the man who initially found this peculiar physical property. Einstein proposed that the mean distance that a single particle is transferred by this Brownian motion is thermically driven and can be expressed as [35]:

$$\bar{x} = 2\sqrt{Dt} \qquad (2.4)$$

where $\bar{x}$ is the mean transferred distance of the Brownian particle, D is its diffusion constant and t stands for the elapsed diffusion time.

This motion can be even be distinguished in atoms. Combining a lot of single Brownian particles and instead considering larger solutions, the properties and behaviour of diffusion is established in a more understandable way. The most common way to explain diffusion is by the appearance of a concentration gradient, where areas of high concentration tend to transfer its mass to areas of low concentration, or in other words, down the concentration gradient. Diffusion is simply an act of equalization, seeking an even concentration throughout the whole fluid, often described as nature's own way of distributing energy evenly. This way of going down the concentration gradient and the time dependency is explained by Fick's first and second law, respectively [3]:

$$J = -D \frac{\partial C}{\partial x} \tag{2.5}$$

$$\frac{\partial C}{\partial t} = D \frac{\partial^2 C}{\partial x^2} \tag{2.6}$$

where J is the flow/flux of the fluid, D is the diffusion coefficient and x corresponds to the distance traveled.

The often used diffusion constant $[m^2/s]$ is explained by the Stokes-Einstein relation [3]:

$$D = \frac{kT}{6\pi \eta R_H} \tag{2.7}$$

where k is the Boltzmann constant, T is the temperature, η is the dynamic viscosity and R_H is the hydrodynamic radius of the particle.

The dimensionless Peclet number (Pe) is a way to describe the relation between advection and diffusion [3]:

$$Pe = \frac{advective\ mass\ transfer}{diffusive\ mass\ transfer} = \frac{Lu}{D} \tag{2.8}$$

where L is the characteristic length, u is the velocity of the flow and D is the diffusion coefficient.

When fully developed and steady laminar flow is present in microfluidic microchannels, the streaming lines are parallel to each other and thus, no lateral mixing can be achieved, so mixing or mass transfer of the fluids is instead regulated by diffusion, where the two fluids interface, see Fig. (2.2). The reason behind this is easily understood when looking at Eq. (2.8). The advective mass transfer dominates when we use large dimensions and high velocities,

whereas diffusion dominates when these parameters are low, such as in microfluidic devices, having velocities and dimensions in the sub-micro range. When Pe ≪ 1, diffusion is the dominating mass transfer process.
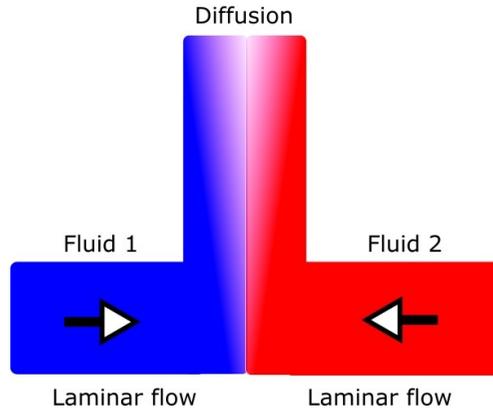
Figure 2.2: **In the laminar flow regime, mixing between fluids is accomplished by diffusion. The purple region is a representation of the mixing caused by diffusion after the two laminar streaming lines are merged together at the intersection.**

By looking at the Brownian motion in Eq. (2.4), it can be understood that diffusion is an extremely fast process when dealing with small distances, which the dimensions in microfluidics allow for and also when the diffusion constants are fairly small, referring to smaller particles and ions of the solutions. Over larger distances and for bigger particles, diffusion becomes less and less dominant whilst advection takes over as explained by the Pe-number in Eq. (2.8). The typical time range for mixing of laminar fluids can be obtained from Eq. (2.4), knowing the diffusion distance and diffusion coefficient of the solutions. This thesis will also encounter the impact of diffusion as the two fluids used, iodixanol and a water solution containing beads, were allowed to be mixed in order to obtain a homogeneous medium. After mixing had occurred, acoustic streaming was once again present in the analysis for 1 μm PS-beads. Assume that the diffusion/travel distance is across a microchannel's height of, for instance, 150 μm and a diffusion constant of about $2.5 \cdot 10^{-10}$ m^2/s for iodixanol [36], when considering room temperature and mixing of iodixanol with an aqueous solutions as illustrated in Fig. (2.2). This gives us a total diffusion time of t = 45 s. In this project, around 30 seconds after acoustic actuation it was observed that acoustic streaming once again started to slowly develop, thus meaning that the inhomogeneous property of the medium was starting to dissapear thanks to mixing of iodixanol and the PS-beads solution by diffusion. The waiting time for total mixing

to take place in this project was set to 5 minutes, which is more than enough time considering it takes on an average 45 s for one iodixanol particle to move around 150 μm. This will be discussed more in detail in chapter 7.

2.2 Lab-on-a-chip systems in life science

The goal in life science and biomedicine has always been to achieve, among other things, faster sample analysis, less energy consuming devices, smaller sample and reagent volumes and high throughput analyses leading to bigger and more efficient population screenings. Suddenly, a new technology emerged that seemed to be able to fulfil all of these needs. When we furthermore entered a new era regarding the prediction and trend line of Moore's law, fitting smaller and smaller components into integrated circuits, the LOC lightbulb was finally lit.

2.2.1 Bio-MEMS and μTAS - The cornerstones of the Lab-on-a-chip concept

It is easy to say that the breakthrough and increasing interest in recent years for microfluidics would not be a reality, if it was not for the rise of a technology called Microelectromechanical systems (MEMS) [4]. These systems focused on building small devices in the micrometre range and use them as sensors based on mechanical and electronic feedback. Originally, the greatest issues that were studied, were regarding the construction and thereby the optimisation of the incorporated elements. However, the true potential of these novel systems was far from evident in its starting years. During the 1990's, the sequencing of DNA and study of proteins was one of the major research questions in the world of science [7,8]. The term bio-MEMS refers to the contribution and impact that the MEMS technology had on genomics, proteomics and other approaches in clinical diagnostics, just to mention a few [4,5,7,10].

The need for aiding chemists in automating their complicated analyses resulted in a method abbreviated as μTAS (total chemical analysis systems) in the year 1990 [6]. By introducing automated systems that used fluids, many of the difficult and time consuming steps in analytical chemistry that demanded great accuracy could now be simplified, e.g. separation, detection and filtration [6]. These systems were based on digitalisation of chemical data and information, converting chemical concentration of a substance into electrical signals [6].

The Lab-on-a-chip concept can be seen as a collection name for the μTAS and the biomedical branch from the MEMS-technology, referred to as bio-MEMS. The key words that demonstrate the similarities between these methods is the fact that they both rely on the physical and material benefits of down-scaling all the way to the nano-scale, leading to faster sample runs, less reagents and samples needed but also less waste products. Both methods can use sensitive sensor techniques, AD-conversion and also obtain high throughput during analysis of biological systems.

2.2.2 How the LOC-systems are being utilized

The diversity of methods being utilized from the knowledge behind microfluidics is vast. This section will discuss some interesting applications with different physical attributes and external forces implemented in LOC-systems.

External fields

Particles and cells in a fluid can be managed and manipulated by different external fields, such as electrical-, magnetic- and acoustic fields. Here follows an explanation on these.

Dielectrophoresis is a method where a non-uniform electrical field is applied over particles making them travel towards the positive or negative pole of the electrical field inside of an aqueous medium [3]. The particles need to be uncharged in order for a net dielectrophoretic force (DEP) to be created, which is dependent on the radius of the particles, the shape of the channel and how non-uniform and strong the electrical field is. The difference in dielectric properties between the medium and the particles (electric permittivity) is what creates the movement. Larger particles are thus affected more by the electrical field and can move faster to the positive or negative charged regions than smaller particles. This method is great for characterising and separating cells, e.g. cancer cells, from small volumes of blood samples.

Similarly, the method of *magnetophoresis* can be used to manipulate particles with magnetic properties, but instead applying an inhomogeneous magnetic field over them. One such method implementing an external magnetic field is called *magnetic activated cell sorting*. Here, magnetic nanoparticles are coated with a specific antibody acting as a tag, in such a way that when the external magnetic field is applied, the target particles (e.g. antigens) will attach to the magnetic nanoparticles' antibodies, which in turn will be magnetically affected and separate the entire bundled particle to a desired outlet

inside of the microchannel [39]. (Unyoung *et al.*, 2009) showed that this method was also possible to be used together with DEP-tags, thus increasing the separation properties. They called this a multi-target separation method using both magnetic and electrical external fields, showing that bacterias from a culture can be selectively purified by up to 95% from a sample after one run.

Acoustophoresis is a way of manipulating small particles in microchannels using standing waves created by ultrasound. This particular method is of great importance related to this thesis since it was implemented in the experiments. Thus, a more detailed explanation of the physics, history and method behind acoustophoresis and the improved IAF-method will be presented in section 2.3 and 2.6, respectively.

Drug detection using inertial microfluidics

As previously mentioned using the Reynolds number, viscous forces dominate over intertia when downscaling to the sub-micrometre range. There are still some ways where intertia can be benefitial in microfluidics, e.g. in drug- and bacteria detection in blood [40]. In an experiment done by (Hou *et al.*, 2015) and his colleagues, it was possible to detect bacterias in a blood sample and also measure how well a drug worked by detecting RNA-ribosomes of antibiotic sensitive transcripts. The microchip used in these experiments had curvatures and a spiral shape, giving rise to so called Dean flows. What these curvatures and spiral shape achieve is that the smaller particles in the blood (platelets and bacteria) are affected by Dean flow vortices in such a way that they are ultimately moved along the outer sidewall of the channel when they approach the outlet. The bigger erythrocytes (red blood cells) will instead move along the inner sidewall of the channel when approaching the outlet, since they are more affected by inertia because of their size and will thus be separated from bacteria.

Point-of-care using microfluidics

The goal with point-of-care (POC) devices is to favour both the patient and the caretakers and doctors at the hospital by giving a possibility for self-diagnosis instead of being constrained to long hospital visits. Such a device has some requirements; it should be giving fast answers, easy to use, possible to be used by the patient at home and preferably also directly coupled to the hospitals computer system for continuous check-ins by the doctors [9]. Microfluidic devices, with their fast sample analysis, small amount of sample and reagents needed and low cost, provide great opportunities to be developed into POC-devices.

A clever solution for blood analysis using a microfluidic trick was presented in (Mohammadi *et al.* , 2015). Initially, they used a *cross-flow filtration* (CFF) method with *capillary forces* and a driving *electroosmotic flow* (EOF) to separate plasma from blood. EOF is induced by applying a potential over the microfluidic device where the bulk fluid is driven by the potential differences between the medium and the microchannel boundaries. In CFF, a filter with many small membrane pores allows free passage only to the bigger desired particles (blood plasma) whilst solutes smaller than the membrane pores will be filtered out. Capillary action/force is also a phenomenon widely used in microfluidics, denoting to the movement of liquids "moving by themselves" inside a microchannel due to the impact of surface tension, which is a mixture between the desire of similar molecules to stick together (cohesive forces) and the possibility of sticking to the sidewalls (adhesive forces).

The problem with this initial method was that red blood cells (RGB) clogged at the entrance of the cross-flow filter. In order to counteract this problem, a reversible EOF was instead applied [12], breaking the clogging. Finally, they showed that by implementing this simple change, the desired blood plasma could be extracted with high purity (> 99%). Such smartly designed devices have great potential to be employed in POC testings and diagnostics in the future.

Microvalves, micropumps and micromixers

Microvalves can be used to stop and switch fluid directions of a flow inside of a microchannel. The most common used design today is called a *Quake microvalve* where the methodology consists of using two separate channels, one main semi-circular channel where the fluid is supposed to flow through and one air-filled rectangular channel, placed perpendicularly above it [41].

This rectangular channel is able to stop the flow when a pressure is applied to it, pressing it down on the semi-circular channel. The pressure is actively applied when needed and thus the direction of the flow inside a microchip device can be controlled accurately.

Micropumps are other applications in microfluidics that are of great aid when trying to control fluids inside microchip devices. They can be used passively or actively, without or with an external force applied [41]. The passive versions can simply use the capillary force which was mentioned earlier, based on a fluids surface tension. In such a micropump, many capillaries are placed next to each other, driving the fluid forward. Active micropumps can on the other hand control a fluid by exerting external forces, such as using e.g. electrically induced piezoelectric transducers while also using physical restrictions, as for instance walls. Thus, the flow rate of a fluid can be both directed and increased or decreased as desired.

As explained previously in section 2.1.3, the mass transfer and mixing in microfluidics is mainly affected and driven by diffusion, which is not a sufficient way of mixing fluids. Thus, means to create so called chaotic advection are needed [42]. This insight has lead to innovative mixing methods, making it faster and more efficient. Even in this case, both passive and active versions of *micromixers* can be used. Since we have laminar properties of fluids in microfluidics, for passive micromixers, many different designs have been developed. The so called T- and H-shaped micromixers are probably the most basic ones, having inlet sections where the two fluids meet and start mixing. The geometry; decreasing dimensions at an intersection simply enhances the molecular diffusion time. Another passive version of a micromixer is to split and recombine a lot of channels and by using inlets that are e.g. shaped as wedges, with the goal to minimize the diffusion distances and thereby also decreasing diffusion times [42]. Active versions of micromixers use the same external forces as previously discussed for micropump and microvalves, such as electrical or magnetic forces.

Droplet microfluidics

Droplet microfluidics is a method that exhibits high-throughput when dealing with biological assays [11]. This is an "all-in one" procedure that does not need multiple steps using different methods for manipulation, mixing and analysing. The most common way is to use oil as a so called carrier fluid which can encapsulate incoming aqueous fluids filled with target particles or

molecules inside of a microchannel. The aqueous solution flows in a straight manner until it reaches a branch where we have oil flowing perpendicular to it, both under and above the straight channel. This set up is called a co-flow and with the right flow rates, it creates water-in-oil emulsions or microbeads, $5 - 120$ μm in size, which are being carried forward in the the oil carrier fluid [3,11]. The goal is so encapsulate important cells, particles or molecules which will be stored or analysed further down the microdevice. This is an extremely fast event creating more than $10,000$ microbeads per second, hence the high-throughput characteristics [3]. A sorting device could also be implemented in this method if the microbeads were injected with fluorescent dyes corresponding to their biological properties at the merging region where they are encapsulated in a water-in-oil emulsion. The sorting into two, or more, different side outlets can thus be actively done by using a laser that determines what kind of particle it has optically examined, based on what color of the dye it has. Droplet microfluidics is a great tool e.g. in screening out, sorting, for how well bacteria and viruses react to drug influence, that is how many of these pathological particles will survive and still be able to merge with the microbeads [11]. The same thing goes for studying the efficiency of antibodies, analysing how many will successfully bind to a specific target molecule after incubation inside of the droplets. Another prospect that droplet microfluidics can be used for is examining polymerase chain reactions (PCR), where many copies of a DNA-template are created and amplified.

2.3 Acoustophoresis

2.3.1 History

Throughout the last century, the study of acoustic fields and its interplay and impact on small objects has lead to many intriguing revelations. August Kundt, a great German physicist who was one of the forerunners in the field of acoustics, created a way of calculating the speed of sound of gases using a tube that was vibrating at a specific frequency with dust or other small particles placed at the bottom [16]. He found out that at a specific frequency, all the particles would gather in the nodes of a resulting standing wave, making it possible to calculate the wavelength of the sound and thus also its speed. A few years later, in 1874, August Kundt together with his colleague and student Otto Lehmann further investigated the effects of acoustic forces on small dust particles [4]. Thus, the science of manipulating small objects using acoustic standing waves was born.

It was not until the last few decades that this field of science revealed its benefits to microfluidics, that is, how to integrate this phenomenon onto microchannels. In 2004, Petersson *et al.* and his colleagues realized that when a microchannel containing a fluid filled with particles of some sort, is exposed to ultrasound, typically in the 1-5 MHz range, the same effect of particles gathering in the nodes or the antinodes of a standing wave could be obtained [14]. The ultrasound was generated by using piezoelectric transducers that convert electrical pulses to mechanical vibrations. In this original study, blood containing unwanted lipids was inserted into a microchannel via the inlet channel and moved in a controlled matter thanks to the laminar flow. The frequency and geometry of the microchannel was chosen so that it would give rise to a half wavelength ($\lambda/2$) standing wave. This method had the ability to separate particles based on their size, compressibility and density. The bigger erythrocytes gathered in the node of the standing wave which lies in the centre of the microchannel and were sorted out in the centre outlet whereas the smaller lipids gathered at the antinodes, near the sidewalls and ended ut at the side outlets. A clearer picture regarding this method and its results in this study needs the introduction of the physics behind the Stokes' drag force and especially the acoustic radiation force.

2.3.2   Standing waves

To fully understand the method behind acoustophoresis, we need to get to the basics of sound theory. What we interpret as sound, is actually a result of vibrating particles in a medium, for instance air or water, after pressure has been applied to the medium. In microchannels used in acoustophoresis, these vibrations are created by applying a voltage at specific frequencies (2-5 MHz) to a PZT that is coupled to the microchannel's bottom or sides, having the ability of converting electrical signals to mechanical vibrations. The pressure waves created in the frequency region used in acoustophoresis (2-5 MHz) are called ultrasounds, which the human ear is not constructed to hear, being well above the human hearing limit of around 20 kHz.

In liquids, the spread and direction of a sound wave is strictly longitudinal, meaning that the closest particles in the medium effect each other in an oscillating manner, moving left to right, which is why compression is another common way to call this process [13]. This oscillating manner leads to a superposition process, spread throughout the whole medium where we have maximum and minimum interaction locations between the longitudinal sound waves that are incident and reflected of a boundary, such as the walls in a mi-

crochannel. The positions where the amplitudes of two meeting longitudinal waves coincide and enhance each other to a maximum are called antinodes. In the same manner, nodes are the positions where the interaction of the two longitudinal waves leads to an amplitude minimum, which explains why particles at the nodes are seen as motionless. The amplitude in this case corresponds to the longitudinal displacement. By combining this interaction of the longitudinal waves, we get so called standing waves [13], see Eq. (2.9).

$$y(x,t) = A\sin(kx)\cos(\omega t) \qquad (2.9)$$

where A is the total displacement amplitude after superposition of the longitudinal waves, k is the wave number, x is the longitudinal position, ω is the angular frequency and t is time.

The theory behind standing waves can be seen in Fig. (2.3), illustrating the pressure standing wave and displacement standing wave in (b) and (c) respectively. The mediums continuous longitudinal vibrations to the left and right can be seen in (a). The interesting fact in Fig. (2.3) is that the nodes of the pressure standing wave, (b), correspond to the compression of the particles making the particles stick closer together and thereby increasing the density around that area [13]. The other process, called rarefaction, is when the particles moves away from the pressure node, thus decreasing the density around that area in the medium. The physical changes of this increase and decrease in density, compression versus rarefaction, is seen in (a), where each particle is oscillating within its own small region.

a)

A sin(kx) cos(ωt)   A sin(kx) cos(ωt)   A sin(kx) cos(ωt)

b) Pressure standing wave

c) Displacement standing wave
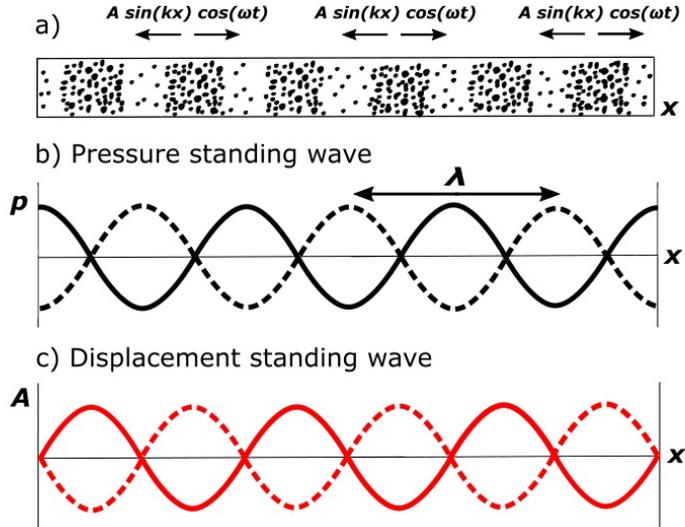
Figure 2.3: **The theory behind standing waves illustrated. (a) each particle is oscillating left and right within its own small region in the medium. Only longitudinal waves can be obtained in a liquid medium. (b) Superposition between the incident pressure wave (—) and the reflected pressure wave (- - -) result in the pressure standing wave. (c) Superposition between the incident displacement wave (—) and the reflected displacement wave (- - -) result in the displacement standing wave. The incident displacement wave corresponds to the particles in the medium moving to the right in (a) and the reflected displacement wave corresponds to the particles moving to the left.**

In this thesis, the width of the microchannel used is equivalent to half of the wavelength, $\lambda/2$, which in turn gives the so called 1st harmonics, as illustrated in Fig. (2.4), two antinodes at the sidewalls and only one node at the centre of the microchannel after superposition of two equally large but opposing pressure waves. More resonance modes can be obtained by changing the length of the microchannel so that it corresponds to multiples (n) of the half wavelength $n \cdot \frac{\lambda}{2}$, leading to higher harmonics/overtones which showcase more nodes and antinodes. A frequency of 2 MHz was used to generate the standing wave since we have the relation $\lambda = \frac{c}{f} = 750 \, \mu m = \frac{1500 \, m/s}{2 \, MHz}$
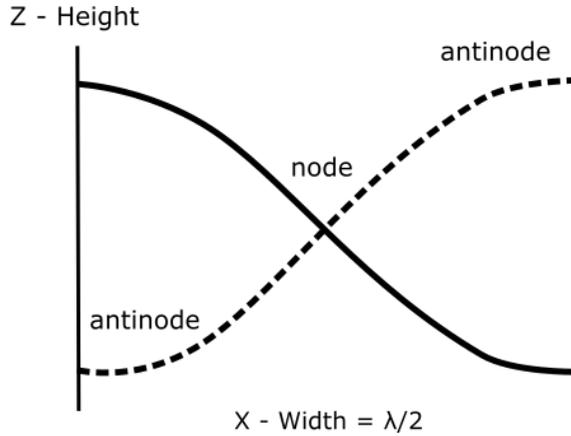
Figure 2.4: **1st harmonics for the case $X = n \cdot \frac{\lambda}{2}$, n = 1. In the centre of the microchannel lies the node of the acoustic pressure standing wave as a result after superposition of two equally large but opposing pressure waves, whereas two antinodes are present at the sidewalls of the microchannel.**

The reason why the standing waves reflect of a boundary in the first place is due to differences in acoustic impedance. At the boundaries, the reflected amount of the standing wave can by calculated by using the following equation:

$$R = \frac{Z_2 - Z_1}{Z_2 + Z_1} \tag{2.10}$$

where R is the reflected coefficient showing how much (%) of the incident pressure wave is reflected back and Z is the acoustic impedance, also denoted as the density of the medium times the velocity of sound in that medium ($\rho \cdot c$).

Eq. (2.10) tells us that when the difference between Z_1 and Z_2 of the two different mediums is large, the R coefficient also becomes large, indicating that most of the incident wave is reflected back to the first medium, whilst only a small fraction is transmitted straight through. This big difference in acoustic impedance is achieved in acoustophoresis when using aqueous solutions as the first medium (Z_1) and the microchannels sidewalls made out of silicon, acting as the second medium (Z_2).

2.3.3 Acoustic energy density - $\mathbf{E}_{ac}$

The acoustic energy density E_{ac} is a direct relation to the transverse pressure standing wave that is applied to a microchannel through the coupled PZT. The relation can be written as:

$$E_{ac} = \frac{p_a^2}{4\rho_0 c_0^2} \tag{2.11}$$

where p_a is the amplitude of the pressure standing wave, ρ_0 is the density of the medium and c_0 is the speed of sound inside the medium.

In this thesis, E_{ac} is of great importance since it was used as a fitting parameter when fitting the experimental data of PS-bead velocities to theoretical models for acoustophoretic particle motion. These theoretical models will be discussed further in section 2.5.

2.3.4 Stoke's drag force

Since we are in the low Re-number region, in the field of microfluidics, the particles in a fluid will move in a controlled matter thanks to the laminar flow. As mentioned earlier, the viscous forces dominate over the inertial forces. When trying to manipulate and push particles to the middle of a microchannel using acoustic standing waves, at the onset of ultrasound we have that the friction force equals zero whilst the acoustic radiation force accelerates the particle forward ($F_{rad} > F_d = 0$). The frictional force is better known as the Stokes' drag force F_d and can be described by the Stokes' law [13]:

$$F_d = 6\pi a\eta u \tag{2.12}$$

where a is the radius of the particle, η is the dynamic viscosity of the fluid and u is the particles velocity.

The Stokes' law shows us that when the velocity increases, F_d increases linearly with the velocity. After only about 1 μs, the particle will reach a velocity where we have the condition $F_d = F_{rad}$. After this stage, the particle moves at this constant velocity. Thus, if we know the velocity of a particle with known size, it is possible to calculate the force it is exposed to.

Eq. (2.12) is based on a few assumptions, namely that the particles are seen as entirely spherical, the fluid is incompressible, the flow is laminar and no interaction between particles may occur which can alter the flows dynamic. The streaming lines of a laminated fluid and the forces acting on particle/beads can be seen in Fig. (2.5).
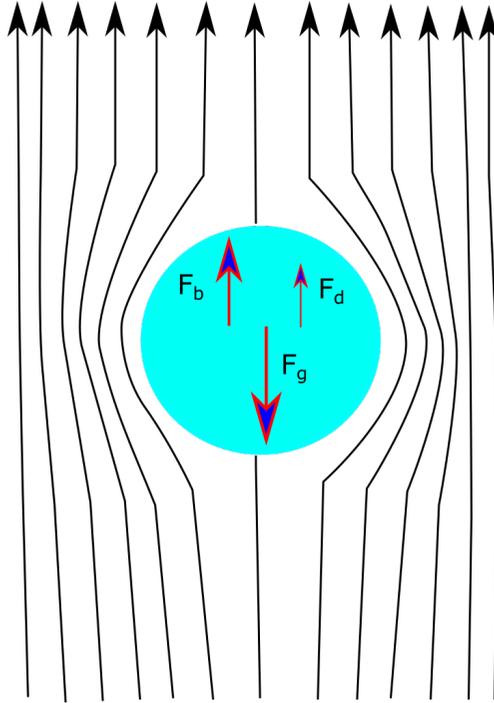
*Figure 2.5: **The fluid flows smoothly around the spherical particle. The Stokes' drag force is denoted as $F_d = 6\pi a\eta v$ which can be seen as a frictional force opposing to the gravitational force pulling down the particle, $F_g = mg$. The buoyancy force, $F_b = (\rho_p - \rho_m)gV_p$ equals the weight of the liquid being displaced by the particle. Since we have laminar flow, $Re < 1$, the net force is zero which means that $F_b + F_d = F_g$ [34].***

2.3.5 Acoustic radiation force

The goal in acoustophoresis is to manipulate particles based on their size, density and compressibility. The acoustic radiation force, ARF, which acts on particles suspended in a fluid, is a direct result of the difference in acoustic properties between the particles and the fluid surrounding them while being affected by an acoustic standing wave [13–15, 17, 18]. It can be divided into the primary- and the secondary acoustic radiation force, PARF and SARF respectively.

The PARF on a spherical particle is the dominant force of these two, since it dominates on longer distances whilst SARF dominates when particles are really close to each other and can interact. In this work we limit ourselves to working with dilute suspensions and will therefore neglect the impact of the SARF. When considering a half wavelength standing wave approach, the PARF can be described by the following equation [18]:

$$F_{rad} = 4\pi\Phi(\beta,\rho)a^3 k_x E_{ac} \sin(2k_x x) \tag{2.13}$$

where

$$\Phi(\beta,\rho) = \frac{5\rho_p - 2\rho_m}{2\rho_p + \rho_m} - \frac{\beta_p}{\beta_m} \tag{2.14}$$

Φ - *acoustic contrast factor*
p - particle
m - medium

$$E_{ac} = \frac{p_a^2 \beta_m}{4} = \frac{p_a^2}{4\rho_0 c_0^2} \tag{2.15}$$

a - radius of particle/bead
x - positions along the width of the microchannel
$k = 2\pi/\lambda$ *- wave number*
β *- compressibility*
ρ *- density*
c - speed of sound
E_{ac} *- acoustic energy density*
p_a *- acoustic pressure amplitude*

Combining Eq. (2.12) and Eq. (2.13), it is possible to calculate the velocity of the particles whilst only being affected by the PARF since we have an equilibrium, $F_d = F_{rad}$. This purely horizontal velocity u_{rad} is being showcased in the following equation [18]:

$$u_{rad} = \frac{F_{rad}}{6\pi a\eta} = \frac{dx}{dt} = \frac{2\Phi(\beta,\rho)}{3\eta} a^2 k_x E_{ac} \sin(2k_x x) \tag{2.16}$$

where

η - viscosity of the medium

Fig. (2.6) illustrates how particles with a positive acoustic contrast factor tend to move towards the node at the centre, whereas particles with a negative acoustic contrast factor instead move towards the antinodes located at the microchannel's sidewalls. In an acoustophoretic microchannel of this type, there are three outlets disposed at the end of its length. One central outlet for the particles with a positive contrast factor and two side-outlets for the particles with a negative contrast factor at the sidewalls. This can be related to the original study where red blood cells were separated from lipids which was previously discussed in section 2.3.1.
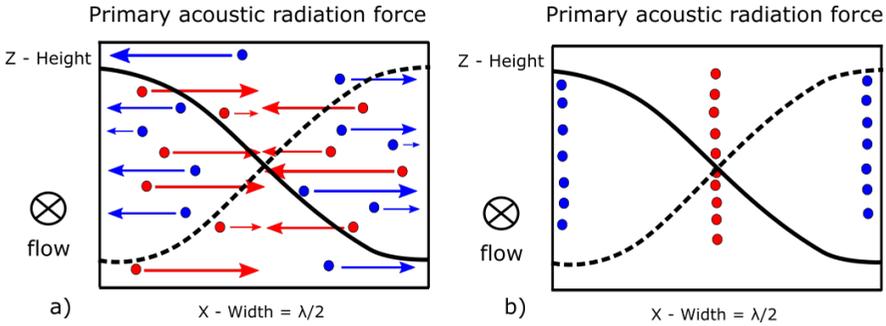
Figure 2.6: **Primary acoustic radiation force. (•) – particles with a negative acoustic contrast factor. (•) – particles with a positive acoustic contrast factor. (a) All the particles are randomly spread inside the microchannel initially. (b) After acoustic radiation, the focusing of the particles is seen at the node (centre) and antinodes (sidewalls). The particles mainly travel with the horizontal velocity u_{rad}. The relation in this particular setup is that the width of the microchannel equals half of the wavelength, $X = \frac{\lambda}{2}$. The direction of the flow ($\otimes$) is perpendicular to the acoustic pressure standing wave.**

2.4 Boundary driven acoustic streaming

Acoustic streaming is a special phenomenon that presents itself when trying to manipulate extremely small particles using standing waves inside of a microchannel. The characteristic appearance of circular streaming vortices is related to the small viscous boundary layer δ (- - -), as seen in Fig. (2.7). The thickness of this region lies around 0.38 μm for the setup used in this thesis. The bulk flow with the circular streaming pattern is called Rayleigh streaming, having its maximal velocities at the top and bottom of the microchannel [13]. As previously explained, we have a "no slip condition" at the walls of a microchannel, meaning that a viscous solution has zero velocity at the boundaries. This confined geometry means that inside of the viscous boundary layer δ, the acoustic energy from the standing wave must dissipate quickly since the acoustic oscillations are absorbed by the solid boundaries and this results in a circular movement, called Schlichting streaming [13]. This counter-rotating circular pattern, (↺, ↻) Fig. (2.7), as it spreads out more and more, is what drives the bulk fluid flow inside of the microchannel. There are different types of acoustic streaming but the confined geometry of the microchannel used in this thesis, w = 375 μm and h = 150 μm, was affected by the so called boundary driven acoustic streaming, as illustrated in its enterity in Fig. (2.7). From now on, when mentioning acoustic streaming, boundary driven acoustic streaming is actually considered.
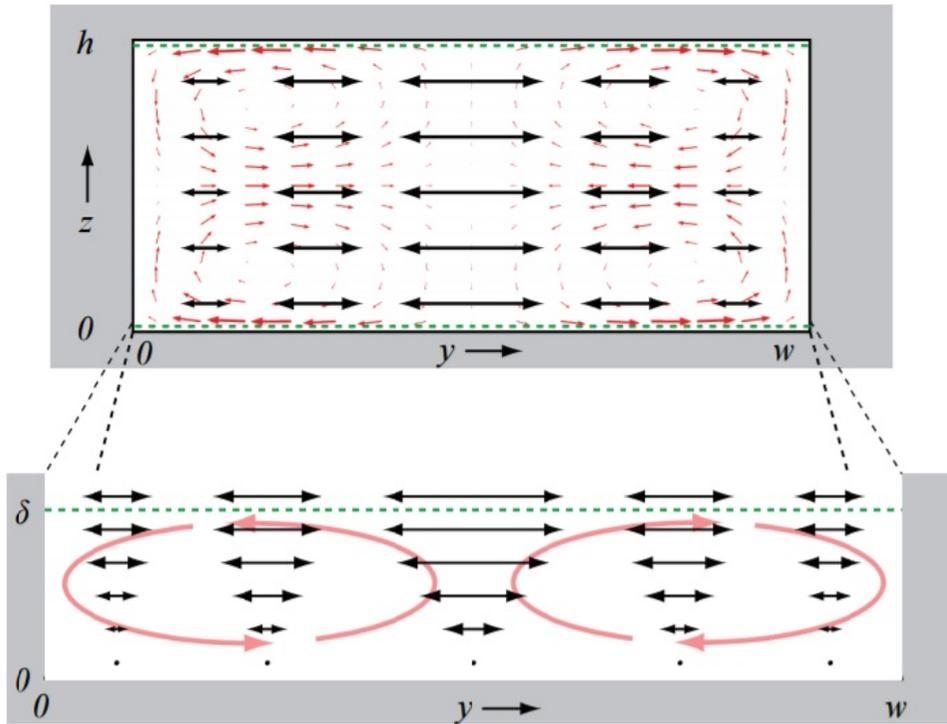
Figure 2.7: ***Boundary driven acoustic streaming as seen in the transverse cross section of a microchannel, w denoting the width and h corresponding to the height. The Schlichting streaming (↺, ↻) can be seen inside of the viscous boundary layer δ (- - -), giving rise to the bulk fluid flow called Rayleigh streaming. The streaming trajectories are denoted as (→) and the oscillating first acoustic velocity field as (←→). Adapted with permission from Per Augustsson [18].***

The boundary driven acoustic streaming, which this thesis focuses on, was first explained by Lord Rayleigh, hence the name, just outside of the acoustic boundary layer as the bulk fluid flow [25, 27]:

$$u_{str} = u_{str}(x) + u_{str}(z) \tag{2.17}$$

where

$$u_{str}(x) = \frac{3}{16} \frac{4E_{ac}}{\rho_w c_w} \sin\left[2k_x\left(x + \frac{w}{2}\right)\right] \left(1 - 3\frac{z^2}{(h/2)^2}\right) \tag{2.18}$$

and

$$u_{str}(z) = \frac{3}{16} \frac{4E_{ac}}{\rho_w c_w} k_x h \cos\left[2k_x\left(x + \frac{w}{2}\right)\right] \left(\frac{z^3}{(h/2)^3} - \frac{z}{h/2}\right) \tag{2.19}$$

with

w - width of the channel
h - height of the channel
x - positions along the width of the channel
z - positions along the depth of the channel
E_{ac} - acoustic energy density
k_x - wave number
ρ_w - density of water
c_w - speed of sound in water

Acoustic streaming is usually dominating over the acoustic radiation force when we have particles smaller than around 1 μm. This size region falls in line with different bacterias and viruses which are important for medical diagnostics. The mixing nature of the acoustic streaming is hampering the possibility of good focusing and separation when dealing with these small particles in acoustophoresis. This is why this thesis will discuss the possibility of suppressing acoustic streaming.

2.5 Total acoustophoretic velocity of a particle inside of a microchannel

Since the PS-beads are affected by the ARF and the acoustic streaming simultaneously, Eq. (2.16) and Eq. (2.17) are added together in order to obtain the total velocity of the beads which is denoted as:

$$u_{tot} = u_{str} + u_{rad} \qquad (2.20)$$

In this project, the experimental data of the velocities were obtained as vectors in Matlab, see Appendix B for code. During the analysis of the results, as will be discussed more in detail in chapters 6-7, the magnitude of this total velocity was also used giving the relative size of the velocities from the experiments:

$$u_{mag} = \sqrt{u_{str}^2 + u_{rad}^2} \qquad (2.21)$$

Still, Eq. (2.21), has a lot of assumptions and important parameters that are not being considered, especially when using Rayleigh's classical equation for acoustic streaming, Eq. (2.17). For instance, u_{str} requires that the wavelength is much larger than the height of the microchannel ($\lambda \gg h$), but in the case of this project we rather have a ratio of $\lambda = 5h$ ($\lambda = 750\mu$m and h = 150μm).

The basis of a different channel geometry lead to an extended version compared to the one in classical Rayleigh's acoustic streaming described by (Muller, 2012, referred by Barnkob, 2012). This can also be combined with the aspects of thermoviscous correction due to the temperature dependent nature of the viscosity η as proposed in (Radnikov *et al.*, 2011, referred by Barnkob, 2012) together with wall corrections due to single-particle drag (Happel *et al.*, 1983, referred by Barnkob, 2012). The outcome of these findings resulted in a more complete and credible description of the acoustophoretic motion of beads and particles.

Thus, an extended version using these new insights and only taking the horizontal component of u_{tot} into consideration was used in this project for comparison with the more classical view in Eq. (2.20). The complete equation is described as follows [27]:

$$u_{tot}(x) = \left[\frac{1}{\chi(a)} \frac{a^2}{a_o} + s^T_{\lambda \approx 5h} \right] \frac{4E_{ac}}{\rho_w c_w} \sin \left[2k_x \left(x + \frac{w}{2} \right) \right] \qquad (2.22)$$

where

$$a_o = \delta \sqrt{\frac{3}{\Phi}} \qquad (2.23)$$

with

a - radius of the PS-bead
w - width of the channel
x - positions along the width of the channel
E_{ac} - acoustic energy density
k_x - wave number
ρ_w - density of water
c_w - speed of sound in water

$s^T_{\lambda \approx 5h}$ - thermoviscous correction factor combined with the geometry correction for the case $\lambda = 5h$

$\chi(a)$ - wall correction coefficient

δ - width of the viscous acoustic boundary layer
Φ - acoustic contrast factor for a PS-bead

More on which values of these parameters that were used in this thesis will be discussed in chapter 6.

2.6 Iso-acoustic focusing

Iso-acoustic focusing is a rather new method that makes it possible to separate and focus various particles depending on their intrinsic acoustic characteristics and is thus size-independent, unlike ordinary acoustophoresis [19]. A liquid of inhomogeneous properties, like the density gradient medium iodixanol, is laminated into a microchannel together with the particle solution. After the flow is stopped, the heavier iodixanol solution will slowly move towards the bottom of the microchannel. After acoustic actuation, we will obtain a medium condition as seen in Fig. (2.8a). The density gradient medium will focus and stabilize towards the node of the $\lambda/2$-standing wave, pushing the particle solution towards the sidewalls of the microchannel. In this inhomogeneous medium, the particles will gradually sense and move towards an increasing acoustic impedance, all the way to their specific *iso-acoustic point*, which is where the acoustic impedance of the medium equals the acoustic impedance of the particles/cells used, see Fig. (2.8). At this position, a particle stops moving laterally ($u_{rad} = 0$) since the acoustic radiation ceases to influence it, thus proving that an iso-point is directly coupled to each particles individual acoustic properties. In addition to focusing and separation of the particles, there are hopes that this approach can improve existing systems for characterization of different cell types [19]. One big possibility would be to characterize different white blood cells which are similar in size but with completely different immunological properties and tasks. Iso-acoustic focusing not only affects the individual particles, but also the entire medium. The study on IAF also showed that after altering the concentration of the medium, it was possible to modify the acoustic contrast factor of the used particles/-cells.
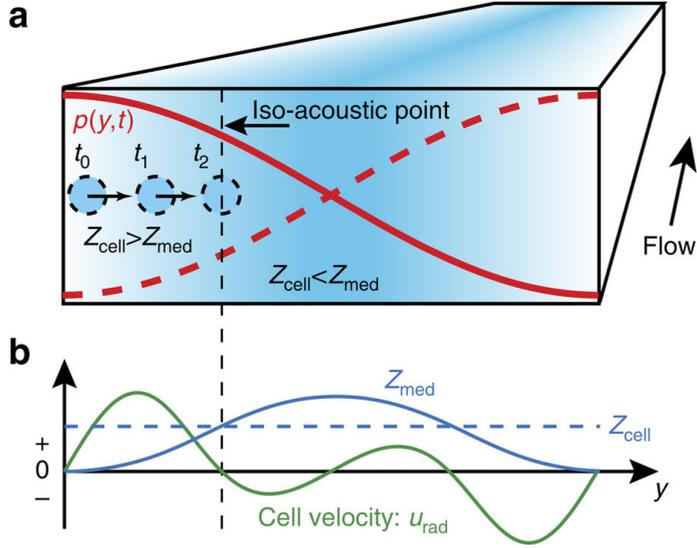
Figure 2.8: ***The IAF- method, seen in the transverse cross section of a microchannel. (a) After acoustic actuation, the heavier density gradient medium (blue color) moves towards the centre of the microchannel where the node of the $\lambda/2$ standing wave (—) lies, whilst the particles/cells (•) are simultaneously being pushed to the sidewalls. Then, they are moving laterally influenced by the acoustic radiation force towards their specific iso-acoustic point, the position where the acoustic impedances of the particles and the medium are equal to each other ($Z_{cell} = Z_{med}$). (b) The iso-acoustic point corresponds to the positions where we have the conditions ($Z_{cell} = Z_{med}$) and ($u_{rad} = 0$). Adapted with permission from Per Augustsson [19].***

One major drawback with acoustophoresis is its size-dependency, which takes the form of acoustic streaming for particles with a radius smaller than around 1μm as earlier mentioned. Acoustic streaming simply mixes the solution, hampering the possibility for acoustic fosusing and separation of particles using acoustic manipulation. It is believed that IAF has an ability to suppress this acoustic streaming with the help of the inhomogeneous properties. The results of these investigations will be discussed in chapter 7.

2.7 Particle tracking using an astigmatic defocusing optical system: GDPT combined with the use of a cylindrical lens

The method of general defocusing particle tracking (GDPT) is used to track and detect the x-, y- and z-positions of small particles in motion using optical imaging and can be applied in LOC-systems, as for instance in acoustophoresis [37]. The z-position (depth position) of a particle, inside of a microchannel, is estimated by analyzing how far out of focus a specific particle is based on how it is imaged through an optical setup. In the GDPT-software, acquired images filled with particles (target images) are compared statistically, by means of cross-correlation, with a number of reference images used for calibration. The reference images are taken at different depths of the microchannel, for instance with a step-size of 2 μm between each taken image, saving these "image-slices" in large stacks, serving as a library. When comparing a target particle with all of the reference particles in the "image library" and eventually a peak in the cross-correlation function is met, it means that the specific reference image for which this occurred is the most similar to the target particle. In this way one can determine the z-position of the captured particle [37]. By analyzing a selected sequence of images, it is made possible to determine the motion/trajectories and corresponding velocities of the individual particles. Thus, we obtain an imaging of the flow field of the liquid and the particle motion in the microchannel in three dimensions. An explanatory manual of how to use the GDPT-software, written by the author of this thesis, can be seen in Appendix C.

The PS-beads used in this project were spherical, thus also being symmetrical in their appearance around the focus depth, giving the GDPT-software a hard time determining if a target particle lying close to the focus, was either slightly under it or above it. This symmetry could be broken by introducing a cylindrical lens between the camera and the objective inside of the microscope, a procedure typically used in astigmatic defocusing optical systems. The focusing aspect relates to the alternation of particle intensity in the images when moving away from the focus (decreasing intensity) or moving towards the focus (increasing intensity). Further, in an astigmatic system, the optical set up, using a cylindrical lens, is ordered in such a way that particles, depending on where they are located in the microchannel, will always only be magnified in one direction [38]. If a bead/particle is slightly above the focus, it appears to be altered/magnified vertically and if it is located slightly

under the focus, it will be altered/magnified horizontally. These concepts are described in detail and visualized in Fig. (5.3), in section 5.2, covering the results when evaluating the GDPT-analysis using 3 μm PS-beads.

CHAPTER 3

PURPOSE AND AIMS OF THE PROJECT

There have been qualitative observations related to the IAF, which indicate that acoustic streaming behaves completely different in liquids with inhomogeneous density and compressibility compared to the homogeneous liquids [19].

The overall goal of this project was to explore the method of IAF on a deeper level by using density gradients and in particular to study and quantify the suppression of acoustic streaming. In order to showcase the trajectories of the suspended particles, a sufficient particle tracking method was needed and the choice fell on the fairly new method GDPT - General Defocusing Particle Tracking. This thesis was divided into three aims:

Aim 1 - Evaluate GDPT for measuring 3D fluid flow in microchannels

- Get acquainted with existing equipment for acoustophoresis and IAF
- Identify necessary new or modified equipment for the project
- Determine how to control the flow
- Establish sample preparation protocol
- Study the GDPT-software and theory behind it
- Carry out a complete GDPT-analysis - calibration and 3D particle tracking for 3 μm PS-beads

Aim 2 - Study acoustic streaming in homogeneous medium

- Actuate an acoustic pressure field to the homogeneous medium
- Carry out GDPT-analysis for 1 μm and 4.8 μm PS-beads
- Measure the acoustic energy density E_{ac}
- Measure the total velocity of the PS-beads, both the acoustic streaming and the velocities induced by the acoustic pressure field.
- Solve and validate these results analytically using theoretical equations describing acoustophoretic particle motion.

Aim 3 - Study acoustic streaming in fluids of inhomogeneous density and compressibility

- Create an inhomogeneous medium with density gradients using water and a solution of iodixanol (20%)
- Actuate an acoustic field to the inhomogeneous medium
- Carry out GDPT-analysis for 1 μm
- Examine the results and compare with the results for homogeneous medium.

CHAPTER 4

METHODS

The entire experimental setup to quantify acoustic fields and acoustic streaming, its components, and in what manner they were used will be explained in detail in this following section. The entire experimental setup can be seen in Fig. (4.1).
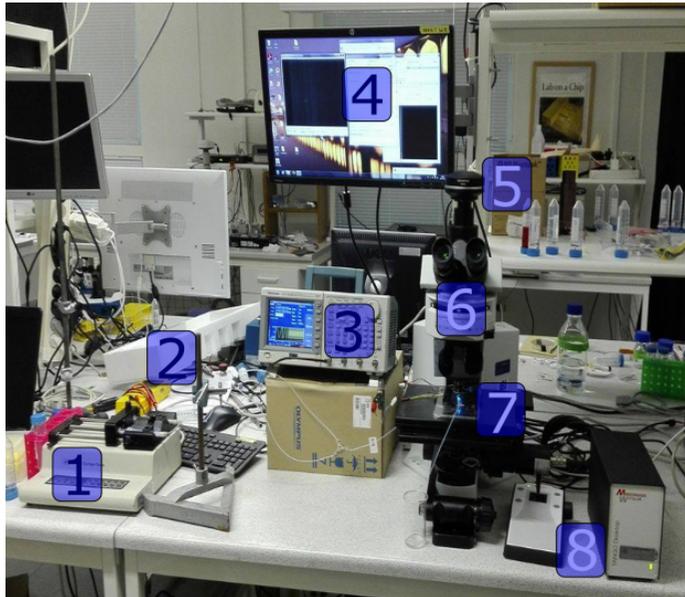

Figure 4.1: **The entire experimental setup. 1 – Syringe pump. 2 – Valve.**
3 – Function generator. 4 – Computer. 5 – Camera. 6 – Microscope.
7 – Microchannel. 8 – Joystick and controller for microscope stage.

Furthermore, a schematic overview of the experimental setup is illustrated in Fig. (4.2). During aim 2 and 3, the syringe pump was set to a mean flow rate of 100 μl/min. The flow of the solutions was opened and closed when needed, with the help of a valve. The microchannel only had one inlet and one outlet. During aim 3, the PS-bead- and iodixanol solutions needed to be laminated before entering the microchannel and this was done using a bifurcation. A function generator was applying a specific voltage to the PZT placed at the side of the microchannel, which gave rise to the standing wave with an orientation perpendicular to the flow. The waste was collected into a bowl.

The optical setup consisted of an upright epifluorescent microscope, a camera and a joystick and controller for the microscope stage. These components also communicated with an image acquisition program on a computer, called Micromanager.
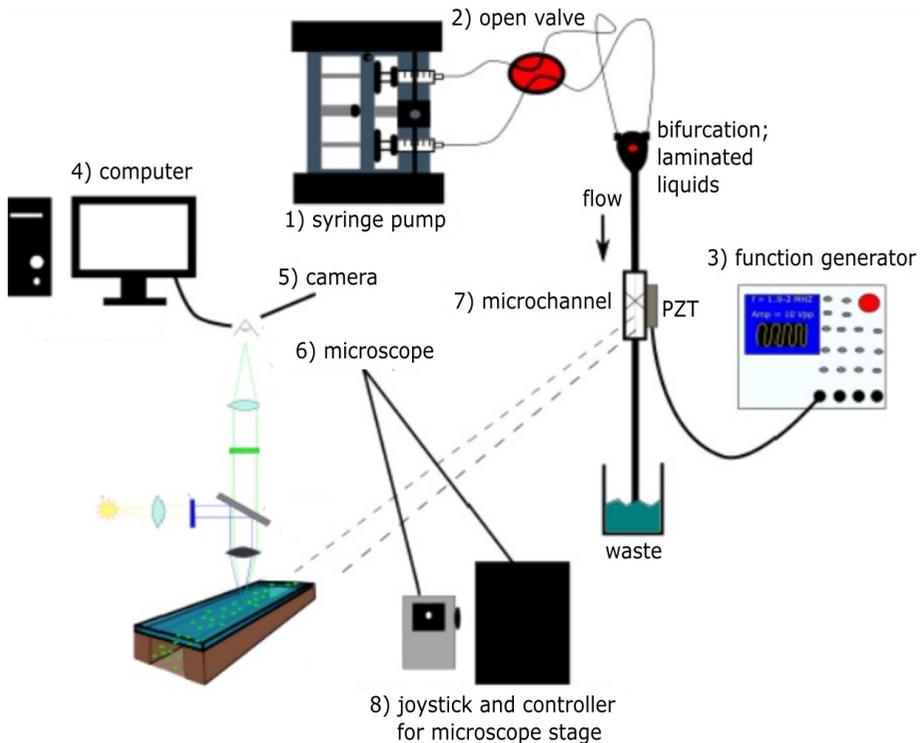
*Figure 4.2: **A schematic overview of the experimental setup.***

4.1 Material and general execution

4.1.1 Microchannel

The microchannel, see Fig. (4.3), with its rectangular shape was made by photo lithography and anisotropic KOH wet etching of a <100> silicon wafer. On top, the microchannel was sealed using glass. The dimensions were 375x150 μm, width and height respectively, with a channel length of 35 mm. It consisted of only one inlet and outlet.
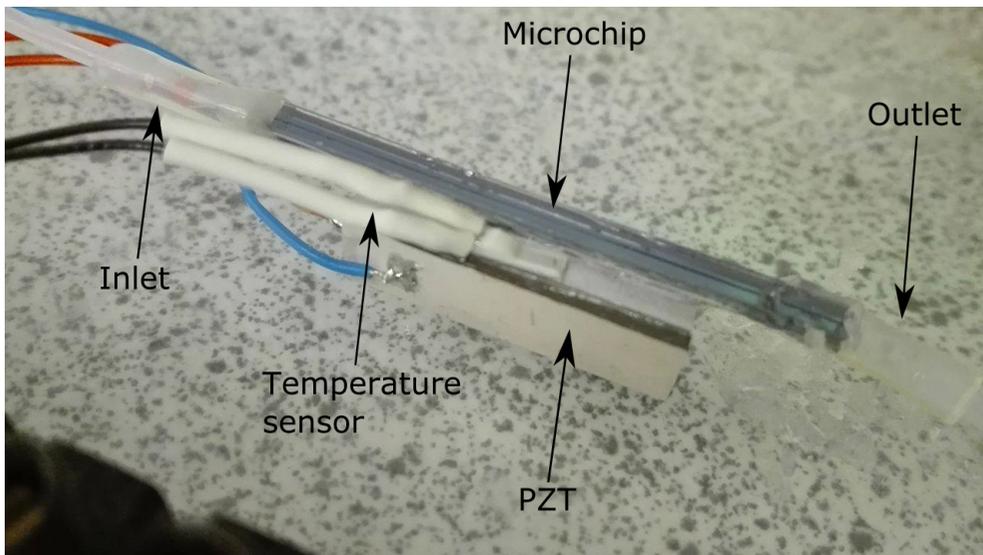
Figure 4.3: ***Close-up of the microchannel and its surrounding components. The inlet and outlet are stabilized with silicon, reducing leakage and clogging. PZT - piezoelectric transducer located at the side of the microchannel. The temperature sensor was not used.***

4.1.2 Optical setup

The optical setup consisted of the microscope, the camera and the joystick and controller for the microscope stage, which now will be described more in detail.

Microscope
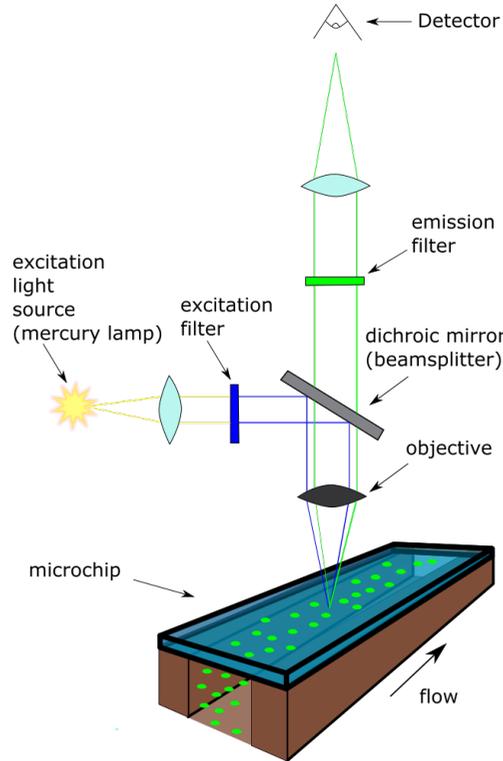
*Figure 4.4: **A schematic illustration of an epifluorescent microscope which was used in this project. The PS-beads were excited by light with specific wavelengths and the resulting fluorescent emission was detected.***

An upright epifluorescent microscope (*Olympus BX51W1*) was used during these experiments. In such a microscope, the sample is illuminated from above, as seen in Fig. (4.4). A mercury lamp was used as the illumination source. The role of the excitation filter is to filter out the specific wavelengths for which the sample, in this case the PS-beads in the microchannel, would be excited [26]. The emitted fluorescence for these PS-beads lies in the green wavelength region, ~ 525 nm, and the excitation wavelength, ~ 490 nm. The light from the excitation filter, Fig. (4.4) blue lines, is reflected from the

dichroic mirror and thus directed towards the sample. After excitation, the resulting emission from the PS-beads, Fig. (4.4) green lines, is freely transmitted through the dichroic mirror and the more wavelength-selective emission filter, before reaching the detector of choice (eye or camera). During these experiments, the images were acquired around the middle of the microchannel's length, $\sim$ 20 mm from the inlet, see Fig. (4.5).
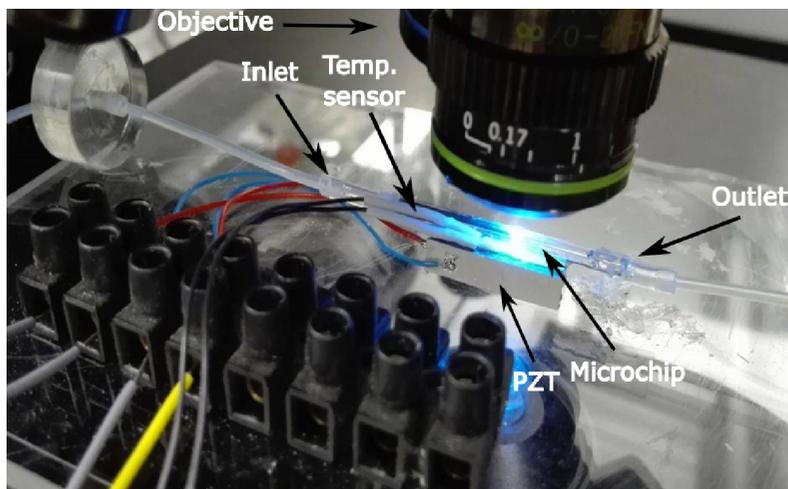
Figure 4.5: **Position on the microchannel where the images were acquired, $\sim$ 20 mm from the inlet. A 10x objective was used. The inlet and outlet of the microchannel can be seen and also the position of the PZT (Piezoelectric transducer). The temperature sensor was not used.**

Camera

The (*Olympus XM10*) was used as the camera for the image acquisition process. It is a high sensitive CCD-camera with a resolution of 1376x1032 pixels and capable of managing high frame rates. During these different experiments 1-10 fps were used. The program *cellSens Entry* was initially used as the viewing software before completely switching to *Micromanager*.

Figure 4.6: **Camera used during the image acquisitions.**

Cylindrical lens

A cylindrical lens was put between the camera and the microscope's objective in order to obtain images that made the GDPT-analysis easier, having vertical and horizontal lines as a focus of the PS-beads, instead of only as a point. The reason and mechanism behind this implementation was explained in the section about GDPT, relating to astigmatic defocusing systems.

Joystick and controller for the microscope stage
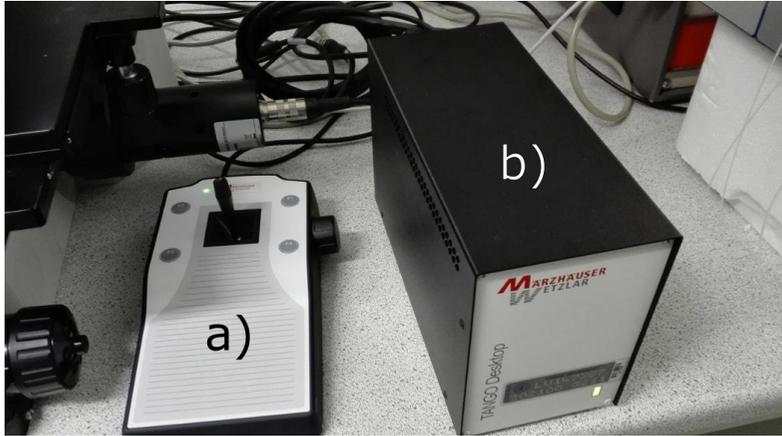
Figure 4.7: **Equipment used for controlling the microscope stage; (a) joystick, (b) controller.**

The stage controller (*Tango Desktop by Märzhäuser Wetzlar*), see Fig. (4.7b), was used to control and shift the microscope's stage motors in the three directions x,y and z of the microchannel. It was used both automatically by the program *Micromanager* during the image acquisitions and manually by using the joystick, see Fig. (4.7a), when needed to navigate by hand.

4.1.3   Actuation of acoustic field

And acoustic pressure standing wave was generated with the help of a function generator (*Tekronix AFG3022B Dual Channel Arbitrary Function Generator*) connected to a piezoelectric transducer which was located at the side of the microchannel as can be seen in Fig. (4.3). The frequency range was chosen as a linear sweep between 1.9 - 2.1 MHz with an interval/period of 1 ms. The amplitude was set to 6 V_{pp} during the experiments of aim 2 and 10 V_{pp} during aim 3.

4.1.4   Flow setup

During initial experiments (aim 1), the flow setup was very basic, only having one syringe containing the PS-beads solution connected to the inlet of the microchannel. When acoustic actuation and the density gradient medium were introduced later on, a syringe pump (*SP210IWZ Syringe Pump*) was added in order to control the flow rates of the solutions used, see Fig. (4.8). The

flow rate was only managed before the inlet of the microchannel and was set to 100 µl/min. The microchannel had only one inlet and outlet, but a bifurcation before the inlet made the two liquids laminate next to each other, prior to entering the microchannel.

Figure 4.8: **The syringe pump set up showing the iodixanol- and PS-bead solutions during aim 3. The flow rate was set to 100 µl/min.**

A valve was used to start and stop the flow when needed, see Fig. (4.9). It had four inlets which it could direct the flow with. By watching the icon on the valve, and which way it was turned, it was possible to know the state of the flow. If it was switched to the left, (a), the flow was open and correspondingly the flow was closed when the valve was switched to the right, (b).
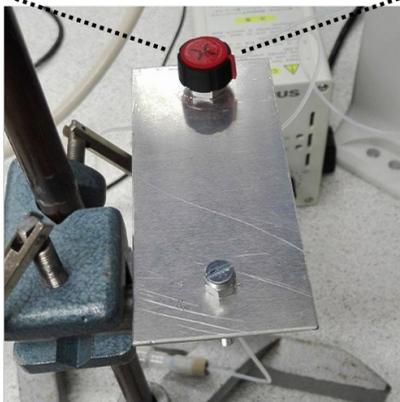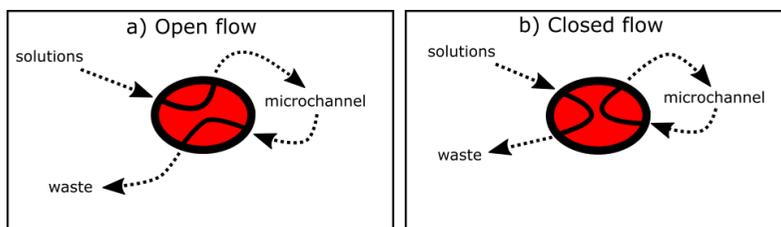
Figure 4.9: **How the valve controls the flow: (a) Left side switch means open flow. (b) Right side switch means closed flow.**

During aim 2, the flow was mainly stopped when image acquiring needed to be done. The valve was especially important during aim 3, where the PS-beads solution and iodixanol needed to be mixed in order to see the difference between inhomogeneous and homogeneous medium. This execution will be clarified more in chapter 7.

4.1.5   Sample preparations

Sample preparation was another factor that needed to be sorted out before initial testings of the GDPT-analysis. It needs to be pointed out that the concentrations of the PS-beads are crucial to how effective the GDPT-analysis would be. This was hard to tell in advance so different concentrations were tested until arbitrary and promising results were obtained. However, after reading the GDPT-manual, it was understood that it needed to be a decent amount of beads, too few PS-beads and no quantitative results would be attained showing the trajectories only in some parts of the microchannel, too many PS-beads and the segmentation process would be impossible to do, making the resulting trajectories misleading or completely wrong since the PS-beads could not be distinguished from one another.

The first solution used was containing 3 μm PS-beads, 10ml MQ water and 100 μl Triton X-100, preventing the particles to form clusters. The size of these beads was later changed to 4.8 μm, bigger beads being affected more by the ARF, whilst the smaller beads were 1 μm at all time. Complications in the GDPT-analysis arose when trying even smaller beads.

The iodixanol solution (OptiPrep™ 60%) used as the density gradient medium was diluted to 20%, at a ratio of 1:2 with the buffer used in the PS-bead solution (MQ-water and Triton X-100). The final and best suited solutions containing the PS-beads and the density medium can be seen in Tables 4.1-4.2.

*Table 4.1: **Solutions used - 1μm particles - 10x objective.***

Solutions	
PS-bead solution	*iodixanol solution (20%)*
PS-beads - 5μl	OptiPrep™ - 1 part
MQ-water - 40ml	MQ-water + Triton X-100 - 2 parts
Triton X-100 - 100μl	

*Table 4.2: **Solutions used - 4.8μm particles - 10x objective.***

Solutions	
PS-bead solution	iodixanol solution (20%)
PS-beads - 10μl	OptiPrep™ - 1 part
MQ-water - 40ml	MQ-water + Triton X-100 - 2 parts
Triton X-100 - 100μl	

4.1.6 Method for calibration - making the 1 μm PS-beads motionless

The difficulty when trying to acquire a stack of images for the calibration, when using the smaller 1 μm PS-beads, was that they would not sediment as well or fast as the bigger ones. The larger 4.8 μm PS-beads sedimented down to the bottom of the microchannel in a matter of seconds, resulting in motionless PS-beads, being perfect data for the calibration analysis.

In order to obtain a calibration stack for the smaller 1 μm PS-beads, it was needed to make them stick to the bottom of the microchannel or the top. The method behind this was rather straight forward. Triton X-100, the substance that prohibited the PS-beads of merging into each other, was removed while the concentration of the 1μm PS-beads was increased significantly. This new solution of beads, suitable only for the calibration, was then inserted into the microchannel, hoping for some PS-beads to get stuck. To increase the chance of this to happen even further, the acoustic field was turned on. Finally, when one or more PS-beads were seen to be stuck, the microchannel was washed off with MQ-water until only the motionless and stuck PS-beads remained.

4.1.7   Image acquisition softwares

Micromanager

Micromager is an open source microscopy-software which automated the entire image acquisition process in these experiments, since it was possible to externally communicate with the Tango Desktop stage controller. The PS-beads could be seen in real time with a live playback option on the computer, making it easy to set correct image parameters, such as exposure time, gain, frame rate and binning. The calibration image stacks were obtained using an option called "Z-stacks (slices)," where the step between each depth in the Z-direction was set and also the starting and ending point of the image acquisition. The images used for the upcoming GDPT-analysis were taken with the option called 'Time Points', where the number of images and frame rate could be chosen.

cellSens Entry

cellSens Entry was the initial image acquiring program used in the beginning of the project since the software was directly coupled to the Olympus camera. It had good functions with almost the same possibilities as *Micromanager* but the reason for the switch was that the saving method of the image stacks was not efficient and a separate software for automation of the image acquisition process was needed.

SwitchBoard

This was the software used together with *cellSens Entry* in order to automate the image acquisitions at the depth direction by creating a list of depth positions in advance, where the stage controller would move to and thereafter obtain and save images. The need of *SwitchBoard* dissapered with the introduction of *Micromanager*.

4.1.8 Particle tracking analysis software

The particle tracking and velocity calculations were analysed in *Matlab, version R2016a*, using a software for GDPT obtained from Rune Barnkob [37]. A walk through of this software and how it is used can be seen in Appendix C. Own code written for extracting and filtering of the results obtained from the GDPT-analysis can be seen in Appendix B.

CHAPTER 5

EVALUATE GDPT FOR MEASURING 3D FLUID FLOW IN MICROCHANNELS (AIM 1)

In order to measure acoustic fields in microchannels and the motion of micro-scopical beads, an efficient particle tracking method is needed. The following sections describe how the GDPT-software was tested and used early on.

5.1 Defocused particle tracking

During the particle tracking, the x-, y- and z-positions were studied with the GDPT-software. The defocused images of the PS-beads correspond to different depths inside of the microchannel. By tracking the PS-beads frame by frame, it is possible to obtain and measure their speed and compare these results by adding different conditions. First, the initial testing of the image acquisition process will be described, after which a complete GDPT-analysis, containing both the calibration and results of the particle tracking will be shown.

5.1.1 Method

Using the program *cellSens Entry* that was linked to the Olympus microscope, it was possible to observe live images of the microchannel's inside. These live images were seen on a computer screen since *cellSens Entry* was able to

communicate with other platforms. The determination of when the focus of the microscope was at the bottom or at the top of the microchannel was also dealt with these live images, not only relying on the microscope view. The exposure time was set to 20 ms and the gain was set to the value of 0. In total, the first testing attained eight images with 6 μm between each taken image. The depth was changed in each direction manually, away from the bottom in order to see how long out of focus the images could be taken and still show recognizable PS-beads.

5.1.2 Results and discussion

The images were initially analysed in the program *imageJ* and the results can be seen in Fig. (5.2). A random PS-bead was chosen and tracked at different depths with the fluorescence intensity being analysed, see Fig. (5.1).
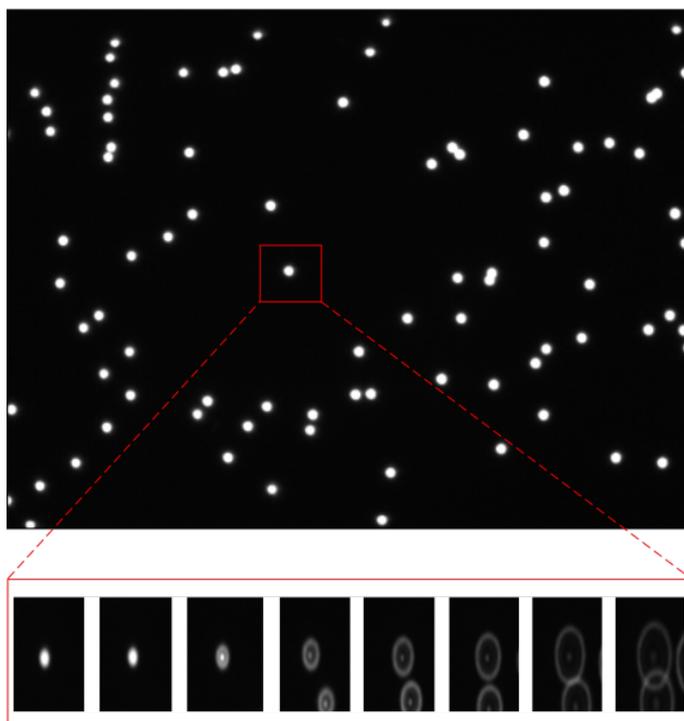
Change in z-position (vertical): 6 µm between each frame

*Figure 5.1: **The chosen PS-bead** (□) **at a few depths (Z-positions) showing the defocusing effect. The smallest image furthest to the left lies in focus and the forthcoming images show the intensity decrease as the depth is changed. The size of the PS-beads is 3 μm.***
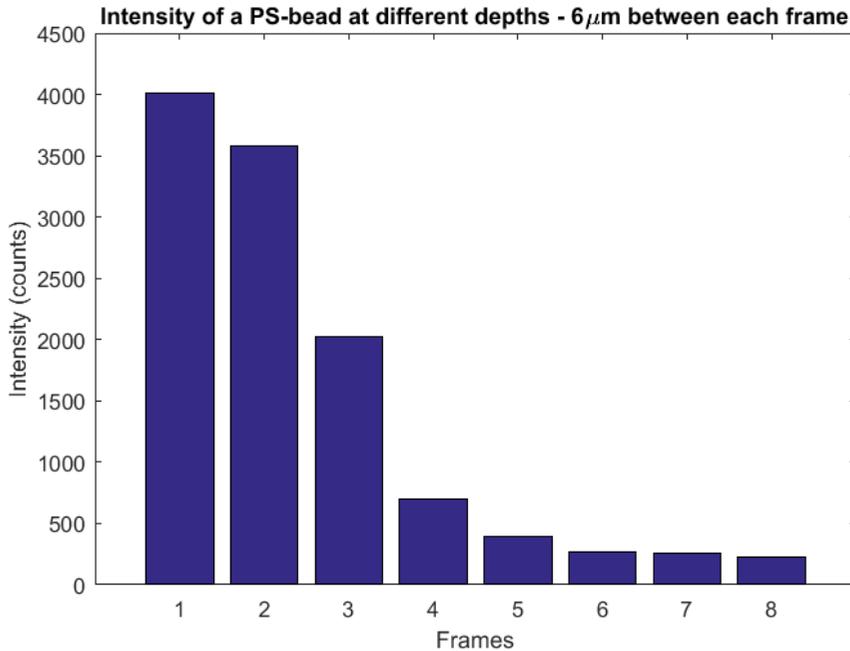
Figure 5.2: ***First stacks of images tested for defocusing particle tracking. The intensity decreased in an expected manner.***

The results attained in ImageJ were solely used for checking and determining that the acquired stacked reference images actually were showcasing particles at different depths. This was proved by the fact that the fluorescence intensity decreased in a predicted fashion, as seen in Fig. (5.2).

The earliest goal of the project was to ensure that all of the software and hardware used was functioning accordingly to the manuals description. If it was not possible to obtain images that were good enough for the forthcoming GDPT analysis, it needed to be considered changing to another experimental set up. The initial testing and results showed that an automated image acquisition was needed in order to save time but also obtain more precise depth changes. Another drawback with this particular setup were the difficulties in saving the large amounts of images. Also, there was not a sufficient way of saving all the images automatically and store them into the same folder.

The chosen size of the PS-beads was 3 μm since in these first experiments, the aim was to understand the GDPT-analysis. By using the 3μm PS-beads instead of 1 μm, we have around 27 times greater volume which simultaneously also results in approximately ten times higher fluorescent intensities. Later on, when studying the acoustic streaming, 1 μm PS-beads were used

since the acoustic streaming, in this size region, strongly dominates over the acoustic radiation force.

It was understood that a large amount of particles in the solution resulted in difficulties during the segmentation of the particles but also hampered the possibility of masking out particular particles for easier calibration instead of using all the available particles. This difficulty in segmentation arose when reaching the deeper Z-positions, as seen in Fig. (5.1), the PS-beads who could freely move in the x- and y-position, ended up above one another. The GDPT-software is a work in progress so occasionally the program also froze or showed strange errors in the Matlab-directory.

It was also observed that for the initially chosen acquisition settings, the particles were brighter than they should be, Fig. (5.1). This overexposure was later on dealt with by lowering the exposure time and increasing the gain until decent images were obtained.

The magnification of the microscope during these initial testings was chosen as a 10x objective in order to increase the depth of focus, which would be preferable over the 20x objective. The 20x objective has its strength in the good resolution and amount of light but using the 10x objective, a larger focus depth is obtained. This basically gives us an improved depth perception at the expense of losing light faster and worsened resolution.

Conclusion

The PS-beads were recognizable about 36 μm at each side away from the focus at the bottom where the main difficulty was caused by the overlapping of the PS-beads and eventually they become too dim to detect, as seen in the small frames furthest to the right in Fig. (5.1). This showcases how important it is to chose an efficient concentration of PS-beads. There is also a problem with these acquired images which needs to be addressed and this was done by using an astigmatic lens. The first experiment gave great insight into the image acquisition process. The minor error sources gave rise to solutions that would develop into useful improvements.

5.2 Defocused particle imaging using an astigmatic lens - complete GDPT-analysis

It was understood that the images from the first setup were fairly decent but a bit too symmetrical and uniform close to the focus depth/plane. The disadvantage lies in that the GDPT-software has difficulties in distinguishing if the PS-beads are above or below the focal plane, when being close to to it. In order to expand this particular range around the focus in the z-direction, a cylindrical lens was put between the microscope and the camera. Obtained astigmatic defocused images using 3 μm PS-beads can be seen in Fig. (5.3). They show how the PS-beads look at the two focal points at the bottom and at the top of the microchannel and when defocusing or moving away from these.
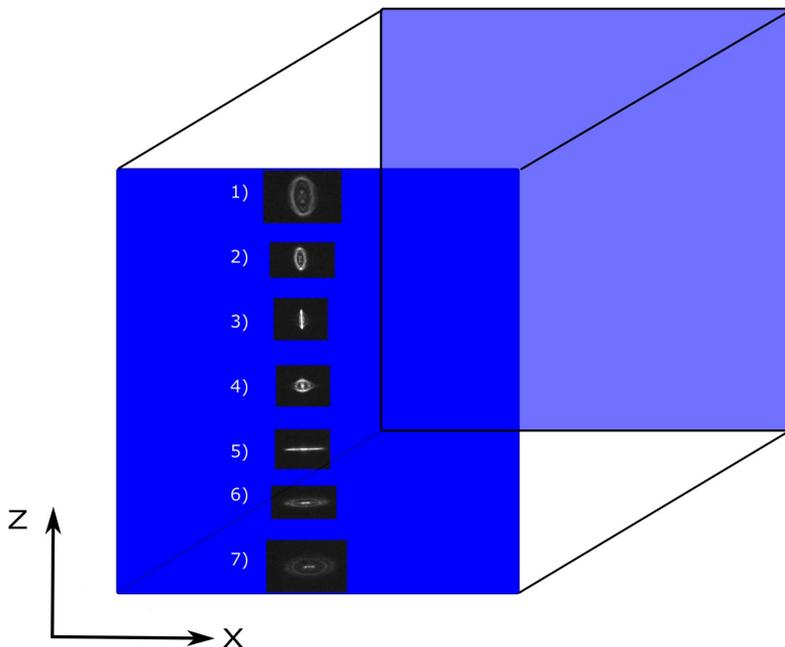
Figure 5.3: **The astigmatic defocusing process shown with real images used for the calibration analysis inside a microchannel. Frame 1 and 7 show when the PS-bead is in focus at the top of the microchannel and at the bottom, respectively. Frame 4 indicates that the PS-bead lies somewhere near the centre of the microchannels height (focus plane). Frame 3) lies slightly above the focus plane and frame 5) slightly under. The remaining frames show the PS-bead being defocused away from the focal points towards the bottom (frame 6) and top (frame 2) of the microchannel. The size of the PS-bead seen in these frames is 3 μm. The microchannel's width is denoted as X and the height as Z.**

The frames from Fig. (5.3) were obtained and saved in the XY-position (width and length of channel), but the depth information (z-position) lies as can be seen, in the horizontal or vertical appearance of the PS-beads. Round shape means that the PS-bead lies near the focus plane, centre of microchannel in this case, whilst horizontal and vertical shapes mean that the PS-bead lies under the focus plane or above it, respectively.

5.2.1   Method

In this case, the program *Micromanager* was used for the image acquisition, automating and thus simplifying the whole process. The exposure time was set to 100 ms and the two specific gains called XM10 Olympus gain and AEAG gain limit were set to 0.8 and 34 respectively, for best contrast in the frames. A calibration was done before analysing the sedimentation rate and trajectories of the 3 μm PS-beads. For the calibration stack, the stepsize in the z-direction (depth) was set to 2 μm/frame. During the image acquisition of the sedimentation, a frame rate of 0.1 frame/s was chosen with a total number of 60 frames taken. Thus, the total image acquisition process took 10 minutes, with an image being taken and saved each 10 seconds. These stacks of images were later on analysed in the GDPT-software, see Appendix C, for a complete particle tracking analysis. No valve was used during this experiment to stop the flow immediately. Instead, the image acquisition was done after letting the flow settle down by itself.

5.2.2   Results and discussion

For the calibration, the PS-beads seen in Fig. (5.4) were used. The threshold was chosen as 12 counts and a minimum area of 300 pixels. The yellow crossed circle ($\otimes$) around the PS-beads indicates that they were valid for the calibration, which means they were tracked in each image, or rather at each depth. The images 92-149 in the calibration stack were showing the interval in which the PS-beads were at all depths of the microchannel. The z-scale was chosen as 2.66 μm, which is the difference between each image (2 μm) multiplied by the refractive index of water (1.33). This was done to account for the fact that light reflected towards a liquid and not solely air.
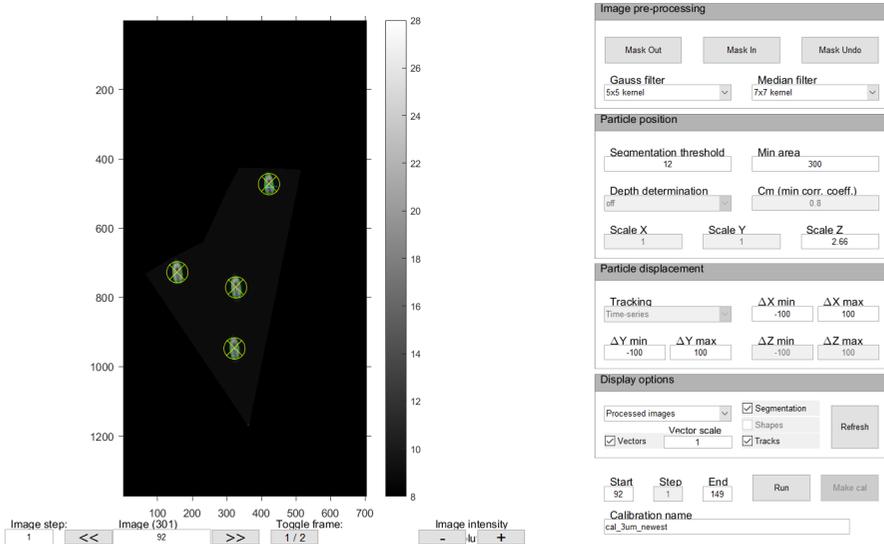
Figure 5.4: **The PS-beads cropped out and used for the calibration, also showing the user interface in the GDPT-software during calibration.**

The results of the calibration can be seen in Fig. (5.5). The measured z-position (•, left axis) lie really close to the actual z-positions (black line) which was calculated as the frame number multiplied by the z-scale = 2.66 μm. This feature, along with the high cross-correlation coefficients C_m (•, right y-axis) indicates that the calibration was good. To put this in perspective, a perfect calibration would follow the black line completely giving $C_m = 1$. In this calibration, the most measured z-positions have correlation coefficients above 0.99, thus proving a really good calibration analysis.
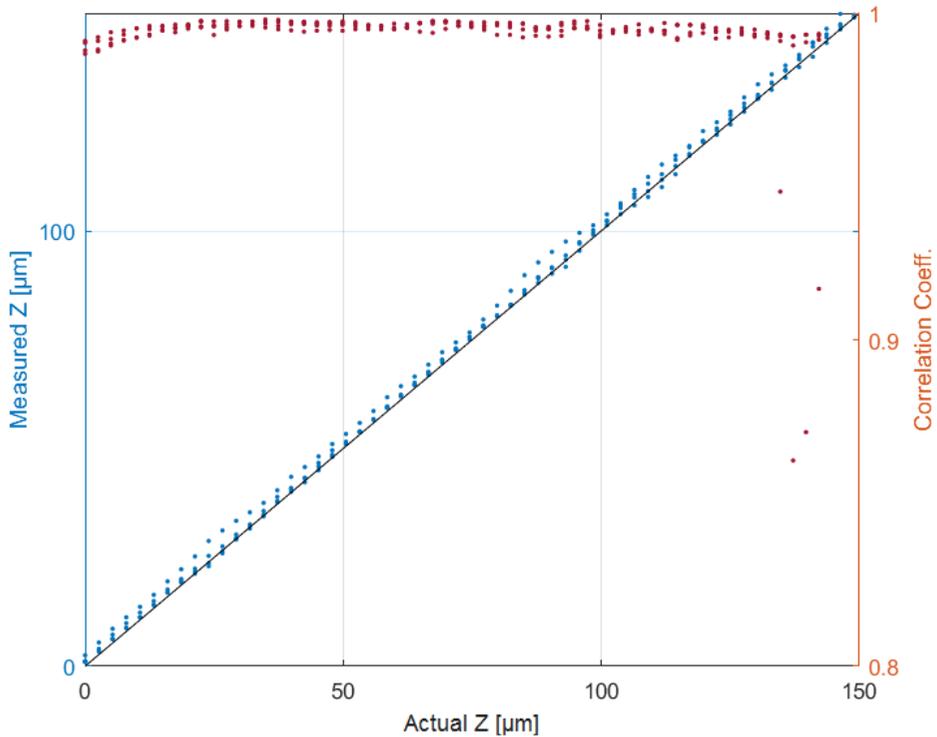
*Figure 5.5: **Calibration evaluation for 3 μm PS-beads.***

The goal was to analyse the sedimentation rate and trajectories of the 3 μm PS-beads. The obtained particle tracking analysis had a predicted flow direction and velocities, as can be seen in Fig. (5.6). The trajectories of the PS-beads in 3D are seen in (a) with the velocities in each dimension x (width), z (depth/height) and y (length). Since the PS-beads were settling towards the bottom, the velocities in the z-direction (DZ) are mostly negative lying between 0-8 μm/s. The higher velocities in the positive y-direction (DY), 0-25 μm/s, are explained by that the flow was let to settle on its own before the image acquisition, during this particular analysis. Ultimately, this means that no valve was used for stopping the flow during aim 1. The main goal was to examine how the GDPT-software worked. The sedimentation of the PS-beads towards the bottom, is easier distinguished in (b), showcasing the starting and ending point of each PS-bead. Thus, every trajectory of one PS-beads journey inside the microchannel can be seen in 3D.
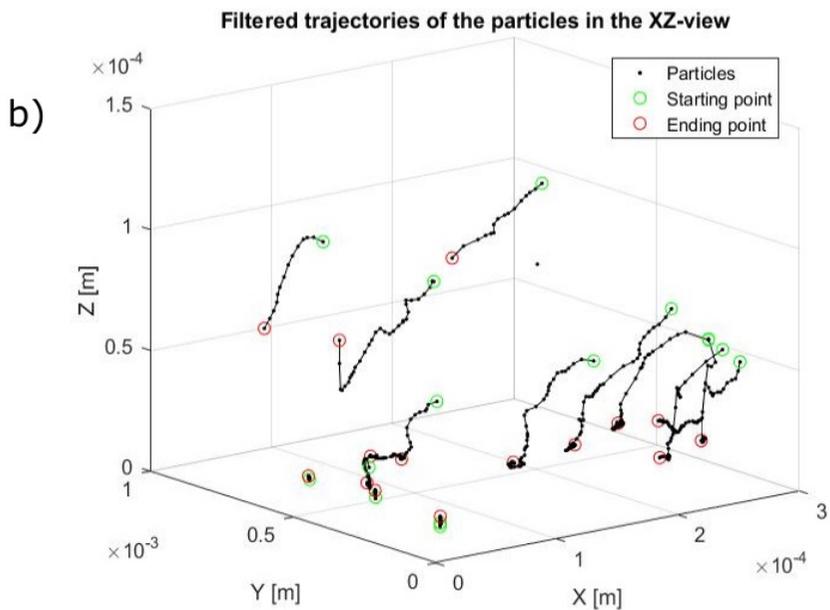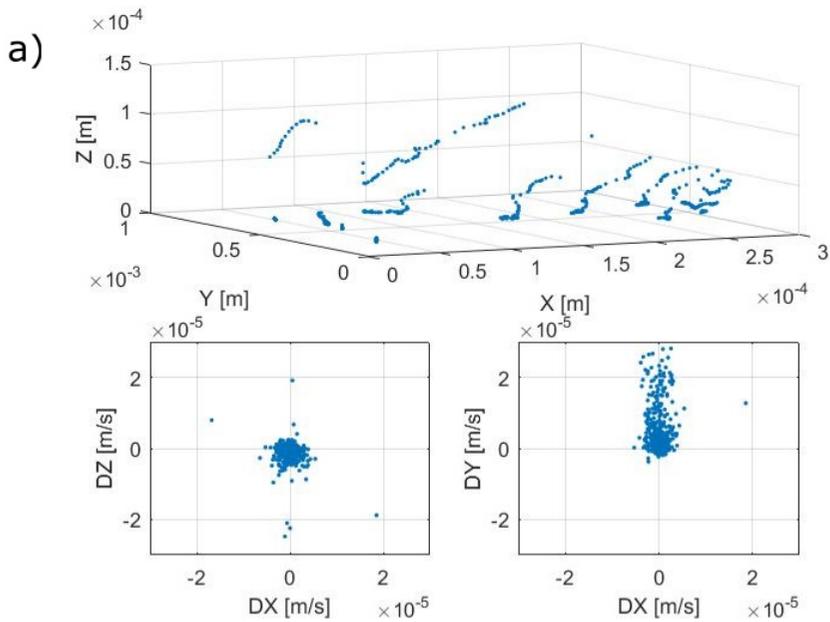
Figure 5.6: **The results of a complete GDPT-analysis using 3 μm PS-beads. (a) showing all the tracks of the PS-beads, their resulting trajectories in 3D and the velocities denoted as DX, DY and DZ. (b) showing the trajectories in 3D with their respective starting point (○) and ending point (○).**

The user interface in the GDPT-software during the analysis, giving the results in Fig. (5.6), can be seen in (5.7). The blue lines (—) represent the trajectories of the different PS-beads. The PS-beads encapsulated by a yellow color (O) are deemed to have a good enough C_m value for particle tracking analysis. Red arrows ($\rightarrow$) correspond to the vector velocity of the beads and the green color (O) surrounding the PS-beads is showing the segmentation.
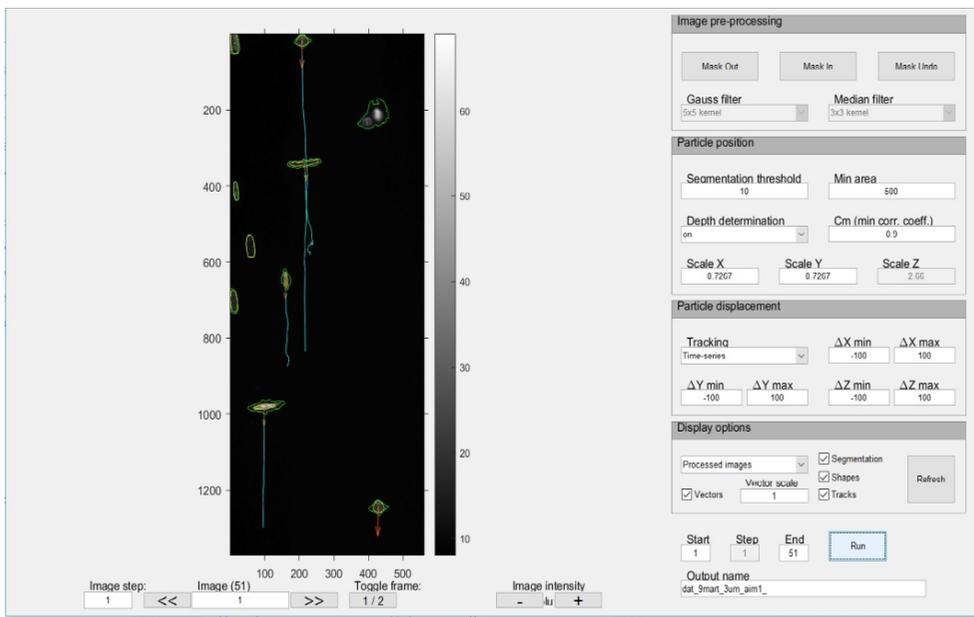
Figure 5.7: **The user interface in the GDPT-software during the particle tracking analysis.**

Still, an error occurred during the image acquisition which created and saved some wrongful images that needed to be erased from the calibration stack. The reason behind this is not known, but a likely cause is some bug in the code of the program *Micromanager*, creating problems during the communication with the camera. Perhaps even the camera itself was causing the error. Thus, the underlying cause of this problem could not be found during the experiments. It was also observed that the particles did not sediment completely towards the bottom (z = 0) but rather at about z = 10 μm, probably because of the astigmatic defocusing properties, changing in only one direction. Another reason may be the chosen images in the calibration analysis, perhaps the frames below z = 10 μm were not deemed as good during the flow analysis. It was also understood that a valve is needed during the forthcoming experiments in order to stop the flow immediately and not being forced to wait for it to settle on its own.

Another interesting thought that arose after studying these results, is that it would be interesting to color code the obtained measured Z (●) to their specific PS-beads in the calibration analysis. Simply put, which PS-bead gives rise to which measured z-position. This would explain which of the PS-beads in the calibration that gives rise to the biggest deviation (●) from the actual z-position (black line in Fig. (5.5)) and could thereby be removed from the calibration. This input was forwarded to Rune Barnkob for improvement in future additions and versions of the GDPT-software during a meeting. It would perhaps also be better if the code of the GDPT-software was open access because as of now, any changes to the source code are prohibited.

Conclusion

The advices and explanations for using an astigmatic lens came from Rune Barnkob and gave great and new insights on the GDPT-method, both concerning its benefits and shortcomings. These results indicated that the GDPT-software can indeed track and plot the trajectories of small beads in 3D, much needed for the following study of acoustic streaming and the acoustic radiation force.

CHAPTER 6

STUDY ACOUSTIC STREAMING FOR HOMOGENEOUS MEDIUM (AIM 2)

Here, the introduction of ultrasound to homogeneous media will be discussed. Homogeneous means that the medium has the same compressibility and density everywhere. With the obtained knowledge of how the GDPT-software works, new experiments were done with 1 μm and 4.8 μm PS-beads, showcasing the trajectories of PS-beads being dominated by acoustic streaming and the acoustic radiation force, respectively after acoustic actuation. Color plots of the magnitudes of the velocities were obtained by using Eq. (2.21) and solved analytically in Matlab, see Appendix B for code. In order to see if the results were equivalent to that expected from theory, the acoustic energy density E_{ac} was measured by using it as a fitting parameter in Eq. (2.20) and Eq. (2.22). The resulting trajectories and velocities were solved analytically in Matlab. In these following sections, only results regarding the velocities obtained by the GDPT-analysis will be shown and discussed. A list of the parameters and their values used in these experiments can be seen in Table (6.1), obtained from [43].

Table 6.1: **List of parameters and their values used during the experiments with acoustic actuation.**

Parameter	Definition	Value
w	width of the channel	375 μm
h	height of the channel	150 μm
k_x	wave number	8378 m^{-1}
ρ_w	density of water	997 kgm^{-3}
c_w	speed of sound in water	1497 ms^{-1}
a	radius of the PS-beads	1 μm and 4.8 μm
η	viscosity	0.89 mPas
Φ	acoustic contrast factor	0.17
δ	width of the viscous boundary layer	0.38 μm
$s^T_{\lambda \approx 5h}$	thermoviscous + geometry correction factor	0.194
χ(a) - 1μm	wall correction coefficient at Z = 75μm	1.006
χ(a) - 4.8μm	wall correction coefficient at Z = 75μm	1.033
χ(a) - 4.8μm	wall correction coefficient at Z = 115μm	1.042

6.1 Introduction of acoustic field for homogeneous medium - 1 μm PS-beads

6.1.1 Method

Micromanager was used for the image acquisition. The exposure was set to 100 ms with the XM10 Olympus gain and AEAG gain limit set to 0.8 and 34 respectively. The step-size in the depth direction during the calibration was used as 2 μm/frame. The particle solution was injected into the microchannel as explained in section 4.1.4. Before each acoustic actuation, the flow was stopped using a valve, see chapter 4.1.4 for details. The frequency range of the generated acoustic standing wave was chosen as a linear sweep between 1.9-2.1 MHz with an amplitude of 6 V_{pp}. One image acquisition took 1 minute, using a frame rate 2 frames/s with a total of 120 frames acquired. This procedure was done three times, resulting in three different stacks of images in order to obtain more PS-beads at all depths and to see if the analysis was reproducible. The obtained image stacks were then analysed using the GDPT-software, see Appendix C. Lastly, the obtained trajectories and velocities of the GDPT-analysis were compared to and solved analytically with the theory of acoustophoretic motion, Eq. (2.20) and Eq. (2.22), see Appendix B.

6.1.2 Results and discussion

As can be seen in Fig. (6.1), the appearance of the PS-beads flow and trajectories correspond to that of acoustic streaming near a boundary layer (Rayleigh streaming), also known as the outer streaming. Four distinct vortices can be distinguished in the transverse cross section of the microchannel with the corresponding velocities in all three dimensions, X (width), Y (length) and Z (depth). The reason why there are not that many PS-beads near the sidewalls (X < 50μm and X > 350μm) is because the GDPT-software did not deem these trajectories as good enough (low values of *Cm* and also hard to segment out). The true depth of the microchannel is 150 μm but some PS-beads can be seen above Z = 150 μm. The reason behind this is the small deviation obtained during the calibration. It has been understood that during the image acquisition, it is important to lie in a focus depth where the PS-beads can be distinguished in all depths, much like the ones seen in Fig. (5.3) in section 5.2. It was thought that the optimal position for the focus was to place it at the centre of the microchannel's height. Since we has astigmatic defocusing properties, this was shifted and thus a small deviation in the results arose. It was fixed by simply subtracting it from the results in the Matlab code.

Note the movements in (c), where the detailed flow direction of the PS-beads is shown. The PS-beads can be seen being drawn towards the centre of the microchannel, where the $\lambda/2$ standing wave has its minimum (node) and then being deflected either towards the bottom or top of the microchannel. The impact of the previously described Schlichting inner streaming can thus be seen by this GDPT-analysis. As explained before, the outer streaming rolls and the bulk flow are a direct result of the counter-rotating inner streaming rolls inside of the viscous boundary layer of thickness $\sim 0.38\mu$m.
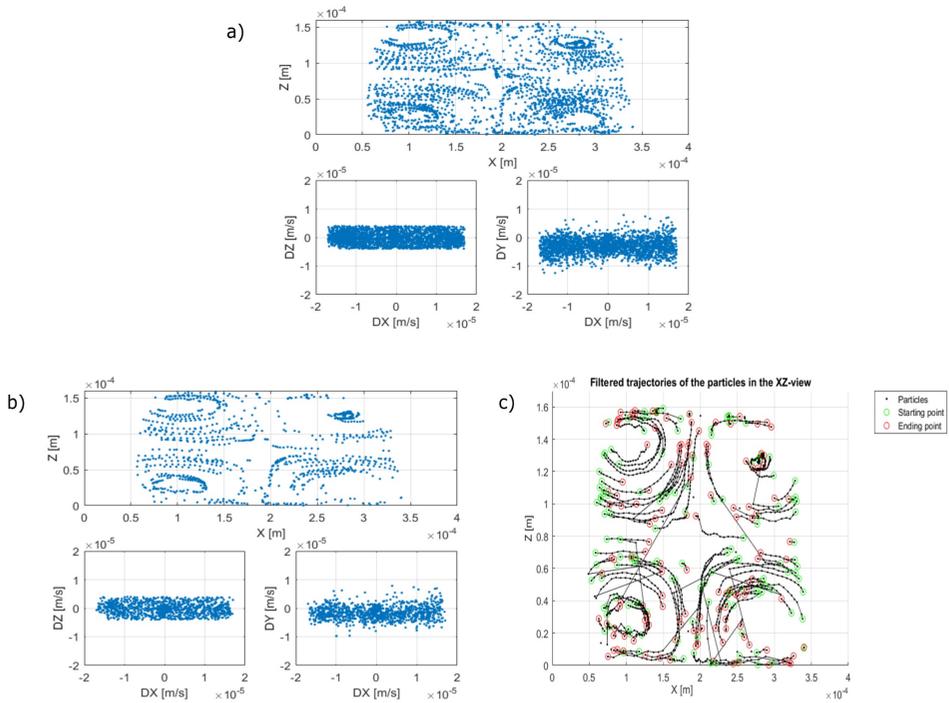
Figure 6.1: **The results of a complete GDPT-analysis using 1μm PS-beads after acoustic actuation. (a) showing all the tracks of the PS-beads from three repeated experiments, their resulting trajectories in the vertical cross section (Z-depth, X-width) and the velocities denoted as DX, DY and DZ. (b) showing one of the three sets used in the analysis and (c) showing the trajectories of this particular set with their respective starting point (○) and ending point (○).**
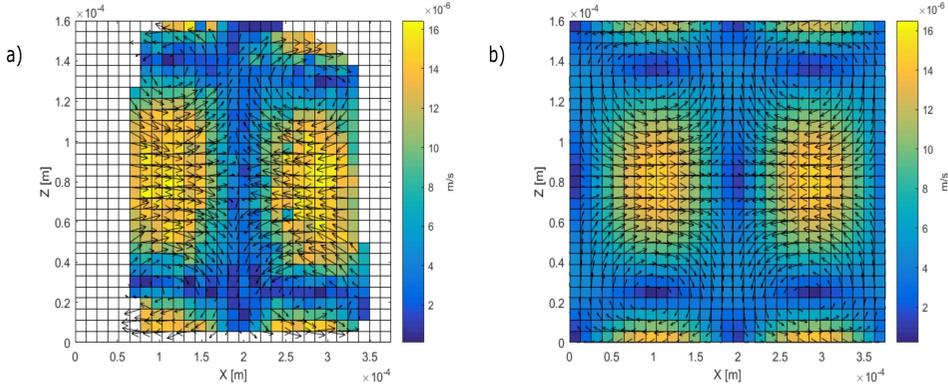
*Figure 6.2: **Color plots showing the magnitude of the 1 μm PS-bead velocities using Rayleigh's equation for acoustic streaming combined with the impact of the ARF, Eq. (2.21). The orientation in each plot is the vertical channel cross section (Z = depth, X = width) where the arrows correspond to the velocity vectors in the X- and Z-direction. (a) experimental data. (b) complete theoretical model. The colors range from dark blue, 0 μm/s to yellow $u_{mag}(max)$ = 16.4 μm/s.***

The velocities and trajectories in Fig. (6.1a) were then color plotted and the resulting magnitude velocities can be seen in Fig. (6.2). (a) showcases the experimental data whilst (b) shows the corresponding magnitude color plot of the theoretical model of Rayleigh acoustic streaming combined with the impact of acoustic radiation force, Eq. (2.21). The empty areas in (a) correspond to no experimental data obtained in those regions. Comparing (a) and (b), the positions of the streaming rolls seem to coincide. The biggest inaccuracy comes from the bottom and top och the microchannel where a small depth deviation can be seen, thus proving the importance of the calibration. Also, when looking at Fig. (6.1c), some PS-beads seem to travel long distances from one channel side to the other. The reason behind this is most likely that the GDPT-analysis confuses two different PS-beads that have the same normalized cross-correlation with one another. Such outliers can easily be filtered out by setting constraints, for instance, regarding maximal distance that they can travel.

Conclusion

By using the GDPT-software, the depth information of the 1 μm PS-bead trajectories was extracted and thereby successfully displaying the dominating nature of acoustic streaming after actuation of an acoustic field.

6.2 Introduction of acoustic field for homogeneous medium - 4.8 μm PS-beads

The next step was to examine if larger PS-beads showcased expected trajectories dominated by the acoustic radiation force.

6.2.1 Method

Micromanager was once again used for the image acquisition, with the same gain properties as before but with a lower exposure of 5 ms since these larger 4.8 μm PS-beads have a volume of about 100 times the size of the smaller 1 μm, thus exhibiting much higher fluorescent intensities. The step-size in the depth direction during the calibration was set to 2 μm/frame once again, with the same generated acoustic standing using a linear sweep between the frequencies 1.9 - 2.1 MHz. The frame rate was 4 frames/s with a total of 25 frames acquired, thus the whole image acquisition process took around six seconds. Nine different stacks of images were acquired, for the same purposes as with the 1 μm PS-beads, obtaining more trajectories in each depth and examining the reproductivity of the experiments. The image stacks were then analysed using the GDPT-software, see Appendix C. The resulting trajectories and velocities were compared and solved analytically with the theory of acoustophoretic motion, Eq. (2.20) and Eq. (2.22), see Appendix B.

6.2.2 Results and discussion

In Fig. (6.3) we can clearly see that the PS-beads are dominated by the acoustic radiation force, focusing towards the middle of the microchannel where the node of the $\lambda/2$ standing wave lies. In total, nine sets of experiments were acquired. One of these sets is shown in (b) and (c) for easier characterization of the trajectories. As can be seen in this particular set, not many PS-beads were found at the channels side walls, which also was one of the reasons for acquiring more data sets/experiments.
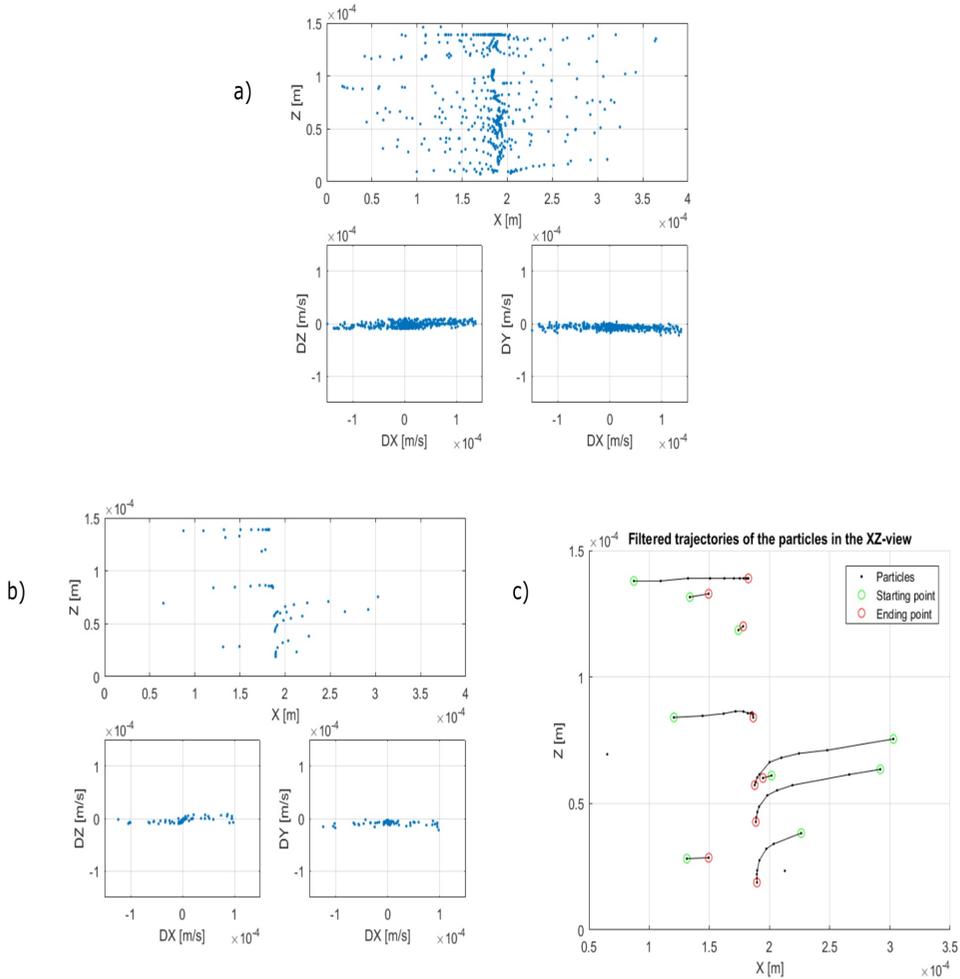
*Figure 6.3: **The results of a complete GDPT-analysis using 4.8 μm PS-beads after acoustic actuation. (a) showing all the tracks of the PS-beads from nine repeated experiments, their resulting trajectories in the vertical cross section (Z-depth, X-width) and the velocities denoted as DX, DY and DZ. (b) showing one of the sets used in the analysis and (c) showing the trajectories of this particular set with their respective starting point (○) and ending point (○).***

All of the nine sets used, seen in Fig. (6.3a), were then color plotted in regards to the magnitude of the velocities and the results can be seen in Fig. (6.4a). When comparing the experimental results in (a) with the theoretical model in (b), a few conclusions can be extracted. First of all, the side walls and the corners at the bottom of the microchannel lacked data points. This also appeared in the experiments with the 1 μm PS-beads, seen in Fig. (6.2a). The astigmatic defocusing properties are what caused these deviations. With

the benefit of hindsight, the solution behind this problem would be to exactly find which position inside the microchannels depth that showcased the whole range of images used in the calibration. Another logical way with dealing with this lack of data points would be to increase the concentration of the PS-bead solutions, but it was also understood that higher concentrations lead to more PS-beads overlapping each other at different depths and thereby making segmentation much more difficult, ultimately making the GDPT-software disregard these PS-beads. Thus, a trade-off between a decent amount of PS-beads and a good segmentation in the GDPT-software is needed for optimal results.
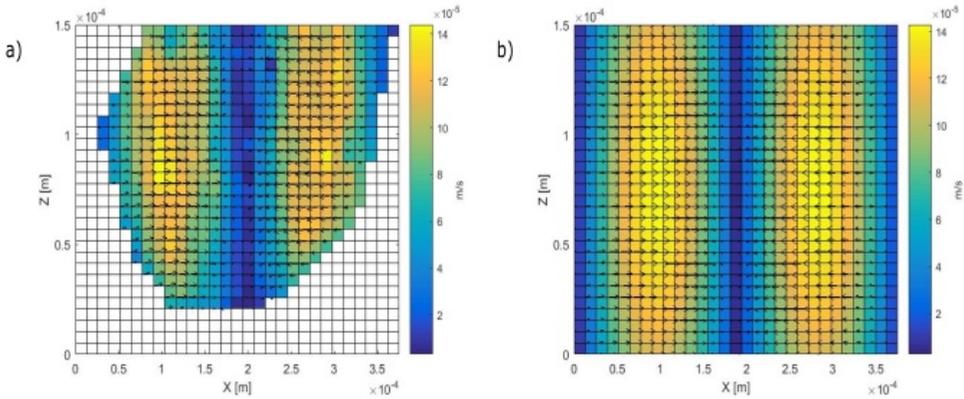

Figure 6.4: **Color plots showing the magnitude of the 4.8 μm PS-beads velocities using Rayleigh's equation for acoustic streaming combined with the impact of the ARF, Eq. (2.21). The orientation in each plot is the vertical channel cross section (Z = depth, X = width) where the arrows correspond to the velocity vectors in the X- and Z-direction. (a) experimental data. b) complete theoretical model. The colors range from dark blue (0 μm/s) to yellow ($u_{mag}(max)$ = 144 μm/s).**

Another apparent fact when comparing figures (a) and (b) is that the velocities in the experimental data seem to be more "smeared out" than the theoretical model which shows an increasing pattern with a distinctive max velocities at around $X = 90 - 100 \, \mu$m and $275 - 300 \, \mu$m. This is because the equation, Eq. (2.21), for the velocities total particle velocity, which is a sinus function, has its maximum (sin = 1) at $X = W/4$, where W stands for the microchannel's width. The same tendencies can not fully be recognized in the experimental results. In (a), the interpolation method used by the method *griddata* in Matlab probably could not evenly distribute the velocities as in the theoretical model seen in (b), as a result of using nine different experimental sets and superimposing these values.

Conclusion

The resulting trajectories of the 4.8 μm PS-beads were shown to be dominated by the ARF after acoustic actuation. Some minor drawbacks arose with the lack of experimental data at some points inside of the microchannel and the magnitudes of the velocities being more smeared out than in the theoretical model. The next step was to see if the obtained velocities of the 1 μm and 4.8 μm PS-beads were correct, by comparing them to theoretical models.

6.3   Measuring the acoustic energy density E_{ac}

In order to verify and prove the validity of the resulting trajectories of the 1 μm and 4.8 μm PS-beads, the acoustic energy density was fitted to the experimental data by using the theoretical models for acoustic streaming and the acoustic radiation force velocity. Matlab code can be seen in Appendix B.

6.3.1   Method

The experimental data was fitted to the parameter E_{ac} using the Matlab program *cftools* which is an open curve fitting tool. The fit type was chosen as the total particle velocity or rather the acoustophoretic motion of a PS-bead as seen in Eq. (2.20) which is labeled as the classical representation. Thereafter, the extended version, Eq. (2.22), was also introduced for fitting of the experimental data. The values of the parameters used in the following calculations can be seen in Table (6.1).

6.3.2   Results and discussion

The whole process when fitting the parameter E_{ac} to the experimental data of the 4.8 μm PS-beads can be seen in Fig. (6.5). The resulting fit for the experimental data obtained in (b) along the width direction at Z = 112.5 μm is shown in (d), in this particular case giving a value of the acoustic energy density of 19.00 J/m^3.
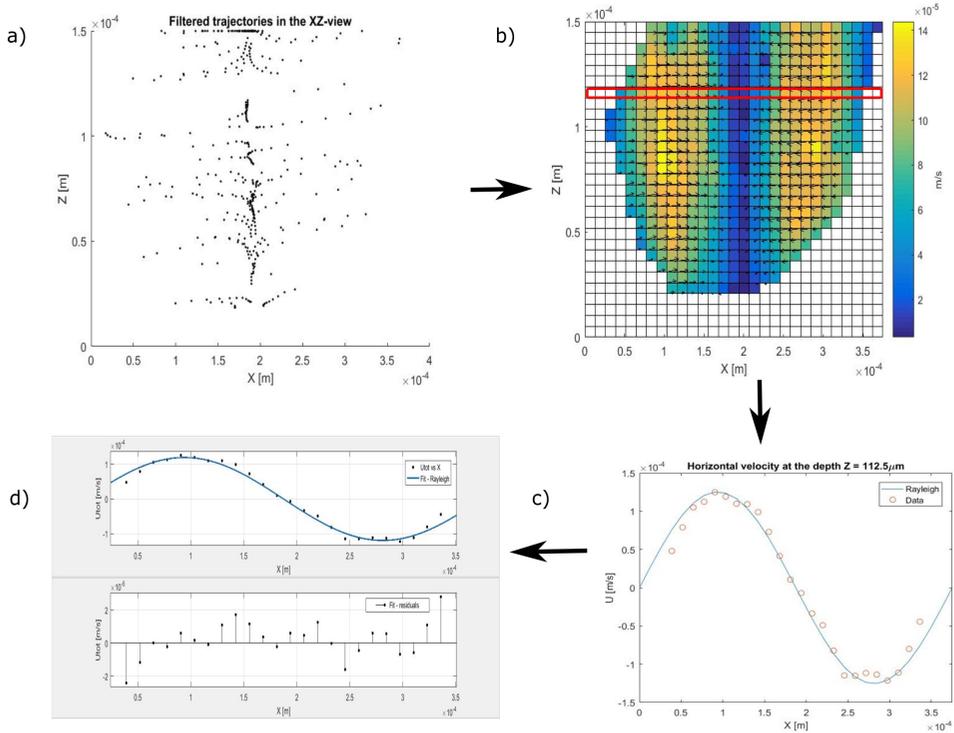
Figure 6.5: **Fitting experimental data to parameter E_{ac} using 4.8 µm PS-beads. a) all of the trajectories used from nine repeated experiments. (b) interpolation method using Delaunay triangulation color coding the velocity vectors ranging from dark blue (0 µm/s) to yellow ($u_{mag}(max)$ = 144 µm/s). This was done with the help of a Matlab code called quiverc [24]. The data at depth Z = 112.5 µm was used for fitting in this case ($\square$). (c) The velocities at Z = 112.5 µm as a function of X-position showing the experimental data ($\circ$) and the theoretical model (—) with Rayleigh's acoustic streaming combined with the ARF-dominated velocity $u_r ad$, Eq. (2.20). (d) The final fit (—) compared to the experimental data ($\bullet$), also showing the error/deviation of the experimental data from the fit in the form of residuals (—$\bullet$).**

The same analysis of the velocities were also done for the 1 μm PS-beads, where one of the tested sets, along the depth direction at X = 100 μm, can be seen in Fig. (6.6). The fitting resulted in an acoustic energy density of 20.80 J/m^3.
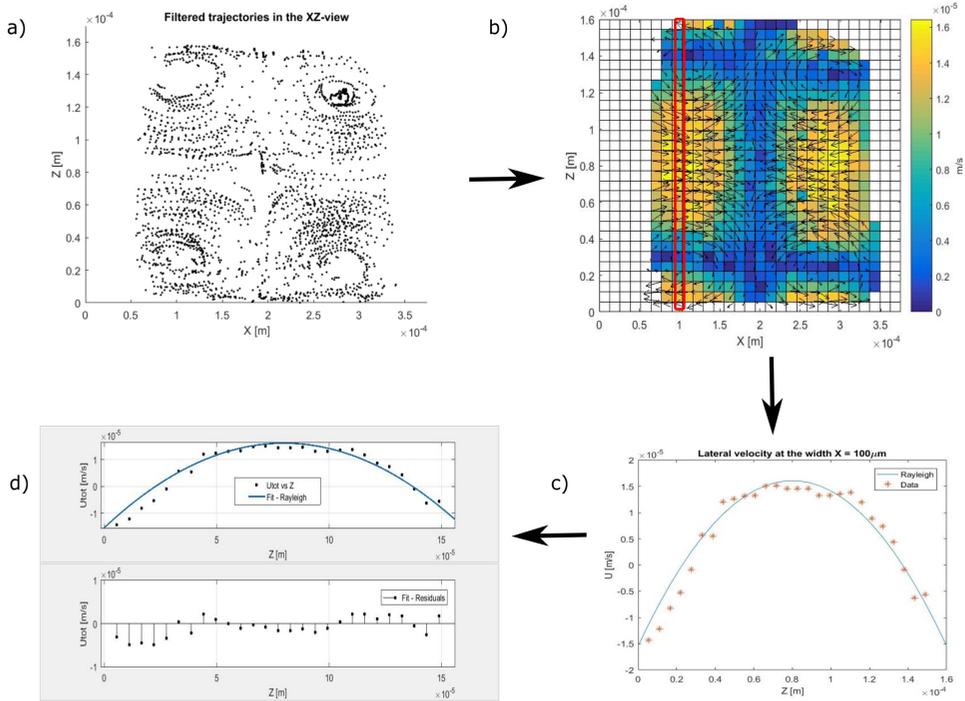

*Figure 6.6: **Fitting experimental data to parameter E_{ac} using 1 μm PS-beads. (a) All of the trajectories used from three repeated experiments. (b) Interpolation method using Delaunay triangulation color coding the velocity vectors ranging from dark blue (0 μm/s) to yellow ($u_{mag}(max)$ = 16.4 μm/s). This was done with the help of a Matlab code called quiverc [24]. The data at width X = 100 μm was used for fitting in this case ($\square$). (c) The velocities at X = 100 μm as a function of Z-position showing the experimental data ($*$) and the theoretical model (—) with Rayleigh's acoustic streaming combined with the ARF-adominated velocity u_{rad}, Eq. (2.20). (d) The final fit (—) compared to the experimental data ($\bullet$), also showing the error/deviation of the experimental data from the fit in the form of residuals (—$\bullet$).***

Tables (6.2 - 6.3) show all of the sets used at different depth- and width-positions indicating similar values of the acoustic density energy with high values of R^2 ranging from 94% - 99%. The statistical model with the R^2 values describes how much of the observations/data that is described by the fitted curve. Mathematically it is seen as one minus the error sum of squares (SS_{res}) divided by the total sum of squares (SS_{tot}), Eq. (6.1) [31].

$$R^2 = 1 - \frac{SS_{res}}{SS_{tot}} \tag{6.1}$$

where

$$SS_{res} = \sum_{i=1}^{n}(y_i - f_i)^2 \tag{6.2}$$

and

$$SS_{tot} = \sum_{i=1}^{n}(y_i - \bar{y})^2 \tag{6.3}$$

y - experimental data/observations
f - data from fitted model
ȳ - mean of experimental data/observations

The least predictable data set was obtained for the 1μm PS-beads at X = 100 and 275 μm where the vertical positions inside the microchannel were examined, Fig. (6.6), whereas the horizontal position at the centre of the microchannel gave high values of $R^2 > 98$ %. Overall, the results clearly show that the obtained velocities in both experiments were valid, since it was expected to obtain the same or adjacent values of E_{ac}, seeing that the acoustic density energy is directly related to the voltage applied for acoustic actuation. The same frequency and voltage, (1.9-2.1 MHz, linear sweep with an actuation voltage of 6 V_{pp}), was used in both of the experiments using 1 μm- and 4.8 μm PS-beads.

Table 6.2: **Results after fitting data of the PS-beads velocities with the help of Rayleigh's classical equation for acoustic streaming combined with velocities caused by the acoustic radiation force, Eq. (2.20).**

Size	X-position	Z-position	E_{ac}(J/m^3)	Goodness of fit
1μm	0-375μm	75μm	20.11	R^2 : 0.9844
1μm	100μm	0-160μm	20.80	R^2 : 0.9378
1μm	275μm	0-160μm	21.21	R^2 : 0.9538
4.8μm	0-375μm	75μm	18.13	R^2 : 0.9778
4.8μm	0-375μm	112.5μm	19.00	R^2 : 0.9858

In Table (6.3), the extended equation of the acoustophoretic motion of PS-beads was used. This equation, Eq. (2.22), only considers horizontal velocities, thereby meaning that the component $u_{str}(z)$ as described in Eq. (2.20) is being neglected. The reason behind the introduction of this improved version was to see if the results would drastically change compared to Table (6.2), since for instance the parameters used in these experiments assumed a temperature at 25 C°. Although, the true temperature of the system was not measured in the beginning, the results in both Table (6.2) and (6.3) were showing great similarities, thus verifying and validating the obtained velocities as correct. Both equations thus indicated that the constant value of E_{ac} during these experiments was around 20 J/m^3.

Table 6.3: **Results after fitting data of the PS-beads velocities with the help of an extended version of Rayleigh's equation with added thermoviscous and wall drag - correction, Eq (2.22).**

Size	X-position	Z-position	E_{ac}(J/m^3)	Goodness of fit
1μm	0-375μm	75μm	19.55	R^2 : 0.9844
4.8μm	0-375μm	75μm	18.60	R^2 : 0.9772
4.8μm	0-375μm	115μm	18.52	R^2 : 0.9858

Another fact that was examined to see if the obtained velocities were correct, was the relation between the magnitudes of the acoustic streaming and acoustic radiation force velocities denoted as u_{str} and u_{rad}, as seen in Eq. (2.21). The theoretical relation between these two velocities can be written as [18]:

$$\frac{u_{str}}{u_{rad}} = \frac{9\eta w}{4\pi\phi a^2 \rho_w c_w}$$

(6.4)

Using the values from Table (6.1), the theoretical value of the ratio when using 4.8 μm PS-beads was obtaining as 0.16, thus meaning that u_{str} should be around 16% of u_{rad}. The same ratio was obtained as 20% when analysing the experimental data, thereby exhibiting a small increase compared to the theory. Still, the results clearly show that the bigger beads are dominated by the ARF.

The same ratio was then obtained for the smaller 1 μm PS-beads where the domination of acoustic streaming was expected. The results showed that this indeed was the case. The theoretical ratio was obtained as 3.77, which means that u_{str} should be around 3.77 times larger than u_{rad}. The experimental data showcased a ratio of 3.26, somewhat smaller than the theoretical ratio but nevertheless showing the dominating nature of acoustic streaming over the acoustic radiation force when dealing with the smaller PS-beads. The critical radius of the PS-beads, meaning where $u_{rad} = u_{str}$, lies somewhere near 1 μm for water [18]. The PS-beads used in these experiments (a = 0.5 μm) were thus much smaller than the critical radius 1 μm.

Lastly, a more straight forward examination of the velocities was done by looking at the image stacks of the 4.8 μm experiments to see how far the PS-beads traveled in the X-direction. Since we know the frame rate used during the analysis, an estimation of the PS-beads velocity could be obtained. This simple estimation was in the same region as the velocities from the GDPT-analysis. For instance, the chosen PS-beads in Fig. (6.7) had a mean horizontal velocity of 128 μm/s and 104 μm/s respectively.

a) $t_1 = 0$ b) $t_2 = 0.25$ s
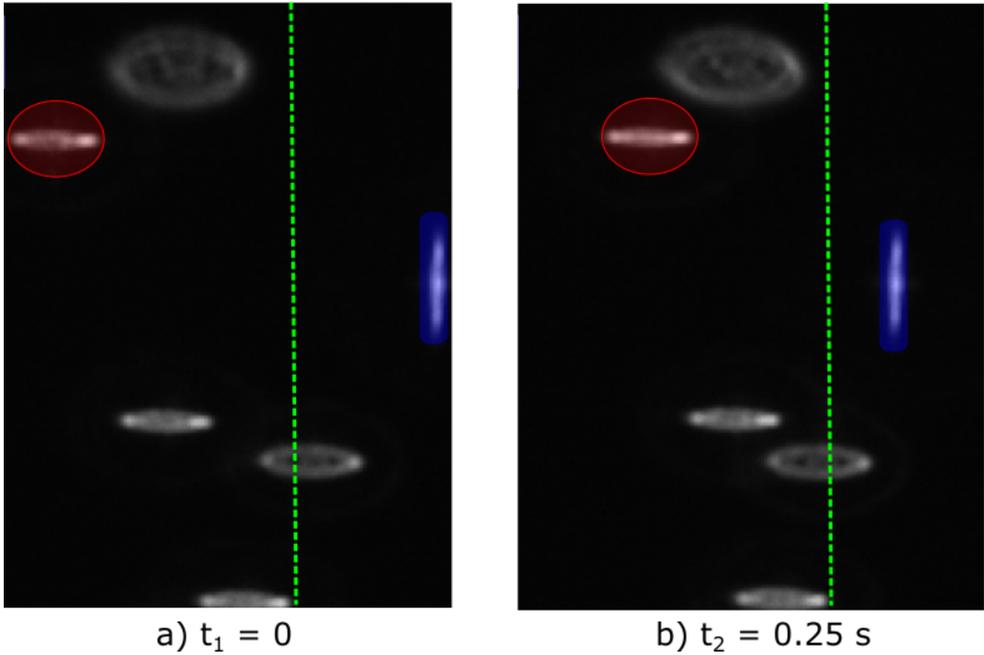
Figure 6.7: **Obtaining the horizontal velocities for the 4.8 μm PS-beads by using the image stacks. The xy-orientation is seen in the images, x being the width of the microchannel and y being its length. The images are zoomed in, in order to distinguish the travel distances easier, where the centre of the microchannels width, which the PS-beads travel towards is denoted by (- -). In this chosen frame period, the first PS-bead (○) traveled 32 μm in 0.25 seconds, giving an average horizontal velocity of 128 μm/s. The second PS-bead (□) instead traveled 26 μm in 0.25 seconds, giving an average horizontal velocity of 104 μm/s.**

Conclusion

By fitting the parameter E_{ac} to the experimental data and obtaining similar values in the different experiments, it was shown that the obtained velocities were correct and in the right order of magnitude, thus indicating that the GDPT-software was successful in measuring the velocities of the PS-beads. With this new insight about the GDPT-analysis, the next aim was to examine if the acoustic streaming would be suppressed when using the IAF-method.

CHAPTER 7

ACOUSTIC STREAMING IN FLUIDS OF INHOMOGENEOUS DENSITY AND COMPRESSIBILITY (AIM 3)

As already explained, in small microfluidic systems, we have resonance conditions that can create acoustic streaming after acoustic actuation. When dealing with small particles and beads (a $< 1\ \mu$m), this acoustic streaming impairs the quality of separation and focusing methods based on applied acoustic radiation forces. Thus, it would be of great significance to suppress the impact of acoustic streaming. The introduction of a density gradient using an inhomogeneous medium in IAF [19], is thought to be a method where the suppression of acoustic streaming indeed is possible, as described more in detail by Karlsen *et al.* [32]. These theoretical explanations need experimental proof and the following chapter will show and discuss with the help of experimental data, what impact the IAF-method has on the phenomenon acoustic streaming.

7.1 Studying the acoustic streaming in fluids with inhomogeneous density and compressibility

7.1.1 Method

Almost the same method as in chapter 6 was performed but now with some important changes. To begin with, iodixanol (20%) was laminated next to the PS-bead solution, in order to create a density gradient, where the syringe setup can be seen in Fig. (4.8) and (4.2). The denser and more viscous iodixanol-solution was diluted using reverse pipetting. *Micromanager* was used for the image acquisition, with the same gain properties as before. The exposure was set to 100 ms since 1 μm PS-beads were used. The step-size in the depth direction during the calibration was set to 2 μm/frame, with a generated acoustic standing using a linear sweep between the frequencies 1.9 - 2.1 MHz with an applied actuation voltage as V_{pp} = 10 V, being larger than in the experiments of chapter 6, in order to see how well even larger velocities could be analysed and detected. The frame rate was set to 10 frames/s with a total of 500 frames acquired, thus the whole image acquisition process took around 50 seconds for each experimental data set. Two different aspects, see Fig. (7.1), were examined. Firstly, acquiring images after stopping the flow and immediately actuate the acoustic field (IAF-method), with 4 different sets of data being acquired. The latter aspect was to acquire images after waiting for 5 minutes, for diffusion to mix the liquids, after stopping the flow and then actuating the acoustic field. In this case, 3 different sets of data were obtained. The image stacks were lastly analysed in the GDPT-software and Matlab.
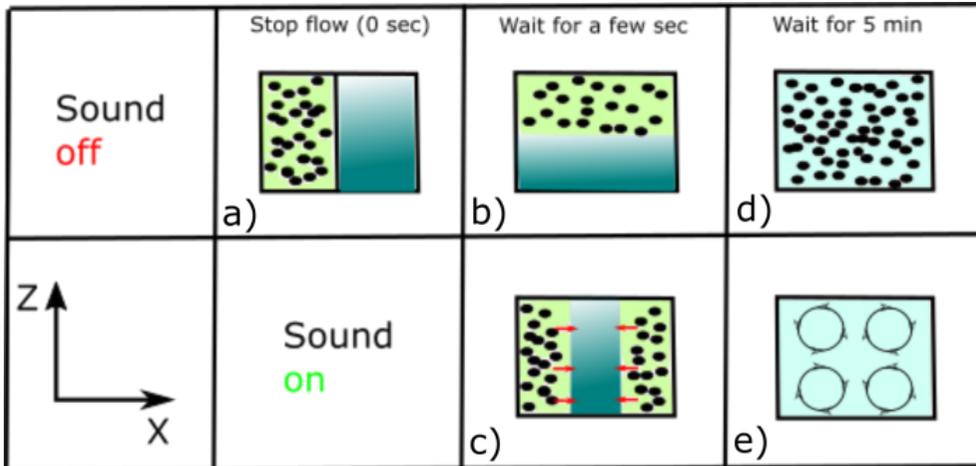
*Figure 7.1: **Schematic for the experiment during aim 3. (a) The PS-bead so-
lution (•) and the density gradient medium iodixanol (dark blue color) are
laminated next to each other before entering the microchannel. (b) A few sec-
onds after the flow is stopped, the heavier density gradient medium will move
towards the bottom of the microchannel due to impact of gravity. (c) If the
acoustic field is actuated after a few seconds, the iodixanol solution will move
to the centre of the microchannel and the PS-beads will be pushed to the side-
walls. From there, they will be affected by the ARF and move laterally towards
their specific iso-acoustic point, where the difference in acoustic impedance of
the PS-beads equals the acoustic impedance of the medium ($Z_{PS} = Z_{medium}$).
After around 30 seconds, small circular motions of the PS-beads will again
be observed, due to the impact of diffusion. (d) A homogeneous medium was
obtained by stopping the flow and waiting for 5 minutes, letting the solutions
mix. (e) Now, with the homogenenous properties of the medium, fully devel-
oped acoustic streaming will once again be present.***

7.1.2   Results and discussion

The iodixanol-solution, which acts as the density gradient medium, was lam-
inated together with the PS-bead solution before entering the microchannel
with the help of a bi-furcation as previously described and seen in Fig. (4.2),
in chapter 4. After the acoustic actuation, it was discovered that the PS-beads
moved to the sidewalls, see Fig. (7.2b). It only differs 300 ms between the
two images (a) and (b), indicating that the relocation of the medium was an
fast event.
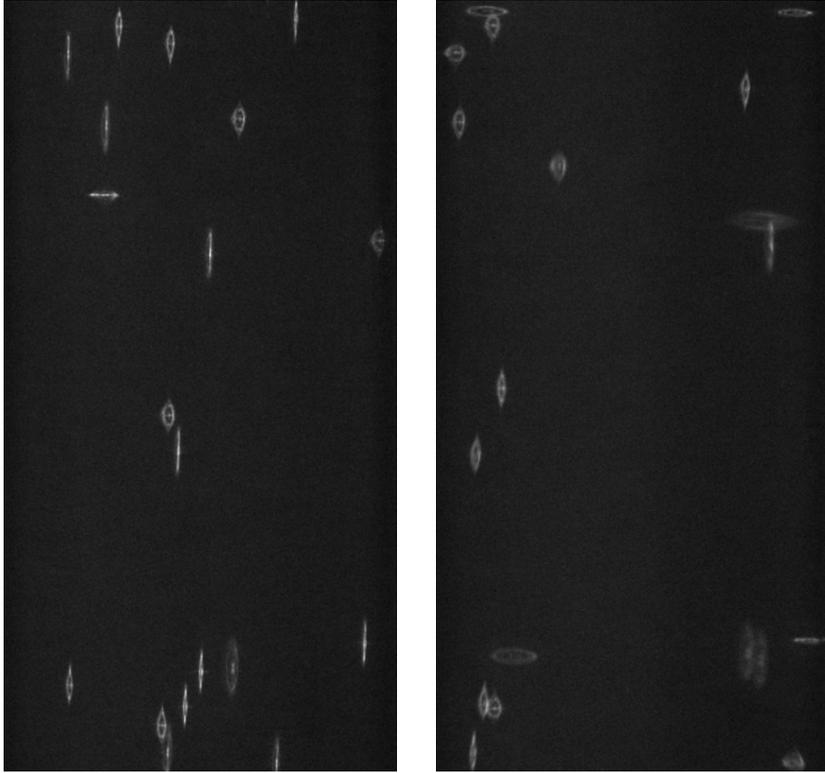
*(a) **Orientation of the 1 μm PS-beads before the acoustic actuation, x-y view.***

*(b) **Orientation of the 1 μm PS-beads after the acoustic actuation, x-y view.***

*Figure 7.2: **The effect of liquid relocation after acoustic actuation. It differs 300 ms between the two images. (a) is before acoustic actuation and (b) is afterwards.***

Since the iodixanol-solution has a greater density than the surrounding solution containing PS-beads, initially before the acoustic actuation ($E_{ac} = 0$ J/m^3), it will be more affected by the gravity and lie closer to the bottom of the microchannel. When turning on the ultrasound, the iodixanol-solution would relocate to the centre of the microchannel, pushing the solution with PS-beads to the side channels, Fig. (7.2b). The interface between the two liquids, caused by gravity and density differences, was thus stabilized after the acoustic actuation. The initial work behind this relocation phenomena was treated in (Deshmukh *et al.*, 2014) [33], where a fluid containing NaCl was successfully relocated and stabilized at the centre of a microchannel. The physical representation of this stabilising appearance of the density gradient can be seen in Fig. (7.3), which also gives a physical explanation to why the

acoustic streaming can not arise, since the density gradient acts somewhat as a blocking medium. This kind of stabilization of the density gradient can also be found in [32], where they used different values of E_{ac} and the higher the value, the better stabilization of the denser gradient was obtained at the centre of the microchannel, much like the experimental results seen in Fig. (7.3b).
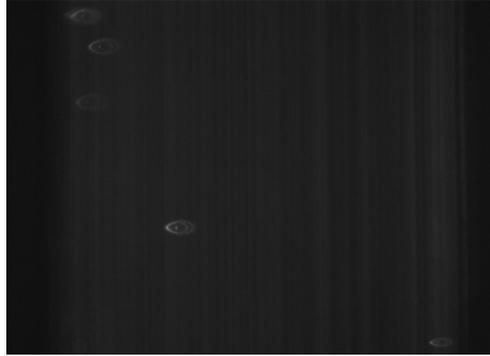
(a) Flow of solution before acoustic actuation E_{ac} = 0 J/m^3, x-y view.
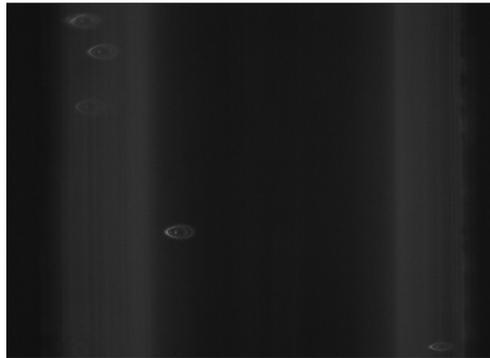
(b) Flow of solution after acoustic actuation $E_{ac} \approx 54$ J/m^3, x-y view.

*Figure 7.3: **Flow of the 1μm PS-beads in inhomogeneous medium before and after acoustic actuation. The inhomogeneous properties are clearly seen in (b), where the actuated pressure standing wave forces the denser iodixanol-solution to stabilize towards the centre of the microchannel, where the node lies, whilst the PS-bead solution ends up at the side walls.***
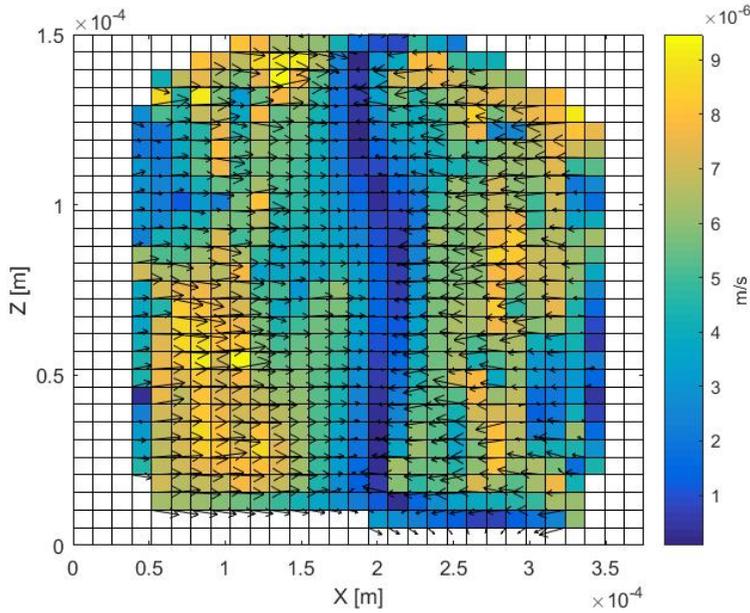
(a) **Color plot coded by velocity magnitude with the overlaying velocity vectors of the PS-beads as arrows in the XZ-view. The velocities range from dark blue, 0 µm/s to yellow color $u_{mag}(max)$ = 10 µm/s).**
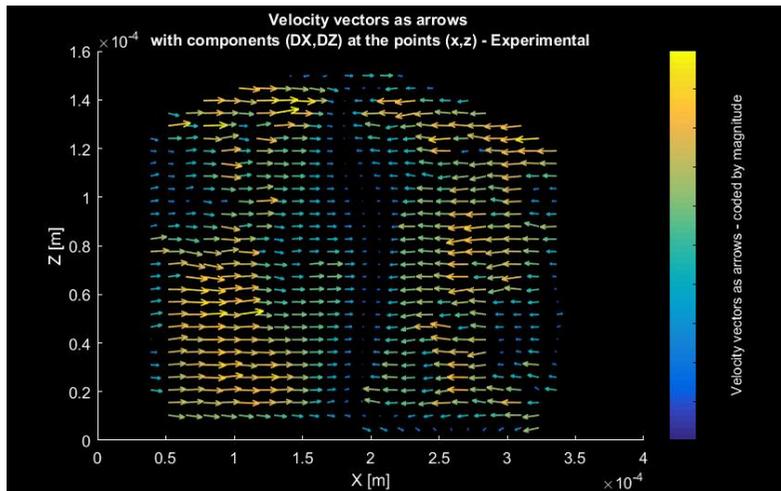
(b) **Color plot coded by velocity magnitude with the overlaying velocity vectors of the PS-beads as arrows in the XZ-view using the Matlab code quiverc [24]. This version makes it easier to distinguish the velocity vectors.**

Figure 7.4: **Test with the density gradient medium iodixanol. The results for the 1 µm PS-beads, acquiring images 10 seconds after acoustic actuation. Little time for diffusion to have any effect within this time frame.**

The results in Fig. (7.4) were obtained with the help of an image stack, immediately acquired after the acoustic field was turned on, see Fig. (7.2b). Thus, during the first ten seconds of this experiment, the 1 μm PS-beads were mainly affected by the ARF before the acoustic streaming could be seen later on near the microchannel's bottom and top after the two fluids were mixed together by diffusion, thereby changing from an inhomogeneous- to more of a homogeneous medium.

Eq. (2.21) was used for calculating the different magnitude velocities u_{rad}, $u_{str}(x)$ and $u_{str}(z)$, see Appendix B for detailed Matlab code. The color plot in Fig. (7.4a) was obtained in this manner, with the velocity vectors being the result of a quiver-plot. Simultaneously, Fig. (7.4b) shows color coded velocity vectors, making it easier to distinguish the horizontal movement towards the centre of the microchannel.

These results showcase that the acoustic streaming has been suppressed considerably when using the IAF-method with inhomogeneous medium since the classical streaming rolls are not seen after the acoustic actuation, as compared to the results with homogeneous medium, Fig (6.2). The PS-bead trajectories rather showcase a more horizontal/lateral nature, as if they are now more dominated by the ARF. To examine exactly how much the acoustic streaming has been suppressed by using the IAF-method, these results needed to be compared to when the two liquids were allowed to mix by diffusion, using the same GDPT-analysis as previously.
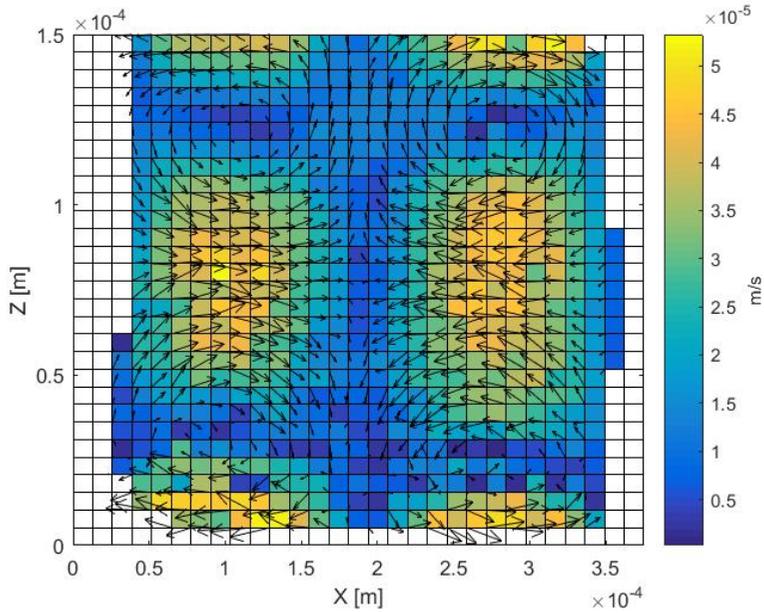
(a) **Color plot coded by velocity magnitude with the overlaying velocity vectors of the PS-beads as arrows in the XZ-view. The velocities range from dark blue, 0 µm/s to yellow color $u_{mag}(max)$ = 53 µm/s.**
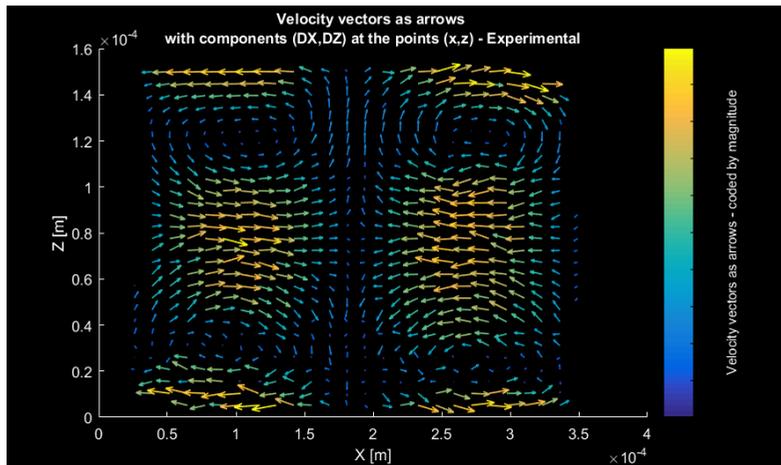

(b) **Color plot coded by velocity magnitude with the overlaying velocity vectors of the PS-beads as arrows in the XZ-view using the Matlab code quiverc [24]. This version makes it easier to distinguish the velocity vectors.**

Figure 7.5: **Test with density gradient medium. The results for the 1 µm PS-beads, acoustic actuation was done after waiting five minutes, letting the liquids mix by diffusion.**

The results after waiting for five minutes before acoustic actuation can be seen in Fig. (7.5) and the similarities with Fig. (6.2) in chapter 6 are obvious. It indicates that the theoretical assumption of letting the liquids mix and thereby obtaining a homogeneous medium once again is valid, since we clearly can see the characteristic acoustic streaming rolls again. As mentioned earlier, the main goal was to examine the size of the suppression of acoustic streaming while using the IAF-method.

Just by comparing the max velocities from the two experiments, Fig. (7.6), we can see that the total max velocity of the PS-beads when using the IAF-method ($u_{mag}(max) = 10\ \mu$m/s) in (a) is decreased by a factor of around 5 compared to when the two liquids are mixed in (b) and the inhomogeneous characteristics of the medium are lost ($u_{mag}(max) = 53\ \mu$m/s).
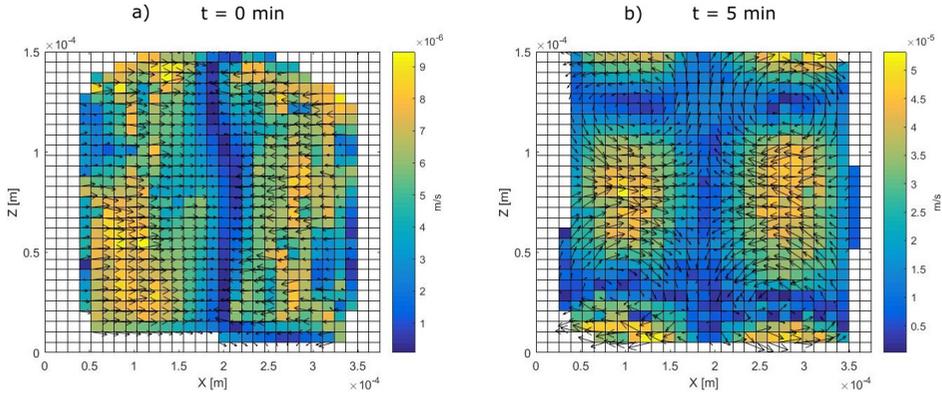
Figure 7.6: **Color plots of the experiment using a density gradient medium for 1 μm PS-beads with (a) acoustic actuation done immediately after stopping the flow with velocities ranging from 0 μm/s to $u_{mag}(max)$ = 10 μm/s and (b) diffusion taking place for five minutes, mixing the liquids, before acoustic actuation, with velocities ranging from 0 μm/s to $u_{mag}(max)$ = 53 μm/s.**

Initially, the lateral velocities at the depth of were obtained as illustrated in Fig. (7.7).
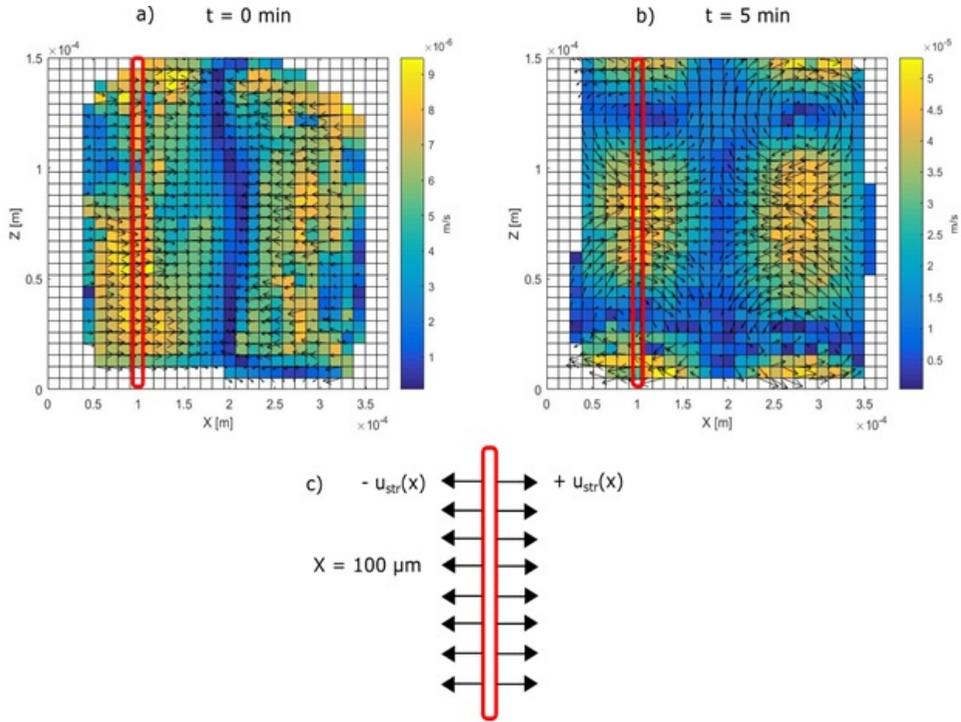
*Figure 7.7: **The process when obtaining the lateral velocities for both the homogeneous and inhomogeneous results. (a) Color plot for inhomogeneous medium. (b) Color plot for homogeneous medium. (c) The x-component of the acoustic streaming, $u_{str}(x)$, was calculated at X = 100 μm for the two cases.***

It is a palpable and essential difference when comparing the results in Fig. (7.6). This difference is a direct demonstration of the IAF-method. Stopping the flow and waiting for five minutes before acoustic actuation as seen in (b) corresponds to the experiments with homogeneous media whilst the PS-beads in (a) are mainly being affected by the ARF, showcasing the size-independency of the method since the acoustic streaming is suppressed.
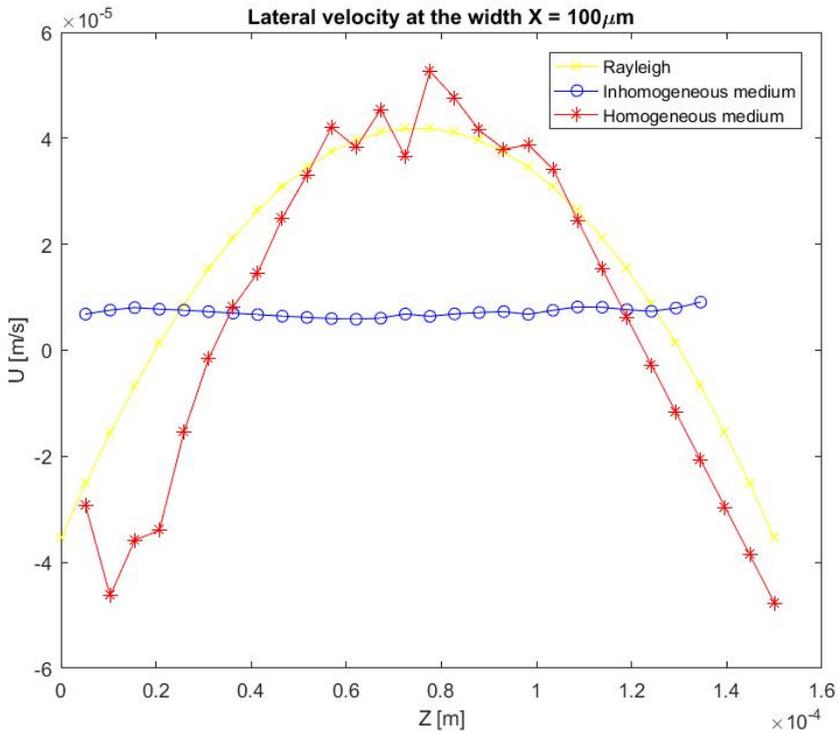
*Figure 7.8: **The acoustic streaming velocities as a function of depth (z) at the width x = 100 μm when using inhomogeneous and homogeneous medium. The theoretical Rayleigh model for the lateral movement of the PS-beads is used as** $u_{str}(x) + u_{rad}$**, Eq. (2.20).***

The suppression of acoustic streaming can easily be distinguished in Fig. (7.8) where both the experiments using homogeneous and inhomogeneous are shown. The Rayleigh model corresponded to an acoustic energy density of 54 J/m^3 which is plausible since in this experiment, the applied voltage from the function generator was increased from the previous case 6 V_{pp} to 10 V_{pp}. Comparing the results for the homogeneous medium with the theoretical model, a small shift can be observed at Z = 0 – 50 μm and Z = 100 – 150μm. Thus, in these regions, the experimental velocites for the acoustic streaming are systematically lower than in the theoretical model.

The most important discovery from Fig. (7.8) is that the velocities in the in-homogeneous medium are in principle independent on depth (z), and instead dominated by the acoustic radiation force.

It is hard to find a proper way to value an actual size of the suppression since acoustic streaming is dependent on both x- and z-direction, but in this thesis a ratio was calculated between the mean absolute velocities (z-direction) of the acoustic streaming, see Fig. (7.9). This related more to the acoustic streaming since the inhomogeneous case should only be affected by the ARF, thereby only having a lateral movement and an vertical velocity that is approximately zero.
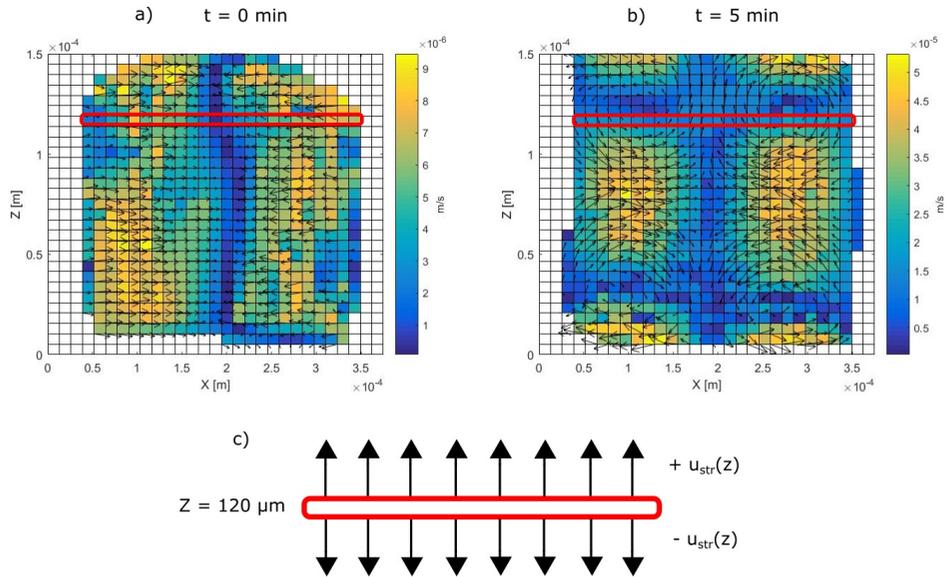
*Figure 7.9: **The process when calculating a ratio between the acoustic streaming in a homogeneous and an inhomogeneous medium. (a) Color plot for inhomogeneous medium. (b) Color plot for homogeneous medium. (c) The z-component of the acoustic streaming, $u_{str}(z)$, was calculated at $Z = 120$ μm for the two cases. For homogenenous medium, the theoretical max velocity of $u_{str}(z)$ lies around this region.***

The results are ilustrated in Fig. (7.10) and the distinctive difference between inhomogeneous and homogeneous medium can be distinguished. Whilst the $u_{str}(z)$ for homogeneous medium is similar to the theoretical model of Rayleigh's acoustic streaming Eq. (2.19), the vertical acoustic streaming for inhomogenenous medium seems to be more or less around 0, indicating that the velocity is mainly affected in the lateral direction, meaning not dependent on z.
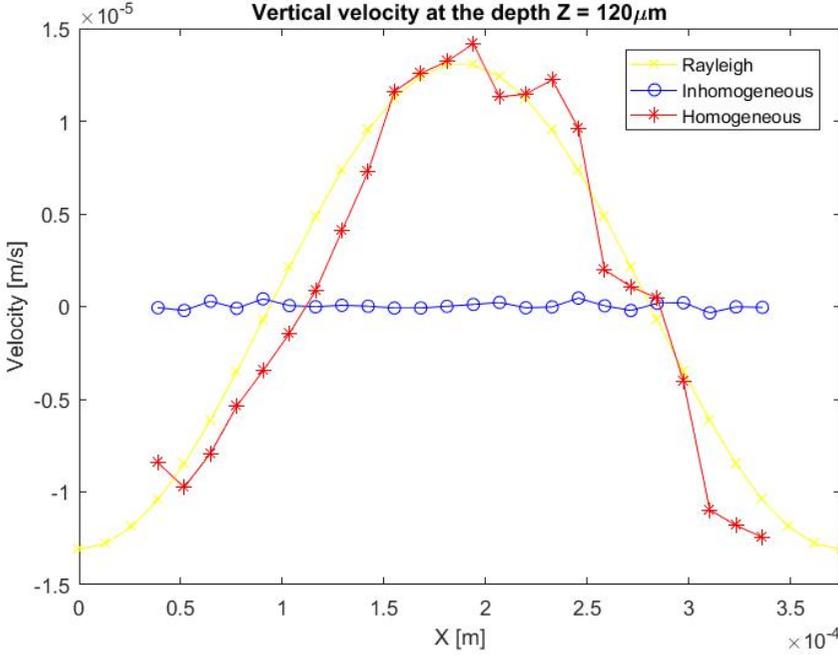
Figure 7.10: **Vertical velocity $u_{str}(z)$ for three cases, inhomogeneous medium, homogeneous medium and theoretical model.**

The ratio was calculated as:

$$\frac{\left|u_{str}(z)^{t=5min}\right|}{\left|u_{str}(z)^{t=0min}\right|} \approx 57 \tag{7.1}$$

Eq. (7.1) explains that the acoustic streaming is suppressed approximately a 57-fold when using the IAF-method, compared to the usual case with a homogeneous medium. These results follow the description in [19] (Supplementary Note 2), where the explanation of this suppression was presented in the fact that the time-averaged acoustic density energy E_{ac} has different values in different areas of the microchannel whereas when using a homogeneous medium, E_{ac} has a constant value as seen in chapter 6. They also explained this suppression of acoustic streaming mathematically by calculating the ratio between the acoustic forces related to the acoustic streaming rolls and the inhomogeneous medium, respectively. The results showed that the acoustic force density (f_{ac}) generated by the inhomogeneous medium (not constant E_{ac}) is about 10 000 stronger than the acoustic force density (f_{str}) related to the acoustic streaming rolls. The suppression of acoustic streaming obtained in this study is probably even higher than the factor of 57 since it is hard to

measure a value that is close to zero because of noise levels. The statistical ratio in Eq. (7.1) is thus only a simplistic view of the overall suppression, the most important information lies in that the appearance of the velocities obtained in homogeneous and inhomogeneous medium are so significantly different.

Conclusion

With the help of the GDPT-analysis, it was discovered that the acoustic streaming is decreased by an average factor of 57, when implementing the IAF-method using a density gradient (iodixanol, 20%), compared with homogeneous medium.

CHAPTER 8

ETHICAL REFLECTION

New and innovative methods that lead to breakthrough insights in their field require a deep understanding of the moral and ethical questions behind them. One of the goals is to minimize every possible source of error, resulting in improved safety protocols, before finally coming out to the public use via clinical studies. This is particularly true regarding novel methods with a background in physics and human biology. For instance, in the field of microfluidics, a well used application is DNA-sequencing of human genomes. This gives us a future possibility of parents modifying the DNA of their babies, creating the perfect gene pool for coming generations. Should it be possible, for the greater good, to design new human beings by removing the unwanted gene sequences and how do we find these "universally bad" genes? Should doctors and patients be allowed to see such results? These negative aspects need to be measured and compared with the grater good that DNA-sequencing can give us, namely knowing the risks for a disease long before symptoms arrive and a better knowledge of how the human body works. As can be seen, ethical reflection is much needed.

This thesis is examining a fundamentally physical principle, regarding IAF and acoustophoresis, currently having no obvious risks. With that being said, the main question lies in what the knowledge from IAF can contribute to future methods. The goal with IAF is to use it as a fast diagnostic tool in the healthcare. A possible design is that it would be used as a biomarker since it has shown to detect cell specific acoustic properties, being able to separate different white blood cells from each other, having roughly the same size but completely different biochemical tasks in our immune system [19]. In the

case of a larger screening and clinical study, e.g. for a specific aggressive bacteria using IAF, the participants/patients need to know every detail of the procedure, both pros and cons, before "signing on" the study. The data obtained from such a large study needs to be taking care of, only used for the cause of deducing how efficient and fast the IAF-method is for handling and identification of bacterias and other small pathological particles.

As of now, the method of IAF is designed to be used outside of a human body, as a potential diagnostic tool. In the future however, the IAF-method may very well be modified and instead incorporated into more invasive treatment methods giving faster and hopefully extra secure answers in real time, during e.g. an operation. Sensitive questions arise if this new method would happen to give incorrect diagnoses for patients and it would be considered how much of this misdiagnosis is due to IAF and how much is due to the remaining components of this method. Thus, a deeper understanding is needed between the interaction between the IAF and other treatments, if incorporated in the future.

CHAPTER 9

OVERALL CONCLUSION

Iso-acoustic focusing has proven to be a new method potentially allowing acoustic focusing of bacteria and viruses in the sub-micrometre range. It grants a way to overcome the difficulties caused by acoustic streaming in acoustophoresis. The results showed that the velocities in the inhomogeneous medium using 1 μm PS-beads are in principle independent on z. Hopefully, this thesis presents some of the knowledge that is crucial and needed for future investigations of IAF.

For future use of the GDPT-software in these kind of studies, more focus should lie on perfecting the calibration process. This was not possible during this particular project since, as of now, it is unfortunately not allowed to be handed out and used as an open access code, meaning that no underlying changes could be made with the source code. A particularly good insight was obtained during the calibration process where it would be helpful if it was possible to color code the resulting measured z-positions, thus knowing which actual PS-bead that gives the biggest deviation to the theoretical z-position and thereby ignore and not use it. Also, a more optimal place for the focus when acquiring the images should be chosen. When placing the focus in the centre of the microchannel, as in this thesis, all of the trajectories will be slightly deviated because of the astigmatic defocusing properties. As a suggestion, one could try to put the focus slightly under or above the centre of the channel and make a full GDPT-analysis, being of a "trial-and-error" approach until decent trajectories are obtained with no deviation present.

Considering the position in the microchannel where all of the images were acquired, ~ 19 mm from the inlet, maybe it was not the most optimal concerning the strength and evenness of the acoustic field. If the PZT is not working properly or not put in the right position next to the microchannel, this could potentially lead to areas inside the the microchannel where the acoustic field is uneven.

Problems arose while using the camera and saving the real-time images, where the reason behind this was not found. Some of the acquired frames seemed to flicker around and turn completely black and gray before being saved. This was tried to be dealt with by changing to different frame rates, until a normal image stack was acquired for further GDPT-analysis.

The used values for the parameters in the different equations regarding the acoustophoretic motion of PS-beads had a few assumptions, such as that the temperature of the system was 25 °C. The temperature sensor coupled to the microchannel was not used during the experiments so the true temperature was only assumed to be around room temperature. In future aspects, the correct temperature would be needed to be known in order to get the most suitable values of the different parameters. The values of the parameters are also slightly changed when switching from the homogeneous to the inhomogeneous medium, making it difficult to fit the results to an analytical equation. This is for instance the case when considering the important parameter E_{ac}, which goes from being a constant to having different values at different positions in the microchannel, thanks to the inhomogeneous properties of the density gradient medium.

Future work and improvements regarding this project should also consider using even larger data sets with more images using different frame rates, increasing the statistical credibility. The parameter E_{ac} could also be fitted in a different way, e.g. by using data sets of different applied voltages, ranging from 0-10 V_{pp}. Higher concentrations of the iodixanol-solution should be studied in order to see the effects. The GDPT-software also needs to be understood better, what exactly happens during the analysis. Perhaps, it would also be interesting to do more experiments using particles with a negative contrast factor or increasing the harmonics, thus having more nodes and antinodes.

All in all, this thesis has shown how the IAF started out nothing more than a curious thought and then develop into an improvement of regular acoustophoresis, suppressing the impact of acoustic streaming. This truly shows that curiosity is indeed a scientist's greatest weapon.

BIBLIOGRAPHY

[1] Whitesides, G, **2006**, *"The origins and the future of microfluidics"*, Nature, 442, 7101, pp. 368-373, Inspec, EBSCOhost, viewed 21 November 2016.

[2] Stone, H, Stroock, A & Ajdari, A, **2004**, *"ENGINEERING FLOWS IN SMALL DEVICES: microfluidics Toward a Lab-on-a-Chip"*, Annual Review Of Fluid Mechanics, 36, 1, pp. 381-411, Academic Search Complete, EBSCOhost, viewed 21 November 2016.

[3] Folch, A, **2013** *"Introduction to bioMEMS"*, *Boca Raton : CRC Press, cop. 2013*

[4] Ashraf, M, Tayyaba, S & Afzulpurkar, N, **2011**, *"Micro Electromechanical Systems (MEMS) Based Microfluidic Devices for Biomedical Applications"*, Journal Of Molecular Science (International Edition), 12, 6, pp. 3648-3704, Inspec, EBSCOhost, viewed 21 November 2016.

[5] Bashir, R, **2004**, *"BioMEMS: State-of-the-art in detection, opportunities and prospects"*, Advanced Drug Delivery Reviews, 56, 11, p. 1565-1586, Scopus®, EBSCOhost, viewed 21 November 2016.

[6] Manz, A, Graber, N & Widmer, H, **1990**, *"Miniaturized total chemical analysis systems: a novel concept for chemical sensing"*, Sensors And Actuators B (Chemical), B1, 1, pp. 244-248, Inspec, EBSCOhost, viewed 21 November 2016.

[7] Tian, W & Finehout, E n.d., **2009**, *"Microfluidics For Biological Applications"*, n.p.: Dordrecht, Netherlands : Springer, ePublications, EBSCOhost, viewed 21 November 2016.

[8] Tetala, K & Vijayalakshmi, M, **2016**, *"Review: A review on recent developments for biomolecule separation at analytical scale using microfluidic devices"*, Analytica Chimica Acta, 906, pp. 7-21, ScienceDirect, EBSCOhost, viewed 21 November 2016.

[9] Jung, W, Han, J, Choi, J & Ahn, C, **2015**, *"Review Article: Point-of-care testing (POCT) diagnostic systems using microfluidic lab-on-a-chip technologies"*, Microelectronic Engineering, 132, Micro and Nanofabrication Breakthroughs for Electronics, MEMS and Life Sciences, pp. 46-57, ScienceDirect, EBSCOhost, viewed 21 November 2016.

[10] Jivani, R, Lakhtaria, G, Patadiya, D, Patel, L, Jivani, N & Jhala, B, **2016**, *"Review: Biomedical microelectromechanical systems (BioMEMS): Revolution in drug delivery and analytical techniques"*, Saudi Pharmaceutical Journal, 24, pp. 1-20, ScienceDirect, EBSCOhost, viewed 21 November 2016.

[11] Guo, M, Rotem, A, Heyman, J & Weitz, D, **2012**, *"Droplet microfluidics for high-throughput biological assays"*, Lab On A Chip, 12, 12, pp. 2146-2155, MEDLINE, EBSCOhost, viewed 21 November 2016.

[12] Mohammadi, M, Madadi, H & Casals-Terré, J, **2015**, *"Microfluidic point-of-care blood panel based on a novel technique: Reversible electroosmotic flow"*, Biomicrofluidics, 9, 5, pp. 1-11, Academic Search Complete, EBSCOhost, viewed 21 November 2016.

[13] Grenvall, C, **2014**, *"Acoustic Forces In Cytometry And Biomedical Applications : Multidimensional Acoustophoresis"*, [Electronic Resource], n.p.: Lund : Department of Biomedical Engineering, Faculty of Engineering, Lund University, 2014, Library catalogue (Lovisa), EBSCOhost, viewed 21 November 2016.

[14] Petersson, F, Nilsson, A, Laurell, T, Holm, C & Jönsson, H, **2004**, *"Separation of lipids from blood utilizing ultrasonic standing waves in microfluidic channels"*, Analyst, 129, 10, p. 938-943, Scopus®, EBSCOhost, viewed 21 November 2016.

[15] Bruus, H, **2012**, *"Acoustofluidics 7: The acoustic radiation force on small particles"*, Lab On A Chip, 12, 6, pp. 1014-1021, Science Citation Index, EBSCOhost, viewed 21 November 2016.

[16] Cahan, D, **1990**, *"From Dust Figures to the Kinetic Theory of Gases: August Kundunt and the Changing Nature of Experimential Physics in the 1860s and 1870s"*, Annals Of Science, 47, 2, p. 151, Humanities International Complete, EBSCOhost, viewed 21 November 2016.

[17] Grenvall, C, Augustsson, P, Laurell, T & Folkenberg, J, **2009**, *"Harmonic micro-channel acoustophoresis: A route to online raw milk sample precondition in protein and lipid content quality control"*, Analytical Chemistry, 81, 15, p. 6195-6200, Scopus®, EBSCOhost, viewed 21 November 2016.

[18] Augustsson, P, **2011**, *"On micro-channel Acoustophoresis : Experimental Considerations And Life Science Applications*, [Electronic Resource], n.p.: Lund : Department of Measurement Technology and Industrial Electrical Engineering, Lund University, 2011, Library catalogue (Lovisa), EBSCOhost, viewed 21 November 2016.

[19] Augustsson, P, Karlsen, J, Su, H, Bruus, H & Voldman, J, **2016**, *"Isoacoustic focusing of cells for size-insensitive acousto-mechanical phenotyping"*, Nature Communications, 7, p. 11556, MEDLINE, EBSCOhost, viewed 21 November 2016.

[20] Nilsson, A, Petersson, F, Jönsson, H & Laurell, T, **2004**, *"Acoustic control of suspended particles in micro fluidic chips"*, Lab On A Chip - Miniaturisation For Chemistry And Biology, 4, 2, p. 131, Supplemental Index, EBSCOhost, viewed 21 November 2016.

[21] Evander, M & Nilsson, J, **2012**, *"Acoustofluidics 20: Applications in acoustic trapping"*, Lab On A Chip - Miniaturisation For Chemistry And Biology, 12, 22, p. 4667, Supplemental Index, EBSCOhost, viewed 21 November 2016.

[22] Petersson, F, Nilsson, A, Jönsson, H & Laurell, T, **2005**, *"Carrier medium exchange through ultrasonic particle switching in microfluidic channels"*, Analytical Chemistry, 77, 5, pp. 1216-1221, MEDLINE, EBSCOhost, viewed 21 November 2016.

[23] VP Scientific, Inc. : Innovators in liquid handling, arraying and mixing, **2010**, *Viscosity Tables*, [ONLINE] Available at: `http://www.vp-scientific.com/Viscosity_Tables.htm`, viewed 21 November 2016.

[24] Dano, B, **2008**, *'quiverc'*, MATLAB Central File Exchange, [ONLINE] Available at: `https://se.mathworks.com/matlabcentral/fileexchange/3225-quiverc`, viewed 21 November 2016.

[25] Rayleigh, L, **1884**, *"On the Circulation of Air Observed in Kundt's Tubes, and on Some Allied Acoustical Problems"*, Philosophical Transactions of the Royal Society of London, p. 1, JSTOR Journals, EBSCO-host, viewed 21 November 2016.

[26] Thermofisher scientific, *Epifluorescence Microscope Basics*, [ONLINE] Available at: `https://www.thermofisher.com/se/en/home/life-science/cell-analysis/cell-analysis-learning-center/molecular-probes-school-of-fluorescence/fundamentals-of-fluorescence-microscopy/epifluorescence-microscope-basics.html`, viewed 21 November 2016.

[27] Barnkob, R, **2012**, *"Physics of microparticle acoustophoresis: Bridging theory and experiment"*, Ph.D. thesis, [ONLINE] Available at: `http://web-files.ait.dtu.dk/bruus/TMF/publications/PhD/PhD_2012_RB.pdf`, viewed 21 November 2016.

[28] Muller, P. B, **2012**, *"Acoustofluidics in microsystems: investigation of acoustic streaming"*, Master's thesis, [ONLINE] Available at: `http://web-files.ait.dtu.dk/bruus/TMF/publications/MSc/MSc_2012_PBM.pdf`, viewed 21 November 2016.

[29] Rednikov, A & Sadhal, S, **2011**, *"Acoustic/steady streaming from a motionless boundary and related phenomena: generalized treatment of the inner streaming and examples"*, Journal Of Fluid Mechanics, 667, 1, p. 426, Publisher Provided Full Text Searching File, EBSCOhost, viewed 21 November 2016.

[30] Happel, J & Brenner, H, **1983**, *"Low Reynolds number hydrodynamics with special applications to particulate media"*, Martinus Nijhoff Publishers, The Hague, viewed 21 November 2016.

[31] The Pennsylvania State University, *"The Coefficient of Determination, r-squared"*, [ONLINE] Available at: `https://onlinecourses.science.psu.edu/stat501/node/255`, viewed 21 November 2016.

[32] Karlsen, J, Augustsson, P & Bruus, H, **2016**, *"Acoustic Force Density Acting on Inhomogeneous Fluids in Acoustic Fields"*, Physical Review Letters, 117, 11, p. 114504, MEDLINE, EBSCOhost, viewed 21 November 2016.

[33] Deshmukh, S, Brzozka, Z, Laurell, T & Augustsson, P, **2014**, *"Acoustic radiation forces at liquid interfaces impact the performance of acoustophoresis"*, Lab On A Chip, 17, p. 3394, SwePub, EBSCOhost, viewed 21 November 2016.

[34] Tuller, M & Or, D, *"Stokes law"*, [ONLINE] Available at: `http://images.slideplayer.com/16/5192972/slides/slide_6.jpg`, viewed 21 November 2016.

[35] Einstein, A, **2005**, *"Über die von der molekularkinetischen Theorie der Wärme geforderte Bewegung von in ruhenden Flüssigkeiten suspendierten Teilchen [AdP 17, 549 (1905)]"*, Annalen Der Physik, 14, Supplement 1, p. 182, Supplemental Index, EBSCOhost, viewed 21 November 2016.

[36] Nair, N, Kim, W, Braatz, R & Strano, M, **2008**, *"Dynamics of surfactant-suspended single-walled carbon nanotubes in a centrifugal field"*, Langmuir: The ACS Journal Of Surfaces And Colloids, 24, 5, pp. 1790-1795, MEDLINE, EBSCOhost, viewed 21 November 2016.

[37] Barnkob, R, Kähler, C & Rossi, M, **2015**, *"General defocusing particle tracking"*, Lab On A Chip, 15, 17, pp. 3556-3560, MEDLINE, EBSCOhost, viewed 21 November 2016.

[38] Rossi, M & Kähler, C, **2014**, *"Optimization of astigmatic particle tracking velocimeters"*, Experiments In Fluids, 55, 9, Scopus®, EBSCOhost, viewed 21 November 2016.

[39] Unyoung, K & Son, H, **2009**, *"Simultaneous sorting of multiple bacterial targets using integrated dielectrophoretic-magnetic activated cell sorter"*, Lab On A Chip, 9, 16, pp. 2313-2318, Inspec, EBSCOhost, viewed 21 November 2016.

[40] Hou, H, Bhattacharyya, R, Hung, D & Han, J, **2015**, *"Direct detection and drug-resistance profiling of bacteremias using inertial microfluidics"*, Lab On A Chip, 15, 10, pp. 2297-2307, MEDLINE, EBSCOhost, viewed 21 November 2016.

[41] Au, A, Hoyin, L, Utela, B & Folch, A, **2011**, *"Microvalves and Micropumps for BioMEMS"*, Micromachines, 2, 2, p. 179, Publisher Provided Full Text Searching File, EBSCOhost, viewed 21 November 2016.

[42] Lee, C, Wang, W, Liu, C & Fu, L, **2016**, *"Review: Passive mixers in microfluidic systems: A review"*, Chemical Engineering Journal, 288, pp. 146-160, ScienceDirect, EBSCOhost, viewed 21 November 2016.

[43] Barnkob, R, Augustsson, P, Laurell, T & Bruus, H, **2012**, *"Acoustic radiation- and streaming-induced microparticle velocities determined by microparticle image velocimetry in an ultrasound symmetry plane"*, Physical Review E (Statistical, Nonlinear, And Soft Matter Physics), 86, 5, p. 056307, Inspec, EBSCOhost, viewed 21 November 2016.

APPENDICES

Appendix A — Populärvetenskaplig sammanfat-tning

Hur man blir av med små mikroskopiska strömmar på nolltid

Dženan Hajdarović, *Institutionen för biomedicinsk teknik, Lunds Tekniska Högskola*

Handledare: Per Augustsson Examinator: Christian Antfolk

En populärvetenskaplig sammanfattning av examensarbetet: "Undertryckande av akustisk strömning i vätskor med inhomogen densitet och kompressibilitet"

*B*akterie- och virusinfektioner är i dagsläget ett stort problem inom sjukvården, mycket tack vare att dessa blir mer och mer motståndskraftiga mot läkemedel och vaccin. En metod vid namn akustofores *ger snabba och skonsamma analyser av t.ex. blodprov. Begränsningen med denna metod relaterar till ett fenomen som kallas* akustisk strömning*, se figur 1. Detta arbete undersökte om denna cirkulära strömning kunde motverkas genom att använda vätskor med* inhomogena egenskaper*. Det visade sig att strömningen reducerades med en* faktor 57 *och därmed kan partiklar av samma storlek som bakterier manipuleras i ett akustiskt fält.*
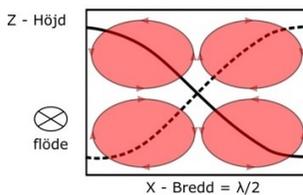
**Figur 1:** *Principen bakom akustisk strömning*

Föreställ er metoden bakom *akustofores* som ett kösystem till affären med en massa människor som radar upp sig en efter en. Inne i en så kallad mikrokanal, som är i storleken av ett hårstrå, så kan partiklar också rada upp sig i olika köer, beroende på skillnader i akustiska egenskaper. Dessa "köer" skapas av en stående tryckvåg till följd av ultraljud som läggs över mikrokanalen. I affären är det däremot kassörers humör som avgör hur många köer vi som handlar får. Hur som helst, en nod har vi i mitten av en mikrokanal och dit rör sig partiklar som har en så kallad positiv akustisk kontrastfaktor, som beror på partiklarnas storlek, densitet och hur mycket de ändras vid pålagt tryck. Antinoderna hittar vi istället vid sidoväggarna där partiklar med en negativ akustisk kontrastfaktor radar upp sig, se figur 2.
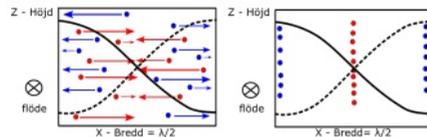
Figur 2: *Principen bakom akustofores*

Det här är alltså en metod som bl.a kan separera röda blodkroppar from blodplasma eller fettmolekyler. Man skulle även kunna leta upp och sortera bort cancerceller i blod, d.v.s. lösa problemet med att hitta "nålen i höstacken". Men som sagt, akustisk strömning försämrar möjligheten till fokusering då väldigt små partiklar används ($< 1\mu$m), eftersom dessa istället blandas runt i cirkulära banor. En metod som kallas Isoakustisk fokusering användes i detta projekt som nyligen utvecklades som en möjlig förbättring av akustofores, med möjligheten att motverka just akustisk strömning. Ett medium/vätska med inhomogena egenskaper användes, d.v.s. både en partikel-lösning och en lösning med högre densitet (Iodixanol).
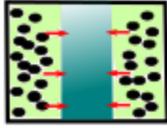
Figur 3: *Iso-akustisk fokusering*

Dessa vätskor låter man först flöda in i en mikrokanal bredvid varandra, även kallat *lamineras*. När ultraljudet slås på, så kommer den tyngre vätskan fokuseras mot mitten av mikrokanalen, så kallat stabiliseras, där vi har den stående vågens nod och partikel-lösningen knuffas ut mot sidoväggarna, se figur 3. Sedan kommer partiklarna, precis som vid vanlig akustofores, röra sig mot mitten av kanalen, fram till den position där den akustiska impedansen mellan vätskan och partikeln är densamma.

Patientnära vård är idag ett hett område inom biomedicin där patienter inte vill känna sig bundna till sjukhus och vill istället kunna ta prover på sig själva i sitt eget hem. Iso-akustisk fokusering är en metod som mycket väl kan komma att implementeras i sådana enkla apparater, där vi får snabba och skonsamma blodanalyser som kan sortera ut och diagnostisera bakterie- eller virus-halter.

Innan detta projekt genomfördes så hade undertryckande av akustisk strömning vid iso-akustisk fokusering mest varit en teori. Detta projekt har alltså lyckats ge starka bevis i form av experimentell data som visar på att detta fenomen faktiskt är sant. En 57-faldig minskning skojar man inte bort!

Bonus-kuriosa:

— *Det finns mer bakterier i din mun än vad det finns människor i världen. Tänk på det nästa gång du känner dig ensam.*

— *Mellan åren 1918-1920 så dog runt 20-40 miljoner människor i en pandemi orsakad av ett nytt och muterat virus som angrep luftvägarna.*

102

Appendix B — Matlab code

```matlab
%printALL.m

%Loading and printing of all the results for Aim 1,2 ...
    and 3

clear
clc
%% initial testing (aim 1) loading
%3um PS-beads

% load('dat_9mart_3um_aim1.mat')
%% inhomogeneous medium (aim 3) loading

%1um PS-beads, t=0min

load('dat_1um_31maj_set1_0min_newtry.mat')
load('dat_1um_31maj_set2_0min_newtry.mat')
load('dat_1um_31maj_set3_0min_newtry.mat')
load('dat_1um_31maj_set4_0min_newtry.mat')
load('dat_1um_31maj_set5_0min_newtry.mat')

%1um PS-beads, t=5min

% load('dat_1um_31maj_set1_5min_newtry.mat')
% load('dat_1um_31maj_set2_5min.mat')
% load('dat_1um_31maj_set3_5min_newtry.mat')


%% homogeneous medium (aim 2) loading

%5um PS-Beads

% load('dat_aim2_5um_set8_newtry')
% load('dat_aim2_5um_set3_newtry')
% load('dat_aim2_5um_set1_newtry')
% load('dat_aim2_5um_set4_newtry')
% load('dat_aim2_5um_set5_newtry')
% load('dat_aim2_5um_set7_newtry')
% load('dat_aim2_5um_set2_newtry')
% load('dat_aim2_5um_set6_newtry')
%
% load('dat_aim2_5um_set9_newtry')
% load('dat_aim2_5um_set10_newtry')
```

```matlab
44  % load('dat_aim2_5um_set11_newtry')
45  % load('dat_aim2_5um_set12_newtry')
46  % load('dat_aim2_5um_set13_newtry')
47
48  %1um PS-beads
49
50  % load('dat_17maj_aim2_set1_NEW.mat')
51  % load('dat_17maj_aim2_set2_NEW.mat')
52  % load('dat_17maj_aim2_set3_NEW.mat')
53
54  %% correct 3um filenames (AIM 1)
55  %3um PS_beads
56
57  %fileNames = {'dat_9mart_3um_aim1.mat'};
58
59  %% correct 1um files (AIM 3 - Inhomogeneous medium):
60
61  %diffusion time t = 0 min
62
63  %fileNames =
64  %{'dat_1um_31maj_set3_0min_newtry.mat',
65  %'dat_1um_31maj_set4_0min_newtry.mat',
66  %'dat_1um_31maj_set5_0min_newtry.mat',
67  %'dat_1um_31maj_set1_0min_newtry.mat',
68  %'dat_1um_31maj_set2_0min_newtry.mat'};
69
70  %diffusion time t = 5 min
71
72  %fileNames =
73  %{'dat_1um_31maj_set1_5min_newtry.mat',
74  %'dat_1um_31maj_set2_5min.mat',
75  %'dat_1um_31maj_set3_5min_newtry.mat'};
76
77  %% correct 1um and 4.8um (AIM 2)
78  %1um PS-beads
79
80  %fileNames =
81  %{'dat_17maj_aim2_set1_NEW.mat',
82  %'dat_17maj_aim2_set2_NEW.mat',
83  %'dat_17maj_aim2_set3_NEW.mat'};
84
85  %4.8um PS-beads
86
87  %fileNames =
88  %'{'dat_aim2_5um_set1_newtry',
89  %'dat_aim2_5um_set3_newtry',
90  %'dat_aim2_5um_set8_newtry',
91  %'dat_aim2_5um_set9_newtry',
```

```
92  %'dat_aim2_5um_set10_newtry',
93  %'dat_aim2_5um_set11_newtry',
94  %'dat_aim2_5um_set12_newtry',
95  %'dat_aim2_5um_set13_newtry'};
```

```
1   %sorting.m
2
3   % sorting the results into only one combined data set
4   datALL.X = [];
5   datALL.Y = [];
6   datALL.Z = [];
7
8   datALL.DX = [];
9   datALL.DY = [];
10  datALL.DZ = [];
11
12  datALL.ID = [];
13  datALL.EX = [];
14  datALL.In = [];
15  datALL.Cm = [];
16
17  for i = 1:length(fileNames)
18      dataloadStruct = load(fileNames{1,i});
19      dataload = struct2cell(dataloadStruct);
20      currData = dataload{1};
21      datALL.X = [datALL.X currData.X];
22      datALL.Y = [datALL.Y currData.Y];
23      datALL.Z = [datALL.Z currData.Z];
24      datALL.DX = [datALL.DX currData.DX];
25      datALL.DY = [datALL.DY currData.DY];
26      datALL.DZ = [datALL.DZ currData.DZ];
27      maxID = max(currData.ID);
28      datALL.ID = [datALL.ID currData.ID + maxID];
29      datALL.EX = [datALL.EX ones(size(currData.In))*i];
30      datALL.In = [datALL.In currData.In];
31      datALL.Cm = [datALL.Cm currData.Cm];
32
33  end
34
35  save('datALL.mat','datALL')
```

```
1
2   % filtering_and_velocity_vectors.m
3
4   %% Filtering and plotting velocity vectors DX,DZ for ...
```

```matlab
     points x,z - 1um PS-beads
5
6  data = datALL;
7  frameRate = 0.5; %no iodixanol (aim2)
8  %frameRate = 0.1;  %with iodixanol (aim 3)
9
10 %positions and velocitites
11 x1 = data.X.*1e-6;
12 y1 = data.Y.*1e-6;
13 z1 = (data.Z.*1e-6)-3.9e-5; %error in z-direction (due ...
      to calibration error)
14
15 Dx1 = (data.DX.*1e-6)/frameRate;
16 Dz1 = (data.DZ.*1e-6)/frameRate;
17 Dy1 = (data.DY.*1e-6)/frameRate;
18
19 mag1 = sqrt(Dx1.^2 + Dz1.^2);
20
21 %filtering out the outliers
22 flt_In = data.In ≥ 5 & data.In ≤ 120;
23 flt_Cm = data.Cm ≥ 0;
24 flt_Z =  z1 ≥ 0 & z1 ≤ max(z1);
25 flt_EX = data.EX ≥ 1;
26 flt_DX = Dx1 ≥ -17e-6 & Dx1 ≤ 17e-6;
27 flt_DZ = Dz1 ≥ -4e-6 & Dz1 ≤ 4e-6;
28 flt = flt_In & flt_Cm & flt_Z & flt_EX & flt_DX & flt_DZ;
29
30 %%
31 %creating a DX_DZ grid
32 nBinsY = 30;
33 nBinsZ = 30;
34 y0 = 0;
35 x0 = 0;
36 z0 = 0;
37 W = 375e-6; %width of channel
38 H = 160e-6; %height of channel
39 % W = (max(data.X(flt)) - min(data.X(flt)))*1e-6;
40 % H = (max(data.Z(flt)) - min(data.Z(flt)))*1e-6;
41
42 %positions in x,y,z
43 x = x1(flt);
44 y = y1(flt);
45 z = z1(flt);
46
47 %velocities in x,y,z
48 Dx = Dx1(flt);
49 Dz = Dz1(flt);
50 Dy = Dy1(flt);
```

```matlab
51
52  xq = linspace(x0,x0 + W,nBinsY);
53  yq = linspace(y0,y0 + 2*W,nBinsY);
54  zq = linspace(z0,z0 + H,nBinsZ);
55
56  [XQ,ZQ] = meshgrid(xq,zq);
57
58  %velocities in a grid with the size [XQ,ZQ]
59  DXQ = griddata(x,z,Dx,XQ,ZQ,'natural');
60  DZQ = griddata(x,z,Dz,XQ,ZQ,'natural');
61
62  %magnitude of velocities
63  Umag_filtered = sqrt(DXQ.^2 + DZQ.^2);
64
65  nTracks = max(data.ID); %find number of tracks
66  tracksLength = zeros(1, nTracks); %find number of ...
        points per track
67  for n = 1:nTracks
68      tracksLength(n) = sum(data.ID == n);  %adding them ...
            together
69  end
70
71  figure
72  plot3(x, y, z,'.','Color','k') %plot all points
73  title({'Filtered trajectories in the XZ-view'});
74  zlim([0 1.6e-4])
75  xlabel('X [m]')
76  zlabel('Z [m]')
77
78  %colorplots with velocity vectors DX and DZ
79  figure
80  quiverc(XQ,ZQ,DXQ,DZQ,1);
81  title({'Velocity vectors as arrows ';'with components ...
        (DX,DZ) at the points (x,z) - ...
        Experimental'},'Color','white','FontSize',10);
82  xlabel('X [m]')
83  ylabel('Z [m]')
84  colorbar('vertical');
85  c = colorbar;
86  c.Color = 'black';
87  c.Label.String = 'Velocity vectors as arrows - coded ...
        by magnitude';
88  c.Label.Color = 'white';
89
90  %% theory: Utot as a function of z (acoustic ...
        streaming) at X = 100um
91
92  rho_w = 997; %density of water
```

```matlab
93  c_w = 1497;   %speed of sound in water
94  eta = 8.9e-4; %viscosity of water
95  phi = 0.17; %acoustic contrast factor for PS-beads
96
97  Eac = 21; %acoustic energy density
98  k = 8378; %wave number
99  XQ_z = 100e-6; %x-position
100 W0 = 375e-6; %width of channel
101 H0 = 160e-6; %heigh of channel
102 a = 0.5e-6; %radius of PS-bead
103 zq_z = linspace(0,160e-6,30);
104
105 Urad = (((2*phi)/(3*eta))*(a^2)*k*Eac)*sin(2*k*XQ_z);
106
107 Ux = ((0.75*Eac/(rho_w*c_w)))*sin(2*k*XQ_z).*..
108 (1-(3*(ZQ-H0/2).^2/(H0/2)^2));
109
110 Utot = Ux + Urad;
111 A1 = DXQ;
112 B1 = A1(1:30,8); %velocitiy as a function of channel ...
        heigth Z
113 figure
114 D2 = Utot(1:30,8); %theoretical velocity
115 plot(zq_z,D2,'-')
116 hold on
117 plot(zq_z,B1,'*')
118 title({'Lateral velocity at the width X = 100\mum'});
119 xlabel('Z [m]')
120 xlim([0 160e-6])
121 ylabel('U [m/s]')
122 legend('Rayleigh', 'Data')
123
124 max(max(DXQ+DZQ))  %max magnitude velocity
125
126 %% %% theory Utot as a function of z (acoustic ...
        streaming) at X = 275um
127 u0 = 0;
128 rho_w = 997;
129 c_w = 1497;
130 eta = 8.9e-4;
131 phi = 0.17;
132
133 Eac = 20;
134 k = 8378;
135 XQ_z = 275e-6;
136 W0 = 375e-6;
137 H0 = 160e-6;
138 Δz = 0;
```

```matlab
139  Δx = 0;
140  a = 0.5e-6;
141  zq_z = linspace(0,160e-6,30);
142
143  Urad = (((2*phi)/(3*eta))*(a^2)*k*Eac)*sin(2*k*XQ_z);
144  Ux = ((0.75*Eac/(rho_w*c_w)))*sin(2*k*XQ_z).*...
145  (1-(3*(ZQ-H0/2).^2/(H0/2)^2));
146
147  Utot = Ux + Urad;
148  A1 = DXQ;
149  B1 = A1(1:30,22); %velocitiy location as a function of ...
         channel height Z
150  figure
151  D2 = Utot(1:30,22);
152  plot(zq_z,D2,'-')
153  hold on
154  plot(zq_z,B1,'*')
155  title({'Lateral velocity at the width X = 275\mum'});
156  xlabel('Z [m]')
157  xlim([0 160e-6])
158  ylabel('U [m/s]')
159  legend('Rayleigh', 'Data')
160
161  max(max(DXQ+DZQ)) %max magnitude velocity
162
163
164  %% Horizontal/lateral velocity
165  Eac = 20;
166  c_w = 1497;
167  rho_w = 997;
168  phi = 0.17;
169  eta = 8.9e-4;
170  k = 8378;
171  W0 = 375e-6;
172  H0 = 160e-6;
173  a = 0.5e-6;
174  ZQ_z = 75e-6;
175  u0 = 0;
176
177  xq_x = linspace(0,375e-6,30);
178
179  %rayleigh model + Urad
180  Urad = (((2*phi)/(3*eta))*(a^2)*k*Eac)*sin(2*k*XQ);
181  Ux = ((0.75*Eac/(rho_w*c_w)))*sin(2*k*XQ).*...
182  (1-(3*(ZQ_z-H0/2).^2/(H0/2)^2));
183  Utot_2 = Urad + Ux;
184
185  %corrected theoretical model
```

```matlab
f = 2e6;
∆_x = sqrt((2*eta)/(rho_w*2*pi*f));  %boundary layer ...
    thickness
a0 = ∆_x*sqrt(3/phi);
s_t = 0.194; %thermoviscous correction at mid channel
chi_x_mid = (1 - 1.004*((2*0.5e-6)/150e-6) + ...
    0.418*((2*0.5e-6)/150e-6)^2)^-1;
corr_mid = ((a^2/(chi_x_mid*a0^2)) + s_t);
% chi_x_b = (1 - 1.305*((2*a)/H0) + 1.18*((2*a)/H0)^2)^-1;
% corr_b = ((a^2/(chi_x_b*a0^2)) + s_t);
Utot_corrected = -corr_mid*((4*Eac)/(rho_w*c_w))*..
sin(2*k*(xq_x+(W0/2)));

figure
D1 = Utot_2(14,1:30);    %velocity as a function of x
plot(xq_x,D1,'*')
hold on

plot(xq_x,Utot_corrected,'-')
% hold on
%total velocity of particle
%figure
A2 = DXQ;
C1 = A2(14,1:30);
plot(xq_x,C1,'*','Color','red')
title({'Horizontal velocity at the depth Z = 75\mum'});
xlabel('X [m]')
xlim([0 375e-6])
ylabel('Velocity [m/s]')
legend('Rayleigh', 'Corrected','Data')
```

```matlab
%magnitude_fitting.m

%% Plotting the magnitude velocities

Eac=19.5; %acoustic energy density
k=8378;   %wave number

eta = 8.9e-4; %viscosity of water
phi = 0.17;   %acoustic contrast factor of PS-beads
rho_w = 997; %density of water
c_w = 1497;   %speed of sound in water
a = 0.5e-6;   %particle radius

W0 = 375e-6;  %width of channel
H0 = 157e-6;  %height of channel

```

```matlab
17  %theoretical model Urad + Rayleigh
18  Urad = (((2*phi)/(3*eta))*(a^2)*k*Eac)*sin(2*k*XQ);
19
20  Ux = ((0.75*Eac/(rho_w*c_w)))*sin(2*k*XQ).*...
21  (1-(3*(ZQ-H0/2).^2/(H0/2)^2));
22
23  Uz = ((0.75*Eac/(rho_w*c_w))*k*H0)*cos(2*k*XQ).*...
24  ((ZQ-H0/2).^3/((H0/2)^3) - (ZQ-H0/2)/(H0/2));
25
26  %%
27  %%color plots of the magnitude
28
29  figure
30  teorUmag = sqrt((Urad+Ux).^2 + (Uz).^2);
31  pcolor(XQ,ZQ,teorUmag)
32  hold on
33  set(gcf, 'renderer', 'zbuffer')
34  quiver(XQ,ZQ,DXQ,DZQ,2,'color','k')
35  %title('Magnitude of velocity vectors - ...
       Experimental','FontSize',8)
36  xlabel('X [m]')
37  ylabel('Z [m]')
38  c1 = colorbar;
39  %set(c1, 'ylim', [0   1.6441e-05])
40  c1.Label.String = 'm/s';
41
42  figure
43  teorUmag = sqrt((Urad+Ux).^2 + (Uz).^2);
44  pcolor(XQ,ZQ,teorUmag)
45  hold on
46  set(gcf, 'renderer', 'zbuffer')
47  quiver(XQ,ZQ,Urad + Ux,Uz,2,'color','k')
48  %title('Magnitude of velocity vectors - ...
       Theoretical','FontSize',8)
49  xlabel('X [m]')
50  ylabel('Z [m]')
51  c2 = colorbar;
52  set(c2, 'ylim', [0   16.441e-06])
53  c2.Label.String = 'm/s';
54
55  figure
56  expUmag_1um = sqrt((DXQ.^2+DZQ.^2));
57  pcolor(XQ,ZQ,expUmag_1um)
58  hold on
59  set(gcf, 'renderer', 'zbuffer')
60  quiver(XQ,ZQ,DXQ,DZQ,2,'color','k')
61  %title('Magnitude of Utot = Ustr + Urad (1 μm ...
       PS-beads) - Experimental','FontSize',8)
```

```matlab
62  xlabel('X [m]')
63  ylabel('Z [m]')
64  c3=colorbar;
65  set(c3, 'ylim', [0    1.6441e-05])
66  c3.Label.String = 'm/s';
```

```matlab
1   %GDPT_trajectories
2
3   % .ID means track number
4   % .IN means frame number
5
6   frameRate = 0.5; %aim2 1um
7   %frameRate = 0.1; %aim3 1um
8
9   load('dat_17maj_aim2_set1_NEW.mat')  %one of the sets ...
        used for 1um
10  data = dat_17maj_aim2_set1_NEW;
11
12  %positions and velocitites
13  x1 = data.X.*1e-6;
14  y1 = data.Y.*1e-6;
15  z1 = data.Z.*1e-6 - 3.9e-5;
16
17  Dx1 = (data.DX.*1e-6)/frameRate;
18  Dy1 = (data.DY.*1e-6)/frameRate;
19  Dz1 = (data.DZ.*1e-6)/frameRate;
20
21  %filtering
22  flt_In = data.In ≥ 5 & data.In ≤ 120;
23  flt_Cm = data.Cm ≥ 0;
24  flt_Z =   z1 ≥ 0 & z1 ≤ max(z1);
25  %flt_EX = data.EX ≥ 1;
26  flt_DX = Dx1 ≥ -17e-6 & Dx1 ≤ 17e-6;
27  flt_DZ = Dz1 ≥ -4e-6 & Dz1 ≤ 4e-6;
28  flt = flt_In & flt_Cm & flt_Z & flt_DX & flt_DZ;
29
30  nTracks = max(data.ID(flt)); %find number of tracks
31  tracksLength = zeros(1, nTracks); %find number of ...
        points per track
32  for n = 1:nTracks
33      tracksLength(n) = sum(data.ID(flt) == n);
34  end
35
36  xNew = x1(flt);
37  yNew = y1(flt);
38  zNew = z1(flt);
39
```

```
40  DxNew = Dx1(flt);
41  DyNew = Dy1(flt);
42  DzNew = Dz1(flt);
43
44  figure
45  subplot(2,2,[1,2])
46  plot(xNew, zNew,'.') %plot all points
47  hold on, grid on
48  axis([0 400e-6 0 160e-6])
49  xlabel('X [m]')
50  ylabel('Z [m]')
51
52  subplot(2,2,3)
53  plot(DxNew,DzNew,'.')     %m/s
54  axis([-20e-6 20e-6 -20e-6 20e-6])
55  xlabel('DX [m/s]')
56  ylabel('DZ [m/s]')
57  grid on
58
59  subplot(2,2,4)
60  plot(DxNew,DyNew,'.')   %m/s
61  axis([-20e-6 20e-6 -20e-6 20e-6])
62  xlabel('DX [m/s]')
63  ylabel('DY [m/s]')
64  grid on
```

```
1  %GDPT_start_end
2
3  % .ID means track number
4  % .IN means frame number
5
6  load('dat_17maj_aim2_set1_NEW.mat')
7  data = dat_17maj_aim2_set1_NEW;
8
9  frameRate = 0.5;
10
11  %positions and velocitites
12  x1 = data.X.*1e-6;
13  y1 = data.Y.*1e-6;
14  z1 = data.Z.*1e-6-3.9e-5;
15
16  Dx1 = (data.DX.*1e-6)/frameRate;
17  Dz1 = (data.DZ.*1e-6)/frameRate;
18  Dy1 = (data.DY.*1e-6)/frameRate;
19
20  %filtering
21  flt_In = data.In ≥ 5 & data.In ≤ 120;
```

```matlab
22  flt_Cm = data.Cm ≥ 0;
23  flt_Z =  z1 ≥ 0 & z1 ≤ max(z1);
24  flt_DX = Dx1 ≥ -25e-6 & Dx1 ≤ 25e-6;
25  flt_DZ = Dz1 ≥ -10e-6 & Dz1 ≤ 10e-6;
26  flt = flt_In & flt_Cm & flt_Z & flt_DX & flt_DZ;
27
28  nTracks = max(data.ID(flt)); %find number of tracks
29  tracksLength = zeros(1, nTracks); %find number of ...
        points per track
30  for n = 1:nTracks
31      tracksLength(n) = sum(data.ID(flt) == n);
32  end
33
34  xNew = x1(flt);
35  yNew = y1(flt);
36  zNew = z1(flt);
37
38  figure
39  plot3(xNew, yNew, zNew, '.', 'Color', 'k') %plot all ...
        points
40  hold on
41  %find track with larger number of points
42
43  qualifiedTracksID = find(tracksLength ≥ 2); %all ...
        trajectories over a treshhold
44  grid on
45
46
47  for i = 1:length(qualifiedTracksID)
48      ind = (data.ID(flt) == qualifiedTracksID(i));
49
50      allParticles = find(ind==1);
51      firstParticle = allParticles(1,1);
52      lastParticle = allParticles(1,size(allParticles,2));
53
54
55      plot3(xNew(firstParticle),yNew(firstParticle),...
56          zNew(firstParticle),'go');
57      %where does the trajectory begin
58      hold on
59      plot3(xNew(lastParticle),yNew(lastParticle),...
60          zNew(lastParticle),'ro');
61      %where does the trajectory end
62      hold on
63      plot3(xNew(allParticles),yNew(allParticles),...
64          zNew(allParticles),'k');
65      %draw line between particles in each trajectory
66      title('Filtered trajectories of the particles in ...
```

```matlab
              the XZ-view')
67      set(gca, 'ZLim', [0 160e-6])
68      xlabel('X [m]')
69      ylabel('Y [m]')
70      zlabel('Z [m]')
71      legend('Particles','Starting point','Ending point', ...
            'Location', 'NorthEastOutside')
72
73  end
```

Appendix C — GDPT-manual: Step-by-step guide explaining the software

This guide is written by the author in order to explain the complete analysis using the GDPT-software. However, there is an even more detailed guide that was written by the developers and colleagues Rune Barnkob, Christian J. Kähler and Massimiliano Rossi [37].
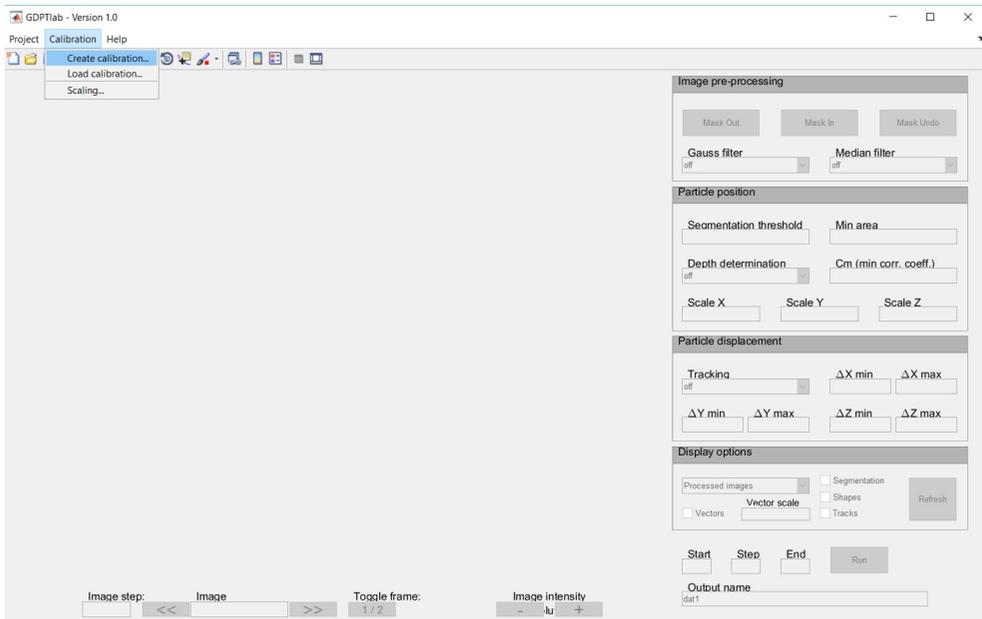

After opening the GDPT-software, the first thing to be done is the calibration. Click on *"create calibration"* and then chose the reference images which were acquired for each depth of the microchannel. In this specific case, 4.8 μm PS-beads were used.
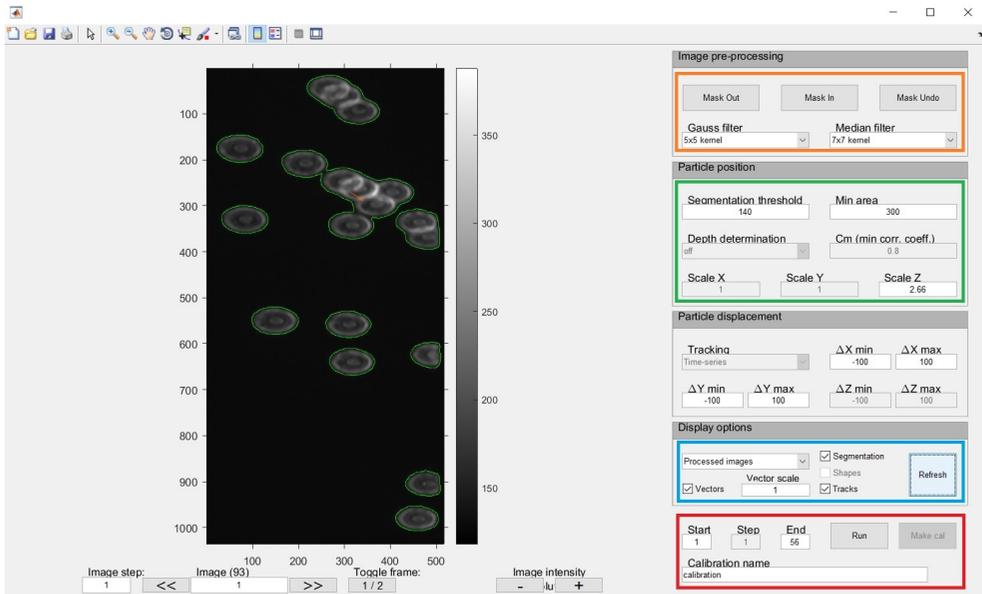
A second user interface will now be opened. Using the image-preprocessing (☐), one can filter out noise and smoothen the images using the gauss- and median-filter. Using the *mask out* and *mask in* options, particular PS-beads can be cropped out. Mask out — crops out target beads that will be analysed whilst mask in — crops out beads which you do not want to analyse.

The segmentation properties (☐) use an intensity threshold and min area, set as 140 and 300 in this case. The *scale Z* component is related to the step size between the acquired images. In these experiments, a step size of 2μm between each depth position/image was used. The value of $2.66 = 2 \cdot 1.33$ takes the refraction of light in water into account.

In the display options (☐), the refresh button gives us an possibility to see how well the particles are segmented. Finally, one can chose which images that will be used in the analysis using the start and end options (☐). When this is done, the name of the calibration should be written. This is needed since the results will be stored in the Matlab directory afterwards. Click on *"Run"* to start the first part of the calibration, which is to see what PS-beads that are valid.
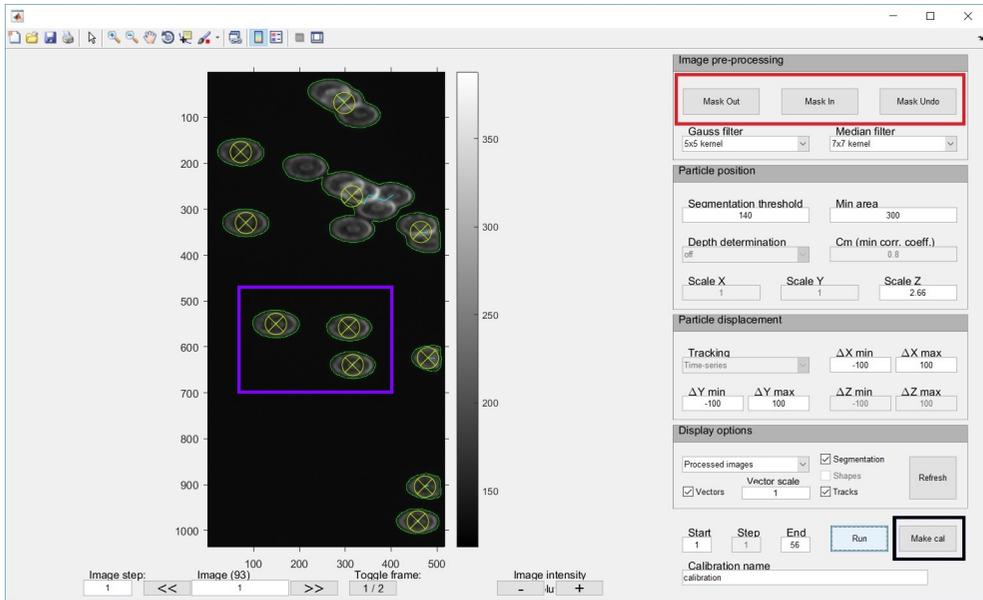
The valid PS-beads are denoted as (⊗), meaning that trajectories at each chosen depth have been successfully observed. As previously mentioned, one can crop out specific PS-beads using the mask out and mask in options (□). In this case the three PS-beads in the middle were cropped out and used, (□). When all this is done, the calibration analysis can be started by clicking on *"Make cal"*, (□) which will take a few minutes, depending on the amount of images used.
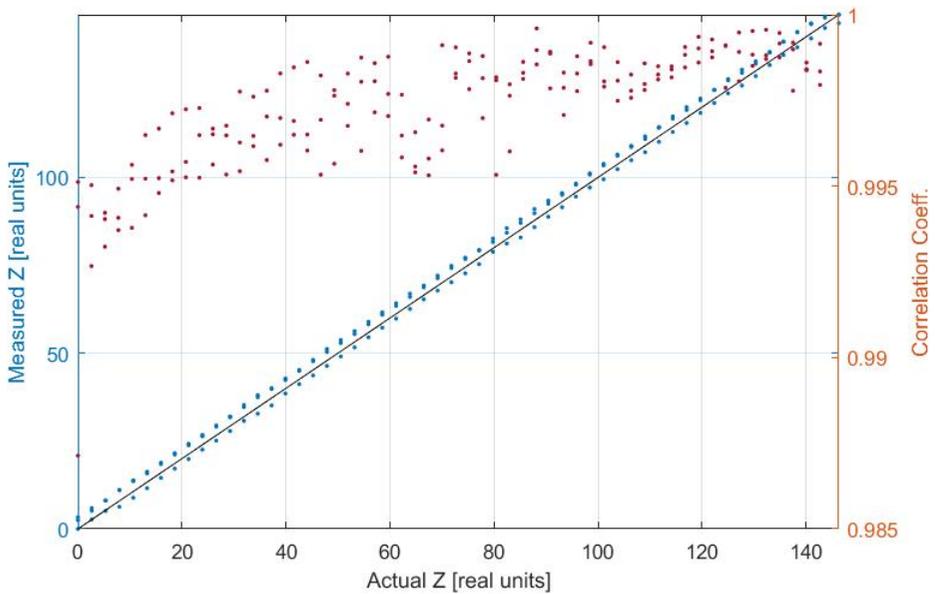
The resulting plot of the calibration shows the measured depth position ($\bullet$) of the three chosen PS-beads and how close they are the actual depth position (—). The statistical goodness of the calibration is also illustrated as the cross-correlation factor C_m denoted as ($\bullet$). This particular result showcases an extremely good calibration with $C_m > 0.99$, where $C_m = 1$ would be a perfect fit. We now have a "library" of reference images that will be used during the particle tracking analysis.
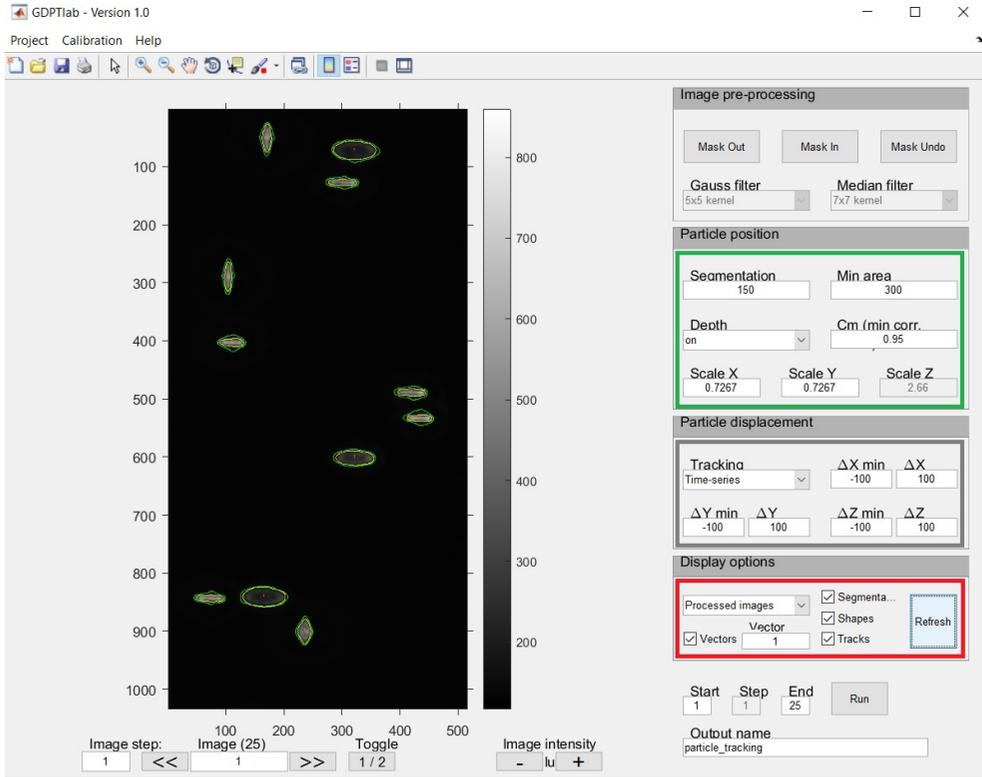
After the successful calibration, the next part will be to establish the actual particle tracking analysis. Moving back to the original user interface of the software, select the images for particle tracking by clicking on *"Project"* and then *"Load images"*. The saved calibration shall also be loaded to the software by clicking on *"Calibration"* and then *"Load calibration"*. In the segmentation options (□), new options regarding the particle tracking will be present. Select *"Depth — on"* and chose a desired C_m coefficient, for instance 0.95. By doing this, all PS-bead trajectories under this threshold will be removed during the analysis. Also, the X- and Y-scale of the width and length positions can be set. In this case, it was known that the width of the microchannel was 375 μm which corresponded to 516 pixels in the images, thus giving a scale of 0.7267 μm per pixel. The region for which the analysis will be done can be selected in the particle displacement options (□). The tracking shall be chosen as *"Time series"* and the x-,y- and z-regions can be initially set as the original values -100 to 100, to be sure that all velocities and trajectories are included. This region can always be changed after the analysis. To see the goodness of the segmentation, the *"Refresh"* button can be pressed. The yellow color around the PS-beads means that they are valid for analysis, after being compared to the reference images in the loaded cal-

ibration. To start the particle tracking analysis, give it a name and then click *"Run"*. The analysis will take a few minutes, where it compares the acquired target images with the reference images in the calibration library.
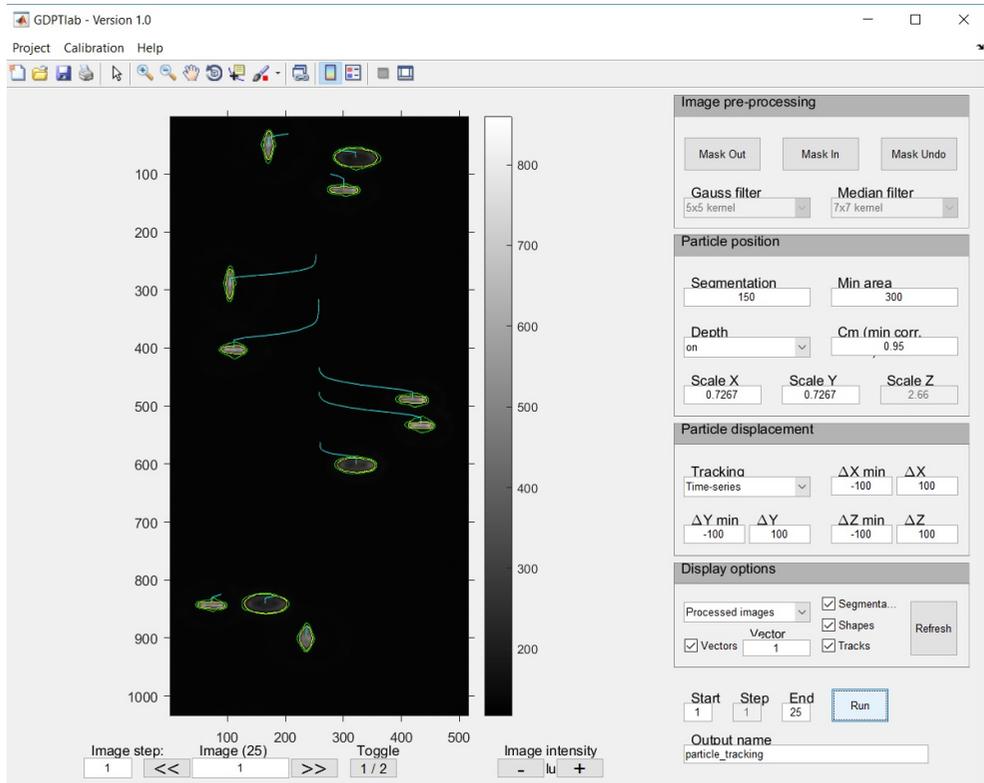
Finally, the trajectories of the PS-beads will be shown in the user interface (x-y orientation), denoted as the blue lines (—).
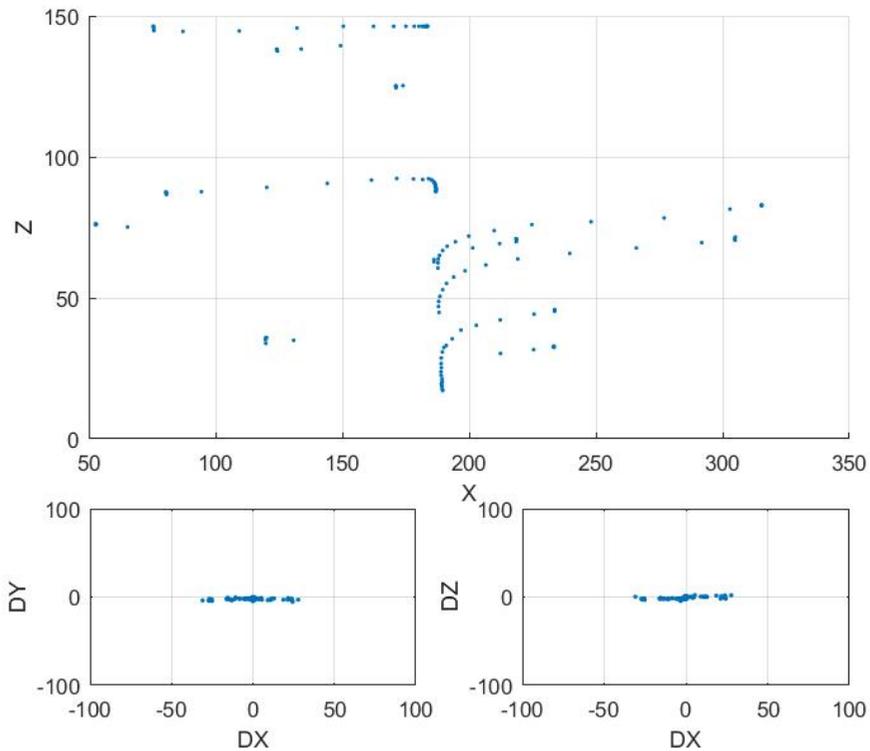
A more detailed version of the results is also created. The lateral movement towards the middle of the microchannel (node of the $\lambda/2$ standing wave) of the larger 4.8 μm can be seen, as they are affected by the acoustic radiation force. In addition to the trajectories, we will also obtain the velocities in the x-, y- and z-orientation, denoted as DX, DY and DZ, respectively. These results can be further analysed in Matlab with the saved Matlab file denoted as *"particle tracking"* in this case. The units of the trajectory axises can be set to μm. The same goes for the velocity plots (μm/s), where the min and max region also can be set to more suitable values. In this case, the region for the obtained velocities can clearly be decreased.